

ANNUAL REPORT 2014

INSTITUTE OF RESOURCE ECOLOGY

hzdr

 **HELMHOLTZ**
ZENTRUM DRESDEN
ROSSENDORF

Wissenschaftlich-Technische Berichte
HZDR-059

Annual Report 2014

Institute of Resource Ecology

Editor:

Prof. Dr. Thorsten Stumpf

Executive editors:

Dr. Harald Foerstendorf

Dr. Frank Bok

Dr. Anke Richter

HZDR

 **HELMHOLTZ**
ZENTRUM DRESDEN
ROSSENDORF

Print edition: ISSN 2191-8708

Electronic edition: ISSN 2191-8716

The electronic edition is published under Creative Commons License (CC BY-NC-ND):

Qucosa: <http://fzd.qucosa.de/startseite/>

Published by Helmholtz-Zentrum Dresden-Rossendorf e.V.

Contact

Helmholtz-Zentrum Dresden-Rossendorf e.V.
Institute of Resource Ecology

Postal Address

P.O. Box 51 01 19
D-01314 Dresden
Germany

Address for visitors

Bautzner Landstraße 400
D-01328 Dresden
Germany

Phone: +49 (0) 351 260 3210

Fax: +49 (0) 351 260 3553

e-mail: contact.resourceecology@hzdr.de

<http://www.hzdr.de/FWO>

This report is also available at <http://www.hzdr.de/FWO>

Cover picture

The complex hydrolysis reactions of the hexavalent uranium ion hamper an accurate evaluation of spectroscopic data due to coexisting species. State-of-the-art numerical algorithms or quantum-chemical methods reveal the spectral properties of single species or provide reasonable predictions of their spectral properties, respectively. In particular, a combination of spectroscopic and numerical methods is promising for the identification of single species and for the correlation with respective molecular structures (for more details see p. 35).

The cover figure shows a uranyl(VI) moiety coordinated by water molecules and competing acetate (CH_3COO^-) anions. The uranyl(VI) ion can form acetate complexes with different stoichiometries depending on the prevailing ligand concentration. Emission spectra of single complexes extracted with parallel factor analysis (PARAFAC) from experimental data are shown in the background

Preface

THE INSTITUTE OF RESOURCE ECOLOGY (IRE) is one of the eight institutes of the Helmholtz-Zentrum Dresden – Rossendorf (HZDR). The research activities are mainly integrated into the program “Nuclear Waste Management, Safety and Radiation Research (NUSAFE)” of the Helmholtz Association (HGF) and focused on the topics “Safety of Nuclear Waste Disposal” and “Safety Research for Nuclear Reactors”.

Additionally, various activities have been started investigating chemical and environmental aspects of processing and recycling of strategic metals, namely rare earth elements. These activities are located in the HGF program “Energy Efficiency, Materials and Resources (EMR)”. Both programs, and therefore all work which is done at IRE, belong to the research sector “Energy” of the HGF.

The research objectives are the protection of humans and the environment from hazards caused by pollutants resulting from technical processes that produce energy and raw materials. Treating technology and ecology as a unity is the major scientific challenge in assuring the safety of technical processes and gaining their public acceptance. We investigate the ecological risks exerted by radioactive and non-radioactive metals in the context of nuclear waste disposal, the production of energy in nuclear power plants, and in processes along the value chain of metalliferous raw materials. A common goal is to generate better understanding about the dominating processes essential for metal mobilization and immobilization on the molecular level by using advanced spectroscopic methods. This in turn enables us to assess the macroscopic phenomena, including models, codes, and data for predictive calculations, which determine the transport and distribution of contaminants in the environment.

The extraordinary broadness of research topics and activities are shown by some selected highlights in 2014:

One important event of the year 2014 was the organization and hosting of ATAS 2014, the “Second International Workshop on Advanced Techniques in Actinide Spectroscopy” in November, attracting 80 scientists. Beside several outstanding scientific talks, the highlight was the discussion of the Round-Robin test, initiated at the beginning of 2014, where 20 in-

ternational institutions with around 40 scientists were involved.

Detailed numerical simulations of hypothetical accidents in nuclear power plants are the basis for the development and assessment of accident management measures and strategies, which in the case of multiple failures of safety systems can prevent or mitigate core damages. On the basis of simulations for a station blackout scenario in a Russian-type pressurized water reactor, it was shown that by application of an optimized accident management strategy the core heat-up can be delayed by several hours. This additional time margin gives more time and different possibilities for operator interventions, e.g., to restore power supply for additional measures to mitigate the accident.

The Reactive Transport division has broadened the library of different radiolabeling techniques for particles - in close international cooperation with the JRC, Ispra Italy. Tracing of nanoparticles in minute concentrations in complex media became possible with unprecedented experimental ease by either radiochemical synthesis or proton irradiation methods at the in-house cyclotron. Unique life-cycle studies of nanoparticles were thusly made feasible, including the first ever imaging of carbon nanotube transport in porous geological media via PET imaging.

Cells of *Sporomusa sp.* decrease the redox potential in solutions containing plutonium in a higher amount than cells of *Paenibacillus sp.* Both cell types have different strategies to handle the stress of plutonium. *Paenibacillus sp.* show a release of about 40% of the primary bound plutonium. An amount of 330 mg/L cells of *Sporomusa sp.* show nearly the same influence to the redox chemistry of plutonium as 11 mg/L sodium pyruvate. In presence of electron donors both strains of bacterial cells show an enrichment of Pu(III) (70%) in the biomass. Without electron donors Pu(IV)-polymers are predominant. Cells of *Sporomusa sp.* have a higher binding capacity for plutonium than cells of the *Paenibacillus sp.* strain.

The quantitative assessment of low dose radiotoxicity versus chemitoxicity has been demonstrated for the first time in living organisms. The metabolic heat dissipation of bacteria was measured as a function of the alpha activity of uranium isotopes and revealed non-lethal radiotoxic effects at low micromolar con-

centrations of ^{233}U that are equivalent to the chemi-toxicity of natural uranium at 100 fold higher concentrations. The microcalorimetric approach opens new approaches in correlating alpha energies at low doses with metabolic impact and genetics.

At the Institute of Resource Ecology the dominating surface species ($\equiv\text{FeO}$) $_2\text{NpO}_2(\text{H}_2\text{O})_3$ in the Np(V)-hematite system was identified by a combination of in-situ ATR FT-IR and EXAFS. Furthermore, for the first time the belonging complex formation constants could be described consistently with all published sorption data bases.

Beside these highlights, we obtained many other new scientific results in the past year, which are presented in this annual report. Furthermore, 60 original papers were published in peer-reviewed international scientific journals. In the year 2014, more than 120 scientists, technicians, and students working on their Ph.D., diploma, master, or bachelor thesis, were employed at the Institute of Resource Ecology. More than 30 Ph.D. students are working at the institute. Promotion of young scientists is an important requirement to ensure the competence and further scientific excellence in future times.

I would like to thank the visitors, German and international ones, for their interest in our research and for their participation in the institute seminars. We

would also like to thank our scientific collaborators and the visiting scientists for coming to Dresden – Rossendorf in 2014 to share their knowledge and experience with us. We will continue to strongly encourage the collaborations and visits by scientists in the future. Special thanks are due to the executive board of the HZDR, the Ministry of Science and Arts of the Free State Saxony (SMWK), the Federal Ministry of Education and Research (BMBF), the Federal Ministry of Economics and Technology (BMWi), the Deutsche Forschungsgemeinschaft (DFG), the European Commission, and other organizations for their support.

At the end of January, the large HGF strategic program evaluation for “NUSAFE” took place in Jülich and Düsseldorf. I would like to address cordial thanks to the high-ranked international review panel of this evaluation for taking the time and of course, for the given extraordinary good marks. As a result, we will be able to focus on our research with a planning reliability until 2020.



Prof. Dr. Thorsten Stumpf
Director of the
Institute of Resource Ecology

Contents

SCIENTIFIC CONTRIBUTIONS

PART I: LONG-LIVED RADIONUCLIDES IN BIOLOGICAL SYSTEMS

Isolated microorganisms from the flooding water of a former uranium mine in Königstein (Saxony, Germany) and their interactions with uranium.....	11
U. Gerber, E. Krawczyk-Bärsch, T. Arnold	
Biosorption studies of the halophilic archaea <i>Halobacterium noricense</i> DSM 15987 with uranium	12
M. Bader, A. Cherkouk	
Isotope-based calorimetric distinction of radio- and chemitoxicity of uranium in the model organism <i>Caenorhabditis elegans</i>	13
M. Obeid, S. Abu Sharkh, C. Erkut, J. Oertel, K. Fahmy	
Pu interaction with two bacterial isolates from Mont Terri Opalinus Clay at pH 6	14
H. Moll, L. Lütke, A. Cherkouk, G. Bernhard	
Speciation of europium and curium in human saliva	15
A. Barkleit, A. Heller	
A spectroscopic screening of the complexation of europium(III) in gastrointestinal tract: mouth and stomach.....	16
C. Wilke, A. Barkleit	
Femtosecond-TRLFS study of the Eu(III) interaction in a cell culture medium for mammalian cells.....	17
S. Sachs, G. Geipel	
Metal sorption behavior of Slp1 from <i>Lysinibacillus sphaericus</i> JG-B53 – A study of protein polymers and proteinaceous monolayers using QCM-D, ICP-MS, and AFM	18
M. Suhr, J. Raff, K. Pollmann	
Activity of immobilized atrazine-degrading <i>Pseudomonas</i> sp. ADP after long-term storage	19
M. Vogel, A. Pannier, J. Raff, K. Pollmann	

PART II: LONG-LIVED RADIONUCLIDES IN GEOLOGICAL SYSTEMS

A macroscopic and spectroscopic investigation of neptunium(V) adsorption on montmorillonite and corundum	23
O. Elo, N. Huittinen, K. Müller, A. Ikeda-Ohno, A. C. Scheinost, P. Hölttä, J. Lehto	
Complementary spectroscopic investigation of Np(V) sorption on birnessite	24
K. Müller, B. Simon, A. Rossberg	
Np(V) retention by magnetite.....	25
R. Steudtner, A. C. Scheinost	
Np(V)-ferrihydrite sorption complexes at high pH: An EXAFS Monte Carlo approach	26
A. Rossberg, K. Müller	
U(VI) surface complexation on montmorillonite at high ionic strengths	27
K. Fritsch, K. Schmeide	
The sorption behavior of U(VI) onto orthoclase and muscovite – Impact of U(VI) concentration and calcium ions	28
C. Richter, V. Brendler, K. Großmann	
Uranium(VI) sorption onto gibbsite: Increasing confidence in surface complexation models by combining spectroscopy and batch sorption experiments	29
F. Bok, K. Gückel	
Effects of the background electrolyte on Th(IV) sorption behavior.....	30
M. Schmidt, S. Hellebrandt, K. E. Knope, S. S. Lee, R. E. Wilson, J. E. Stubbs, P. J. Eng, L. Soderholm, P. Fenter	
Uptake of selenium by δ -alumina.....	31
C. Franzen, N. Jordan	
Effect of ionic strength on the adsorption of Tb^{3+} onto clay in the presence of fulvic acid	32
M. Poetsch, H. Lippold	

PART III: THE CHEMISTRY OF LONG-LIVED RADIONUCLIDES

Speciation studies of uranyl(VI) using PARAFAC and luminescence spectroscopy	35
B. Drobot, R. Steudtner, J. Raff, G. Geipel, V. Brendler, S. Tsushima	
How does uranium photochemically trigger DNA cleavage?	36
S. Tsushima, K. Fahmy	
The formation of intrinsic actinide colloids under nuclear waste repository conditions	37
H. Zänker, S. Weiss, C. Hennig, A. Ikeda-Ohno, V. Brendler	
Ionic strength dependency of the Eu(III)-(poly)borate complexation	38
J. Schott, J. Kretzschmar, M. Acker, A. Barkleit, S. Taut, V. Brendler	
Spectroscopic studies on the Eu(III)/Am(III)-oxalate systems at high ionic strengths.....	39
F. Taube, M. Acker, B. Drobot, S. Taut	
Lactate protonation and Eu(III)-lactate complexation studied by ITC (I = variable).....	40
F. Taube, M. Acker, S. Taut	
Complexation of trivalent <i>f</i> -elements with amides in solution	41
J. März, H. Moll, G. Geipel, K. Gloe	
The aqueous speciation of Se(IV): impact of concentration. Part 1: IR and MP2 studies.....	42
N. Jordan, J. Kretzschmar, E. Brendler, S. Tsushima, C. Franzen, H. Foerstendorf, K. Heim, V. Brendler	
The aqueous speciation of Se(IV): impact of concentration. Part 2: NMR studies	43
J. Kretzschmar, N. Jordan, E. Brendler, S. Tsushima, C. Franzen, H. Foerstendorf, K. Heim, V. Brendler	
β -Diketimate rare earth borohydride complexes: synthesis, structure, and catalytic activity in the ring-opening-polymerization of cyclic esters	44
M. Schmid, S. M. Guillaume, P. W. Roesky	

PART IV: STRUCTURAL INVESTIGATIONS ON SOLID SOLUTIONS

The influence of host cation size and crystal structure on Eu ³⁺ substitution in REPO ₄	47
N. Huittinen, Y. Arinicheva, J. Holthausen, S. Neumeier, T. Stumpf	
Determination of the local structure in La _{1-x} Eu _x PO ₄ solid solutions by EXAFS	48
M. J. Lozano-Rodriguez, Y. Arinicheva, S. Neumeier, A. C. Scheinost	
Structure investigation of U _x Th _(1-x) SiO ₄ solid solutions by EXAFS spectroscopy	49
C. Hennig, S. Weiss, H. Zänker, S. Labs, H. Curtius, D. Bosbach	

PART V: TRANSPORT PHENOMENA IN RESOURCE TECHNOLOGY

Direct observation of waterglass impregnation of fractured salt rock with positron emission tomography	53
L. Bittner, J. Kulenkampff, M. Gründig, F. Enzmann, J. Lippmann-Pipke	
Highly effective radiolabeling of commercial TiO ₂ nanopowder as a tool for sensitive nanoparticle detection.....	54
H. Hildebrand, S. Schymura, U. Holzwarth, N. Gibson, M. Dalmiglio, K. Franke	
Dynamics of metal-humate complexation equilibria: isotope exchange studies substantiate stabilization processes	55
H. Lippold	
Transport system for solid targets of the COSTIS-system mounted at the beam transfer line (BTL) of the Cyclone 18/9	56
K. Franke, J. Hauser	

PART VI: NUCLEAR REACTOR SAFETY RESEARCH

Modeling of the OECD/NEA large SFR core with Serpent-DYN3D and Serpent-PARCS code sequences	59
E. Nikitin, E. Fridman, K. Mikityuk	

Study of the impact from small shifts of fuel assemblies on the ex-core neutron flux.....	60
J. Konheiser, C. Brachem, M. Seidl	
Simulation of a boron dilution transient scenario in a PWR modeling coupled neutron kinetics, thermal hydraulics, and fuel rod behavior by the code system DYN3D-TRANSURANUS.....	61
U. Rohde, L. Holt, S. Kliem	
Implementation of the CCCP solver for pin-power reconstruction in DYN3D – First results	62
D. Litskevich, B. Merk	
Feasibility assessment of the once-through thorium fuel cycle for the PTVM LWR concept	63
R. Rachamin, E. Fridman, A. Galperin	
Accident analyses on a prismatic High Temperature Reactor	64
S. Baier, S. Kliem, M. Schreier	

**SPECIAL CONTRIBUTION:
THE GERMAN STUDY FOR PARTITIONING & TRANSMUTATION**

The German P&T study – Results and conclusions in the view of the contributing Helmholtz research centers.....	66
B. Merk, A. Geist, G. Modolo, J. Knebel	

PUBLICATIONS

▣ Articles (peer-reviewed).....	69
▣ Oral Presentations.....	73
▣ Patents	79
▣ Theses.....	79

SCIENTIFIC ACTIVITIES

▣ Seminars	83
▣ Workshops; (co)-organized by the IRE	84
▣ 2 nd International Workshop on Advanced Techniques for Actinide Spectroscopy (ATAS 2014).....	85
▣ Teaching Activities.....	88

PERSONNEL

89

ACKNOWLEDGEMENTS

95

INDEX OF AUTHORS

98

SCIENTIFIC CONTRIBUTIONS (PART I)

**LONG-LIVED RADIONUCLIDES IN
BIOLOGICAL SYSTEMS**

Isolated microorganisms from the flooding water of a former uranium mine in Königstein (Saxony, Germany) and their interactions with uranium

U. Gerber, E. Krawczyk-Bärsch, T. Arnold

In this work, we show that with a culture dependent method and a selected medium it is possible to isolate nine different microorganisms from the flooding water. The majority of these isolates were eukaryotes. The biosorption studies with uranium (U) showed that three isolates are able to immobilize high amounts of U in relative short times.

The former uranium mine Königstein in Saxony (Germany) is currently in the process of being flooded in a controlled way. As a consequence of acid leaching during uranium mining between 1976 and 1990, the flooding water is acidic as well as highly contaminated with heavy metals, such as uranium which is found at concentrations up to 10 mg/L. Previous studies showed that microorganisms may play an important role in this acid mine drainage (AMD) environments. Thus, we isolated different microorganisms from the flooding water and studied their sorption behavior towards uranium

EXPERIMENTAL. Flooding water (1 L) was vacuum filtered through a 0.2 µm cellulose acetate membrane, and subsequently plated on an agar plate containing SDA medium (sourbound dextrose agar). The agar plates were incubated at room temperature or at 28 °C for several days. For identification, the isolated microorganisms were grown in liquid SD medium and the DNA was extracted using the alkaline lysis method. [1]. Prokaryotes were identified by a part of the 16S rDNA gene which was amplified using the primers 27F (5'-AGAGTTTGATCCTGGCTCAG-3' [2]) and 1492R (5'-GGTACCTTGTACGACTT-3' [2]). For identification of eukaryotes, a part of the 18S rDNA gene was amplified using the primers EukA (5'-AACCTGGTTGATCCTGCCAGT-3' [3]) and EukBr (5'-TGATCCTTCTGCAGGTTACCTAC-3' [4]). The resulting amplicons were analyzed by agarose gel electrophoresis, purified and sequenced by GATC (Germany). For biosorption studies with U, the isolated microorganisms were grown in liquid SD medium and subsequently washed in the background medium used for the immobilization experiment. Afterwards, the cells were harvested by centrifugation and the uranium in the supernatant was determined by ICP-MS/OES.

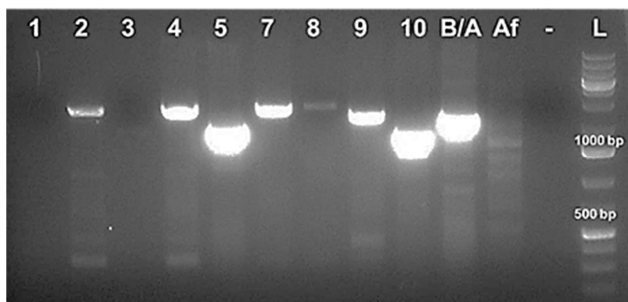


Fig. 1: Gel electrophoresis of the PCR amplicons with primers EukA and EukBr. The numbers display the different isolated microorganisms (KS1-KS10). B/A is the positive control and of the negative control.

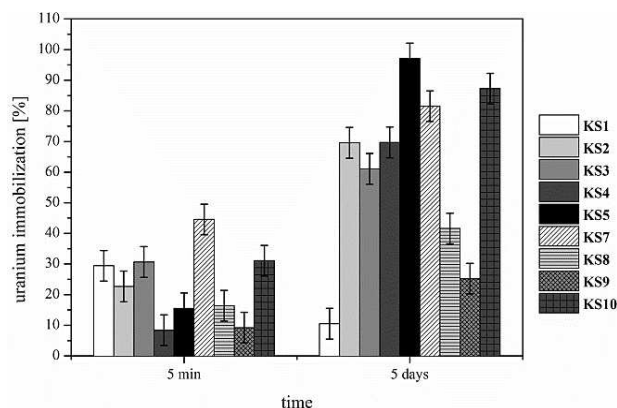


Fig. 2: Uranium immobilization by nine isolated microorganisms of the flooding water from Königstein. Initial uranium concentration: 24 mg/L. Background: tap water, pH 5.0.

RESULTS. Despite the high U concentration and the low pH a high biodiversity in the flooding water of the former U mine is found by culture independent methods (e.g., pyrosequencing) [5]. Nine different microorganisms were isolated by culture dependent method with SD medium. To identify the microorganisms, the amplicons of the PCR (Fig. 1) were sequenced by Sanger sequencing (GATC). The obtained sequence information was compared with available sequences at NCBI BLAST. The resulting amplicons with a size of about 1,500 bp represent the part of the 18S rDNA gene specific for eukaryotic microorganisms. The majority of the isolates were eukaryotic organisms. Studies of the interaction with U by the nine isolated microorganisms showed three candidates which are able to immobilize high amounts within a short time. Isolate KS7 is able to immobilize nearly 50% of the initial U concentration within the first 5 minutes (Fig. 2). After 5 days nearly 100% of the initially added U amount was immobilized by isolate KS5. Isolate KS10 also immobilizes high concentration of uranium. In summary, these three isolates are good candidates for further biosorption investigations.

The microscopic observations of the isolates KS5 as well as the sequencing results identified yeast cells of *Rhodospiridium toruloides*. The isolate KS7 is a mixed culture consisting of an Ascomycetes and the bacterium *Acidocella aromatica*. Also the microscopic pictures confirmed this. The sequencing results for the isolate KS10 displayed the sequence of the bacterium *Bacillus sp.* and also the microscopic investigations showed bacillary shaped cells.

ACKNOWLEDGEMENTS. This work was supported by the Bundesministerium für Bildung und Forschung (BMBF), project no. 02NUK030F. The authors are grateful to S. Gurlit and I. Kappler for ICP-MS measurements and K. Heim for ICP-OES measurements.

- [1] Tsai, Y. and Olson, B. (1991) *Appl. Environ. Microbiol.* **57**, 1070–1074.
- [2] Bond, P. L. et al. (2000) *Appl. Environ. Microbiol.* **66**, 3842–3849.
- [3] Aguilera, A. et al. (2010) *Int. Microbiol.* **13**, 21–32.
- [4] Aguilera, A. et al. (2006) *Syst. Appl. Microbiol.* **39**, 596–605.
- [5] Zirnstein, I. (2014) personal communication.

Biosorption studies of the halophilic archaea *Halobacterium noricense* DSM 15987 with uranium

M. Bader, A. Cherkouk

Biosorption studies of the halophilic archaea *Halobacterium noricense* DSM 15987 with uranium were performed at 3 M NaCl. This microorganism is indigenously in salt rock formations [1, 2] and demonstrated a good sorption capability of uranium at the studied conditions. Nearly 90% of the added uranium was sorbed after 48 h independent from radionuclide concentration and temperature. During biosorption, an agglomeration of the cells occurs depending on time, uranium concentration and temperature.

In Germany, crystalline, clay, and salt rock formations are considered as potential host rock systems for the long-term storage of radioactive waste in a deep geological repository. In the latter two formations high salt concentrations can occur. In salt rock, these concentrations are up to saturation and in the porewater of clay in the Northern part of Germany they can also reach up to 4.2 M [3]. Despite this extreme environment halophilic microorganisms are adapted to these conditions. Currently, little is known about their interactions with radionuclides which can include the change of the oxidation state, the speciation, and hence, the mobility of the radionuclides [4]. This information is of interest to improve the safety assessment of the repository.

In this study, the halophilic archaea *Halobacterium noricense* DSM 15987 was chosen to investigate its interactions with uranium due to its worldwide occurrence in salt rock formations [2]. Biosorption studies at pH 6 were performed depending on time, the uranium concentration, and temperature in batch experiments at 3 M NaCl.

EXPERIMENTAL. *Halobacterium noricense* DSM 15987 cells were cultivated in DSM 372 media at 37 °C and harvested in the mid exponential state after five days. The cells were washed three times with 3 M NaCl, pH 6. A defined amount of cells (0.5 mg L^{-1}) were resuspended in a solution of 3 M NaCl containing different U(VI) concentrations. During a certain incubation time, the cell suspension was stored in the dark on a shaker at room temperature and was subsequently centrifuged. The remaining U(VI) in the supernatant was determined by ICP-MS and the cells were visualized with a light microscope. All experiments were done in triplicates.

RESULTS. At pH 6, the biosorption of U(VI) showed a typical time-dependent behavior with a fast binding of U(VI) to the cells at the beginning (Fig. 1). After 3 h, 35% of the added U(VI) was bound to the cells. However, the maximal sorption was reached after 42 h where nearly 90% of the uranium was removed from the supernatant (Fig. 1). The accumulation kinetics indicated that a two-step process is occurring with a fast step within the first hours and a second slower step. In addition, we observed that the halophilic archaea bound approximately 90% of the U(VI) after 48 h irrespective of the concentration (10–100 μM). At a uranium concentration of 100 μM , $37.5 \pm 0.7 \text{ mg U(VI)}$ were bound to 1 g dry biomass. These results were also obtained at higher temperatures (30 °C and 50 °C).

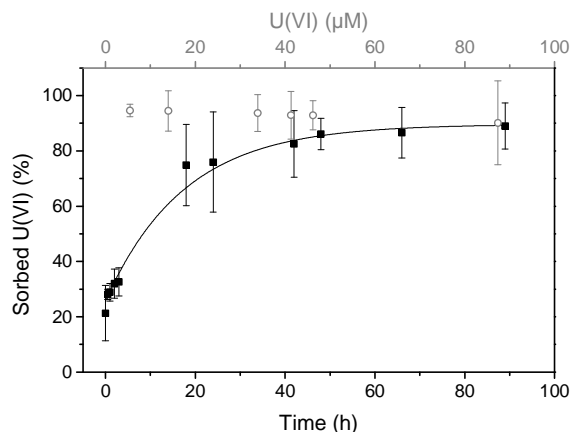


Fig. 1: Biosorption of uranium on *Halobacterium noricense* cells at pH 6, depending on time ([U(VI)] = 100 μM (full symbols, lower abscissa) and U(VI) concentration (t = 48 h (open symbols, upper abscissa)).

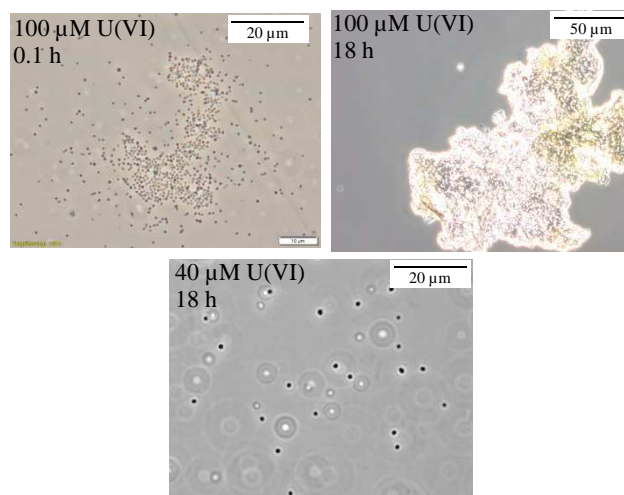


Fig. 2: *Halobacterium noricense* agglomeration depends on time and uranium concentration. After 0.1 h of biosorption with 100 μM U(VI) the cells began to agglomerate. After 18 h nearly all cells form agglomerates in contrast to biosorption with 40 μM U(VI), where the cells were single cells.

Depending on incubation time, uranium concentration, and temperature, an agglomeration of the cells was observed. As clarified in Fig. 2, the agglomeration is more pronounced with increasing uranium concentration and incubation time. Plating the cell suspension on agar plates, it could be demonstrated that even if agglomerates were formed the cells are still alive.

We assume that the cells secrete EPS (extra polymeric substances) represents an effective stress response of the cells to protect themselves from environmental challenges such as relatively high heavy metal concentrations or enhanced temperatures.

- [1] Gruber, C. et al. (2004) *Extremophiles*, p. 431–439.
- [2] Swanson, J. S. et al. (2012) *Status report Los Alamos National Laboratory*, p. 1.
- [3] Larue, J. (2010) *Abschlussbericht VerSi Endlagerung im Tonstein*, p. 34.
- [4] Francis, A. J. et al. (2009) *NUCAR02009*, p. 1

Isotope-based calorimetric distinction of radio- and chemitoxicity of uranium in the model organism *Caenorhabditis elegans*

M. Obeid, S. Abu Sharkh, C. Erkut,¹ J. Oertel, K. Fahmy

¹Max-Planck-Institute for Cell Biology and Molecular Genetics, Dresden, Germany

The assessment of low dose radiotoxicity is a major challenge in radioecology. Classical survival-based methods can hardly be applied because lethality is typically not affected under such environmentally realistic conditions. In contrast, metabolic responses to radio- and chemitoxicity may provide an extremely sensitive real-time monitor of detrimental effects of radionuclides. Here, we have established a minimal food chain model and used microcalorimetry to monitor the metabolic activity of the nematode *Caenorhabditis elegans* from hatching of the eggs up to the larval stage feeding on non-metabolizing bacteria. Since *C. elegans* is genetically fully characterized, such studies will ultimately allow correlating radiotoxicity with genetic traits. Already at 1 μM uranium, the increased α -activity of ^{233}U affects the metabolic activity of *C. elegans* as compared to natural uranium.

Two key issues in radioecology research concern the transit of radionuclides from the geosphere to the food chain and the distinction between the chemi- and radiotoxicity of radionuclides incorporated by an organism at low doses. To address both aspects, we have established a minimal food chain model using a bacterial strain of *E. coli* as a food source for the nematode *Caenorhabditis elegans*. *C. elegans* was chosen, because it is genetically fully characterized. The metabolic activity of the nematode was measured by its heat release during maturation of eggs and growth of the larval stage feeding on bacteria. These experiments were performed in the presence of varying concentrations of natural uranium and the ^{233}U isotope.

EXPERIMENTAL. The *C. elegans* strain N2 was obtained from the *Caenorhabditis* Genetics Center (Minneapolis, MN) and grown in nematode medium (NGM). Worms were bleached and 2000 eggs collected in 200 μM microcalorimeter ampoules supplemented with a non-metabolizing culture of *E. coli* strain N22. Natural uranium or ^{233}U was added from 10 mM uranyl nitrate stock solutions at final concentrations of 1–13 μM resulting in less than 0.01 Bq (at 4.27 MeV) and 17–261 Bq (at 4.91 MeV) per sample, respectively. Ampoules with eggs and controls with bacteria or NGM only were inserted in duplicates in a TAM-III microcalorimeter (TA-Instruments, Eschborn, Germany) and heat flow measured over five to six days.

RESULTS. Hatching of eggs is expected ~ 12 h after insertion of the samples into the calorimeter. The initial rise in heat flow can thus be assigned to growth of the first larval state L1 ending with the L1/L2 molt which we assign to the first peak in heat flow after ~ 27 h (Fig. 1 dotted line). The time course and the increase of heat flow during the L1 stage is little affected by the different uranium isotopes. However, the thermogram that covers the growth of the L2 larval stage after 36 h is clearly affected by the radionuclides if their concentration exceeds 1 μM . Natural uranium at 10 μM delays and decreases the peak metabolic activity which is typically observed 48 h. At the

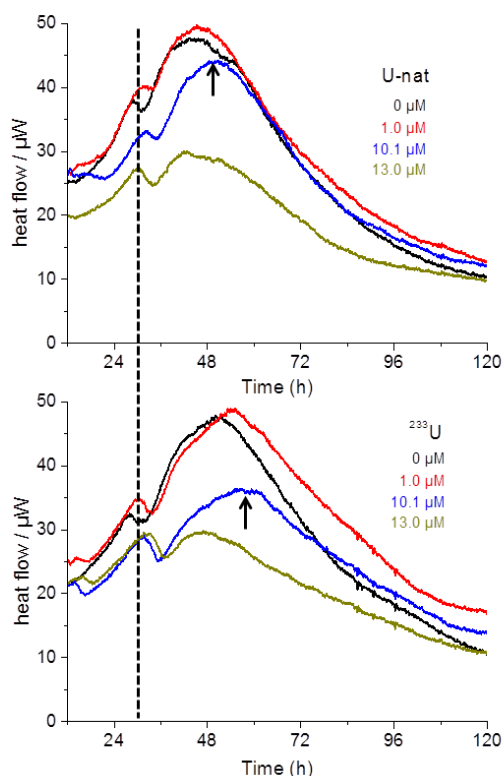


Fig. 1: Metabolic heat flow of developing *C. elegans* larvae in the presence of varying amounts of natural uranium (upper panel) and ^{233}U (lower panel). Dotted line: expected time for L1/L2 molt.

same concentration, ^{233}U is formally twice as effective as natural uranium with respect to both reduction and delay of the peak metabolic activity. Remarkably, a prolonged heat production of the culture is obvious beyond 60 h, (growth of the L3 stage) already at 1 μM ^{233}U but not with natural uranium. Since non-metabolizing conditions for the bacteria were chosen (no carbon source), the thermograms are attributable to the nematode metabolism. The data show that microcalorimetry allows a highly sensitive distinction of radio- and chemitoxic effects in a multicellular organism within a well controllable minimal food chain. Since *C. elegans* responds physiologically and morphological to different stress situations, we will particularly address the effect of radionuclides during formation of draught-resistant dauer state, where heavy metals may get further concentrated. We have shown that under these conditions lipid headgroups are altered to interact preferentially with a cryo-protective disaccharide-trehalose [1]. Molecular mechanisms of cellular uranyl uptake are expected to critically depend on the metal-coordinating properties of these membrane constituents which will be further studied *in vitro* to complement the *in vivo* data.

CONCLUSIONS. A minimal food chain has been established that allows assessing low dose chemi- and radiotoxicity by metabolic monitoring of genetically fully described organisms.

[1] Abu Sharkh, S. et al. (2014) *Langmuir* **30**, 12897–12906.

Pu interaction with two bacterial isolates from Mont Terri Opalinus Clay at pH 6

H. Moll, L. Lütke,¹ A. Cherkouk, G. Bernhard

¹Institut für Radioökologie und Strahlenschutz (IRS), Leibniz Universität Hannover, Hannover, Germany

At pH 6, a moderate to strong impact of *Sporomusa* sp. and *Paenibacillus* sp. cells on the Pu speciation was observed. In contrast to the electron donor free experiments, a clear enrichment of Pu(III) in the biomass (bioreduction) was observed in the presence of 10 mM Na-pyruvate.

In this study, the unknown interaction between two bacterial isolates from Mont Terri Opalinus Clay [1], *Sporomusa* sp. MT-2.99 and *Paenibacillus* sp. MT-2.2, and plutonium were explored in aqueous solution at pH 6 [2]. The time-dependent Pu concentrations measured in the supernatants were successfully fitted with bi-exponential decay functions. The time-dependent Pu oxidation state distributions were successfully fitted by using mono-exponential decay or growth functions.

EXPERIMENTAL. *Sporomusa* sp. MT-2.99 and *Paenibacillus* sp. MT-2.2 cells were cultured anaerobically in R2A medium at 30 °C. Cells were harvested in the mid-exponential growth phase, washed and suspended in 0.9% NaCl solution containing 10⁻⁴ M Na-pyruvate. The experiments were performed anaerobically at dry biomass concentration of 0.33 g_{dry weight}/L and pH 6 at 25 °C in 0.1 M NaClO₄ solution with and without 10 mM Na-pyruvate as an electron donor. [²⁴²Pu]_{initial} was varied between 0.2 and 110 mg/L. The ²⁴²Pu present in a) blank (no cells added), b) supernatant, and c) washed biomass re-suspended in 1 M HClO₄ were analyzed using UV-vis-NIR spectroscopy, solvent extraction, and liquid scintillation counting (LSC) as described in [3].

RESULTS. If no electron donor was added, the biomass interacted with a Pu solution containing mainly Pu(VI) (60%), Pu(IV)-polymers (19%), and Pu(V) (12%). Due to the reducing properties of 10 mM Na-pyruvate, here the composition of the starting Pu solution was 35% Pu(V), 26% Pu(IV), 22% Pu(IV)-polymers, 10% Pu(III), and only 4% Pu(VI).

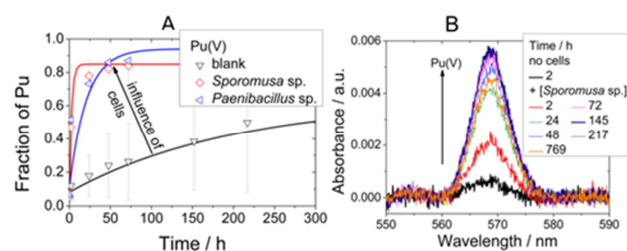


Fig. 1: A) Averaged time-dependent Pu(V) distribution in 0.1 M NaClO₄ at pH 6. B) Absorption spectra of Pu ([²⁴²Pu]_{initial} = 110 mg/L) at pH 6 after different contact times with 0.33 g/L of *Sporomusa* sp. MT-2.99 after separating the cells by centrifugation.

The Pu sorption capacity of *Sporomusa* sp. is slightly higher (118 mg Pu/g_{dry weight}) than that of *Paenibacillus* sp. cells (87 mg Pu/g_{dry weight}). In the electron donor containing system (data not shown) faster kinetics especially for *Sporomusa* sp. were found. It seems that *Paenibacillus* has a slightly different strategy to avoid the stress caused by Pu. After 2 h of contact time, the cells released 40% of this bound Pu. At contact times ≥ 24 h, an exponential de-

crease of the Pu concentration in solution was detected. This phase of the release of biosorbed Pu from the cells was prolonged in the presence of 10 mM Na-pyruvate.

In the *Sporomusa* sp. system, the redox potential measurements indicated that the cells generated reducing conditions. In the blank sample at $t \geq 312$ h a redox potential of 790 ± 73 mV was measured. In the cell suspensions immediately a constant value of 331 ± 25 mV was reached. *Paenibacillus* sp. cells were less effective in minimizing the redox potential. The cell induced effect on the redox potential is smaller in the presence of 10 mM Na-pyruvate.

In the electron donor free experiments a very fast decrease of Pu(VI) (data not shown) was observed which was combined with an increase of Pu(V) (Fig. 1A) in the biomass suspensions. *Sporomusa* sp.: The formation of Pu(V) in the supernatants is 75 times faster than in the blank samples. *Paenibacillus* sp.: The formation of Pu(V) in the supernatants is 10 times faster than in the blank samples. The decrease of Pu(VI) and the increase of Pu(V) (see Fig. 1B) was confirmed by absorption spectroscopy.

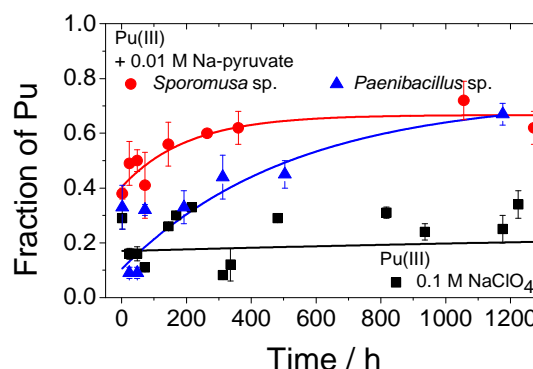


Fig. 2: Averaged time-dependent Pu(III) distribution in the biomass.

There was a clear enrichment of Pu(III) in the biomass in the presence of 10 mM Na-pyruvate (Fig. 2). Pu(IV)-polymers associated on biomass dominated in 0.1 M NaClO₄. The formation of Pu(III) was in the *Sporomusa* sp. system three times faster than in the *Paenibacillus* sp. system.

OUTLOOK. For a better understanding of the interaction processes further experiments for instance as a function of pH or varying the electron donor are planned.

ACKNOWLEDGEMENTS. The authors thank the BMWi for financial support (contract no.: 02E10618 and 02E10971), Velina Bachvarova and Sonja Selenska-Pobell for isolation and Monika Dudek for cultivation of the bacteria, as well as the BGR for providing the clay samples.

- [1] Bachvarova, V. (2009) *Report FZD-530*, p. 18.
- [2] Moll, H. et al. (2014) lecture given at the Plutonium Futures – The Science 2014, September 07–12, 2014, Las Vegas, U.S.A.
- [3] Moll, H. et al. (2006) *Radiochim. Acta* **94**, 815–824.

Speciation of europium and curium in human saliva

A. Barkleit, A. Heller

The speciation of Eu^{3+} and Cm^{3+} in saliva was investigated with Time-Resolved Laser-Induced Fluorescence spectroscopy (TRLFS). Fresh human saliva samples have been spiked in vitro with Eu^{3+} or Cm^{3+} . A comparison of the obtained spectral data with reference data indicates the formation of complexes containing phosphate and carbonate as well as calcium for charge compensation. Furthermore, the complexation with α -amylase is also suggested.

Understanding of the speciation of radionuclides in body fluids is fundamental to assess their potential transport and metabolism in human organisms. As saliva is the first contact medium in the mouth in case of oral ingestion of radioactively contaminated food or radioactive substances themselves, this study focuses on the speciation of Eu^{3+} and Cm^{3+} in human saliva.

EXPERIMENTAL. Ten human saliva samples were collected from healthy adult volunteers and were analyzed by ICP-MS and ion chromatography. TRLFS measurements were performed at room temperature with human and artificial saliva and reference solutions containing representative electrolytes. All samples were spiked with 3×10^{-5} M Eu^{3+} or 3×10^{-7} M Cm^{3+} .

RESULTS. The composition of saliva is summarized in Tab. 1. Here we consider sodium, potassium, and calcium as major inorganic cations, while the anions phosphate, carbonate, and chloride as well as the total organic carbon are taken into account because of their strong coordination ability to Eu^{3+} and Cm^{3+} . The composition of artificial saliva is based on the average data of the analyzed human saliva and literature values [1]. The enzyme α -amylase (Amy) was chosen as a major protein in saliva [1].

Tab. 1: Composition of human and artificial saliva.

Inorganic (mmol/L)						Organic
Na^+	K^+	Ca^{2+}	Cl^-	Phosphate	Carbonate	TOC (g/L)
Human saliva						
3–9	3–21	1–2	10–12	4–6	3–8	0.5–1
Artificial saliva						
10	4.5	1.0	4.0	4.0	4.5	1.0 (Amy)

As shown in Fig. 1, the shape of Eu^{3+} and Cm^{3+} luminescence spectra appears to be similar regardless of the samples. Their luminescence decay was found to be bi-exponential, indicating that at least two different Eu/Cm species are present in these saliva samples. For Eu^{3+} , a major luminescence lifetime was determined to be 372–815 μs with a second shorter lifetime of 125–302 μs , while lifetimes of 484–563 μs and 104–224 μs were found for Cm^{3+} .

In case of Eu^{3+} , mixtures with only the inorganic components fit the luminescence spectra of Eu^{3+} in human saliva (Fig. 2). The addition of α -amylase in the mixture did not change the spectra, which indicates that Eu^{3+} is mainly coordinated by inorganic ions. However, the luminescence lifetime of Eu^{3+} in the inorganic mixture was found to be mono-exponential, while it became bi-exponential

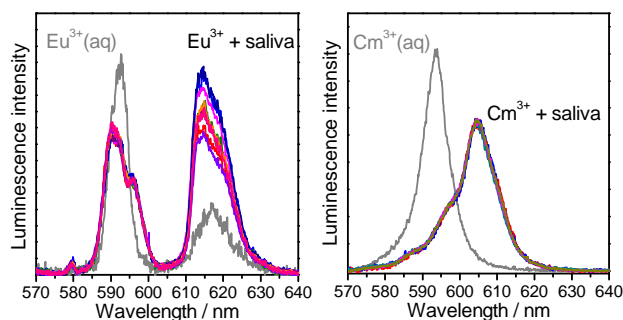


Fig. 1: Luminescence spectra of Eu^{3+} (3×10^{-5} M, left) and Cm^{3+} (3×10^{-7} M, right) in human saliva (pH = 6.8–7.4). Excitation wavelengths $\lambda = 394$ nm (Eu) and $\lambda = 396$ nm (Cm).

after the addition of α -amylase comparable to the human saliva. This is a strong hint that this protein is potentially coordinative to Eu^{3+} . Additional investigations with inorganic references showed that the presence of carbonate and phosphate in combination with calcium fits best the Eu^{3+} luminescence spectra in the human saliva. Similar complexes with multiple ligands were also identified earlier for urine with near-neutral pH values, where Eu^{3+} is coordinated by phosphate and calcium as well as carbonate and citrate as an organic component [2].

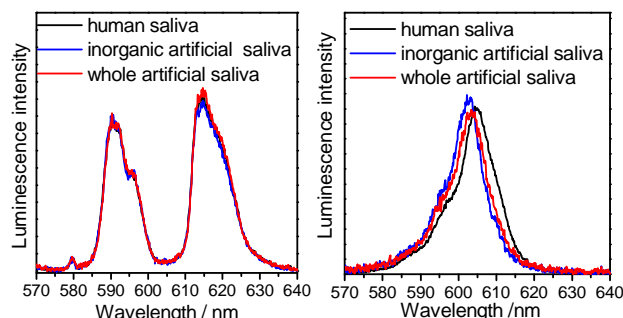


Fig. 2: Luminescence spectra of Eu^{3+} (3×10^{-5} M, left) and Cm^{3+} (3×10^{-7} M, right) in human and artificial saliva (pH = 7.0). Excitation wavelengths $\lambda = 394$ nm (Eu) and $\lambda = 396$ nm (Cm).

In case of Cm^{3+} , the luminescence spectra are more sensitive to the primary coordination sphere. Here, neither the luminescence spectra nor the luminescence lifetimes of Cm^{3+} in the human saliva could be reproduced with the reference spectra containing only inorganic ligands. When α -amylase is taken into account on the fitting, the lifetimes converge, but the luminescence spectra are not completely reproducible. This suggests that other saliva components are involved in the complexation with Cm^{3+} .

ACKNOWLEDGEMENT. This work was funded by the Federal Ministry of Education and Research (BMBF, project “TransAqua”, 02NUK030F).

- [1] Edgar, W. M. (1992) *Br. Dent. J.*, **172**, 305–312.
 [2] Heller, A. et al. (2011) *Chem. Res. Tox.* **24**, 193–203.

A spectroscopic screening of the complexation of europium(III) in gastrointestinal tract: mouth and stomach

C. Wilke, A. Barkleit

For the identification of the main binding partners (i.e. counter ions and/or ligands) of An/Ln in the gastrointestinal tract, a spectroscopic screening was performed by Time-Resolved Laser-Induced Fluorescence Spectroscopy (TRLFS) using artificial digestive juices containing Eu(III). The results indicate that Eu(III), a representative of Ln(III)/An(III), is coordinated to inorganic species in the saliva, whereas it primarily exists as an aquo species in the gastric juice.

In general, the lanthanide and actinide elements play no essential roles in biochemistry. However, through different processes such as nuclear accidents, these heavy metals could be potentially released into the environment where they could be incorporated into the food chain and eventually into the human body through oral ingestion. Because of the chemical toxicity and radiotoxicity of An, it is important to understand their chemical and biological behavior *in vivo*. This study focuses particularly on the biochemical behavior of An/Ln in the gastrointestinal tract. As an initial step, the first spectroscopic screening was performed to find possible binding partners of An(III)/Ln(III) in the gastrointestinal system (i.e. saliva and gastric juice).

EXPERIMENTAL. The *in vitro* digestion model used in this study was developed by Oomen *et al.* [1] and is the basis of an international unified bioaccessibility protocol [2]. This gastrointestinal model simulates the mouth, stomach and small intestine and is based on the human physiology. The compositions of the investigated digestive juices are shown in Tab. 1. Dissolved 1×10^{-5} M $\text{EuCl}_3 \cdot 6\text{H}_2\text{O}$ was added to single constituents and different mixtures of saliva and the gastric juice. TRLFS measurements of the prepared samples were carried out at room- and body temperatures (37 °C).

RESULTS. *Saliva:* The TRLFS spectra of Eu(III) in the saliva are shown in Fig. 1. The proteins (i.e. amylase and

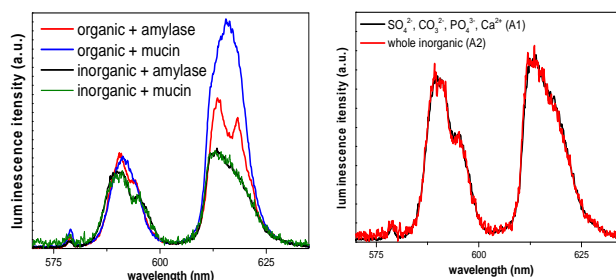


Fig. 1: Luminescence spectra of Eu(III) (1×10^{-5} M) in artificial saliva at 37 °C and pH 6.5.

mucin) show a strong complexation with Eu(III) in the presence of organic substances. This is, however, suppressed in the presence of inorganic ions. The addition of proteins in the samples “inorganic + amylase” or “inorganic + mucin” in Fig. 1 has no significant influence on the luminescence spectra. However, there is change in the luminescence lifetimes calculated for the protein samples, suggesting a minor contribution of proteins to the complexation with Eu(III). In contrast the organic compounds urea and uric acid have no effect on the luminescence spectra or lifetimes. So in the saliva the inorganic species, especially bicarbonate, phosphate and calcium, and with a minor effect also sulfate, are likely to change the Eu(III) speciation.

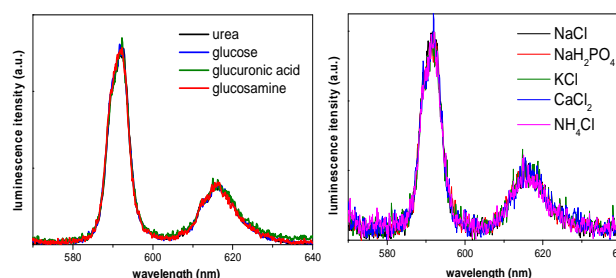


Fig. 2: Luminescence spectra of Eu(III) (5×10^{-5} M) in the presence of organic (left) and inorganic species (right) in gastric juice at 37 °C and pH 1.

Gastric Juice: TRLFS results indicate that there is no significant complex formation of Eu(III) with any constituents of the gastric juice. That is, Eu(III) is present primarily as aquo species (see Fig. 2). This is probably due to the acidic condition of the gastric juice (pH 0.9–1.0).

OUTLOOK. The speciation of Eu(III) will be further investigated in the intestine and bile juice. After the spectroscopic screening, the main binding partners of Eu(III) in the whole gastrointestinal tract will be identified and characterized.

ACKNOWLEDGEMENT. This work was funded by the Federal Ministry of Education and Research (02NUK030F).

Tab. 1: Composition and concentration of the synthetic saliva and gastric juice [1, 2].

	Saliva	Gastric Juice
Inorganic substances	24.0 mM KCl	94.2 mM NaCl
	14.8 mM NaH_2PO_4	22.1 mM KCl
	15.0 mM KHCO_3	11.4 mM NH_4Cl
	10.2 mM NaCl	5.4 mM CaCl_2
	8.0 mM Na_2SO_4	3.9 mM NaH_2PO_4
	4.1 mM KSCN	
	1.0 mM CaCl_2	
	Organic substances	6.7 mM urea
0.1 mM uric acid		2.8 mM urea
		3.1 mM glucosamine hydrochlorid
		0.2 mM glucuronic acid
Proteins	1 mg/mL amylase	3 mg/mL mucin
	0.5 mg/mL mucin	1 mg/mL pepsin
		1 mg/mL BSA
pH	6.5 ± 0.5	0.9–1.0

[1] Oomen, A. G. *et al.* (2003) *Arch. Environ. Contam. Toxicol.* **44**, 281–287.

[2] Wragg, J. *et al.* (2009) *British Geological Survey Open Report OR/07/027*.

Femtosecond-TRLFS study of the Eu(III) interaction in a cell culture medium for mammalian cells

S. Sachs, G. Geipel

Femtosecond (fs)-TRLFS was applied to determine an apparent complex stability constant for the interaction of Eu(III) with serum proteins in a cell culture medium for mammalian cells.

Previously, we studied the interaction of Eu(III) with mammalian cells as a function of its speciation. The Eu(III) speciation was investigated by solubility studies, ultrafiltration, ultracentrifugation, and time-resolved laser-induced fluorescence spectroscopy (TRLFS). In the presence of fetal bovine serum (FBS), Eu(III) is stabilized in solution and forms ternary complexes involving serum proteins and carbonate [1]. In the present work, we studied the interaction of Eu(III) in a cell culture medium applying femtosecond laser pulse based TRLFS (fs-TRLFS) which allows the analysis of the fluorescence behavior of the organic nutrient constituents in the presence of Eu(III).

EXPERIMENTAL. Eu(III) samples were prepared under ambient conditions ($p_{\text{CO}_2} = 10^{-3.5}$ atm) at room temperature by dilution of aqueous EuCl_3 stock solutions (0.05 and 0.1 M) with cell culture medium, consisting of 89.5 % v/v Dulbecco's modified eagle medium (DMEM; Biochrom), 10 % v/v fetal bovine serum (FBS; Sigma), and 0.5 % v/v penicillin/streptomycin (50 U/mL/50 $\mu\text{g/mL}$; Biochrom). The Eu(III) concentration was varied between 0 and 2×10^{-3} M, whereas the nutrient concentration was held constant. The pH values of the solutions were adjusted to $\text{pH } 7.40 \pm 0.02$ using NaOH and HCl. A fs-TRLFS system was applied with an excitation wavelength of 406 nm and pulse energies of about 0.2 μJ . fs-TRLFS spectra were measured in the wavelength range between 376 and 583 nm at delay times between 0 and 100 ns (1 ns time steps).

RESULTS. Time-resolved fluorescence spectra of the organic constituents of the nutrient were measured at varying Eu(III) concentrations. For data evaluation, the spectra at $t = 0$ ns relative to the laser pulse were integrated in the wavelength range between 450 and 550 nm. Figure 1 shows the resulting data as a function of the Eu(III) concentration. Up to about 1.5×10^{-3} M Eu(III), an increase of the fluorescence intensity is observed with increasing Eu(III) concentration, indicating the complexation of Eu(III) by nutrient constituents. With further increasing Eu(III) concentration, the fluorescence intensity approaches an almost constant value pointing to a completion of the Eu(III) complexation. An enhancement of fluorescence intensities due to complex formation was also reported in the literature, for instance, for the complexation of Al^{3+} with fulvic acid [2].

Evaluating the obtained data according to Eq. (1), the concentration of the free ligand (C_L), the Eu(III) complex (C_C), and the non-complexed Eu(III) species in solution can be deduced (I_M : measured fluorescence intensity, I_L^0 : fluorescence intensity at $[\text{Eu}] = 0$ M normalized to the total ligand concentration $C_{L,0}$, I_M^0 : fluorescence intensity at maximum complex concentration normalized to $C_{L,0}$).

$$C_L \times I_L^0 + C_C \times I_C^0 = I_M \quad (1)$$

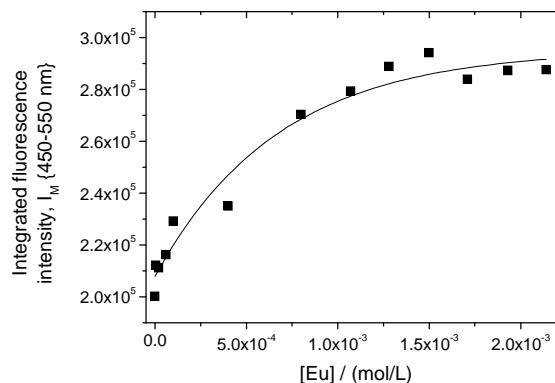


Fig. 1: Integrated fluorescence intensity between 450 and 550 nm as a function of the Eu(III) concentration (delay time $t = 0$ ns).

Based on TRLFS results [1], the formation of a 1:1 complex of an Eu(III) species with serum proteins is assumed. However, due to the complexity of FBS, the complexing proteins are not known, which complicates the specification of the total molar protein concentration. On average, the total protein content of FBS amounts to 38 g/L [3], i.e., the protein concentration in the used medium is 3.8 g/L. Bovine serum albumin (BSA; ~66 kDa) represents the main protein component in FBS (2.3 g/L [3]), therefore, a mean molecular mass of 70 kDa is assumed for calculation of the molar protein concentration in solution. Based on these assumptions we obtained an apparent complex stability constant of $\log K_{app} = 3.90 \pm 0.24$, which represents a mean value for the interaction of Eu(III) with one or more serum proteins. Slope analysis resulted in a slope of 1.1 ± 0.2 verifying the assumed 1:1 complexation. Comparing $\log K_{app}$ with literature data, this value is close to those reported for the complexation of Gd(III) with BSA ($\log K = 3.89$ [4]), however, differs from those of Eu(III) with apo-transferrin ($\log K_f = 7.97 \pm 0.02$ [5]) or human serum ($\log K = 6.25 \pm 0.10$ [6]).

TRLFS revealed the formation of ternary Eu(III) complexes involving serum proteins and carbonate ligands [1]. Under consideration of the Eu(III) carbonate complexation, a higher complex stability can be expected. However, in order to determine this, more information about the Eu(III) speciation in the complex cell culture medium as well as about the kind of the complexing ligands are necessary.

ACKNOWLEDGEMENTS. We thank J. Seibt and S. Heller for sample preparation and S. Gurlit for ICP-MS analyses.

- [1] Sachs, S. et al. (2015) *Toxicol. In Vitro*, submitted.
- [2] Ryan, D.K. et al. (1996) in: *Humic and fulvic acids. Isolation, structure, and environmental role*, p.125–139, American Chemical Society, Washington.
- [3] Lindl, T., Gstraunthaler, G. (2008) *Zell- und Gewebekultur*, Spektrum Akademischer Verlag, Heidelberg.
- [4] Reuben, J. (1971) *Biochemistry* **10**, 2834–2838.
- [5] Sturzebecher-Hoehne, M. et al. (2013) *J. Am. Chem. Soc.* **135**, 2676–2683.
- [6] Schomäcker, K. et al. (1988) *Appl. Radiat. Isot.* **39**, 261–264.

Metal sorption behavior of Slp1 from *Lysinibacillus sphaericus* JG-B53 – A study of protein polymers and proteinaceous monolayers using QCM-D, ICP-MS, and AFM

M. Suhr,¹ J. Raff,¹ K. Pollmann¹

¹Helmholtz-Zentrum Dresden – Rossendorf, Helmholtz-Institute Freiberg for Resource Technology, Dresden, Germany

In this study, the adsorption of selected noble metals and rare earth elements by surface layer (S-layer) proteins were investigated. For this, the sorption behavior of protein polymers was investigated by using inductively coupled plasma mass spectrometry (ICP-MS) and on proteinaceous monolayers by using quartz microbalance with dissipation monitoring (QCM-D). Subsequent atomic force microscopy (AFM) studies enable the imaging of the nanostructures and allow exact statements on structural properties.

S-layers are biological compounds which are part of the cell envelope of many bacteria and nearly all archaea [1]. These compounds have remarkable properties like self-assembling in highly ordered lattices, high metal-binding capacities and high stabilities. This makes them interesting for several bio-based technical applications such as biosorptive materials for metal removal or recovery from the environment [1, 2]. In this work, the sorption of Au, Pd, Pt, and Eu by S-layer of *Lysinibacillus sphaericus* JG-B53 (Slp1) was investigated by QCM-D which enables the detection in real-time during in-situ experiments. The suitability of this technique for the nanoscaled detection of S-layers has been shown successfully in previous studies [3–5]. The comparison between different methods allowed a deeper understanding of the metal sorption of isolated S-layers either free in liquid, adsorbed as a proteinaceous monolayer or as present on the bacterial surface.

EXPERIMENTAL. Slp1 of JG-B53 was isolated as described previously [5]. Purified and freeze-dried Slp1 (1 g/L) was diluted and used for sorption experiments. All sorption experiments were done in 0.9% NaCl solution at pH = 6.0 using 1 mM Au³⁺, Eu³⁺, Pd²⁺ or Pt²⁺. Metal content in supernatant was determined by ICP-MS (SCIEX ELAN 6100/9000, PerkinElmer, Germany). For QCM-D measurements (Q-Sense E4, Q-Sense AB, Sweden) 0.2 g/L of solubilized Slp1 were recrystallized on polyelectrolyte (PE) modified SiO₂ sensors in buffer (1.5 mM TRIS, 10 mM CaCl₂, pH = 8.0) and rinsed with 0.9% NaCl solution before metal adsorption. Experiments were done in flow mode (125 μL/min, 25 °C) and Q-Tool 3 was used for data modeling [5]. AFM imaging (MFP-3D Bio, Asylum Research, USA) was done using Olympus OMCL AC40 cantilever in AC mode in liquid.

RESULTS. ICP-MS indicates high metal sorption rates (q_{\max}) and removal efficiencies (RE) of Pd, followed by Au, Eu, and Pt to the Slp1 polymers (Tab. 1) [5]. This metal binding is believed to be mainly induced by the chemical functional groups (NH₂ and COOH) available in the primary structure of Slp1 sequence [6]. QCM-D experiments have shown that the metal adsorp-

Tab. 2: Adsorption of metals (1 mM, pH = 6.0) on recrystallized Slp1.

Metal cation	Kelvin-Voigt		Sauerbrey	
	Δm_{\max} (ng/cm ²)	$m_{\text{on sensor}}$ (ng)	Δm_{\max} (ng/cm ²)	$m_{\text{on sensor}}$ (ng)
Au ³⁺	955 ± 2.7	3000.2 ± 8.5	932.6 ± 2.9	2929.9 ± 9.1
Eu ³⁺	N.D.*	N.D.*	N.D.*	N.D.*
Pd ²⁺	269.8 ± 0.6	847.7 ± 1.3	269.9 ± 0.6	847.9 ± 2.2
Pt ²⁺	N.D.**	N.D.**	N.D.**	N.D.**

N.D.* = not detectable; N.D.** = Slp1 layer detachment.

tion to Slp1 monolayer was completed after 60 min. Almost stable signals in frequency and dissipation were recorded and even intensive rinsing with NaCl solution does not lead to a metal desorption from the Slp1 lattice in case of Au³⁺ and Pd²⁺ studies. Adsorption of Eu³⁺ was below the detection limit of the device. A detection of the Eu³⁺ binding is additionally impeded, as Eu³⁺ replaces bound Ca²⁺. Pt²⁺ studies have shown destabilizing effects in the recrystallized 2D protein lattice, preventing metal sorption and explaining the low binding affinity also detected by ICP-MS. The calculated mass adsorption (Kelvin-Voigt and Sauerbrey model) on the recrystallized Slp1 lattices are summarized in Tab. 2.

AFM-studies have proven an intact protein lattice of Slp1 on PE-modified SiO₂ sensor after the exemplarily incubation with a 1 mM gold metal salt solution (Fig. 1). The stability of Slp1 monolayer against Au³⁺ and the almost complete desorption of protein lattice seen in QCM-D studies of Pt²⁺ could be visualized via AFM imaging.

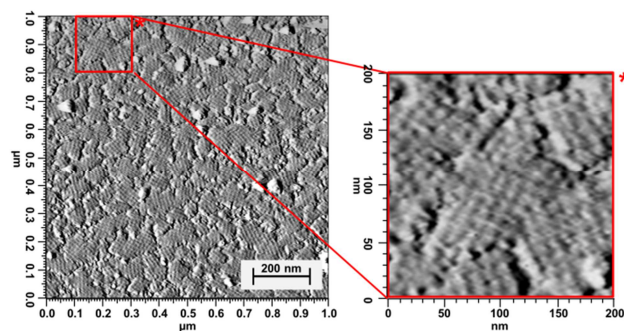


Fig. 1: AFM Slp1 lattice (*p4*-symmetry) after incubation with Au³⁺ solution and magnification of marked region.

CONCLUSION. By combination of ICP-MS, QCM-D, and AFM methods a deeper knowledge of protein-metal interaction on a nanometer scale could be reached. High q_{\max} of Slp1 either free in liquid or as a recrystallized monolayer for Au³⁺ and Pd²⁺ and lower capacities for Pt²⁺ and Eu³⁺ were obtained at slightly acidic pH. Subsequent AFM studies were successfully used to show the metal influence to the Slp1 monolayer stability.

Tab. 1: Metal sorption rate (q_{\max}) and removal efficiency (RE) of Slp1.

	Eu ³⁺	Au ³⁺	Pd ²⁺	Pt ²⁺
q_{\max} (mg/g)	6.80	74.67	71.84	12.31
RE (%)	10.34	37.91	67.51	6.31

- [1] Sleytr, U. B. et al. (2001) *Progr.Surf. Sci.* **68**, 231–278.
- [2] Lopez A. E. (2010) *Small* **6**, 396–403.
- [3] Toca-Herrera, J. L. et al. (2005) *Small* **1**, 339–348.
- [4] Suhr, M. et al. (2012) *Report HZDR- 013*, p. 26.
- [5] Suhr, M. et al. (2014) *Biometals* **27**, 1337–1349.
- [6] Lederer, F. L. et al. (2013) *Microbiology* **159**, 1097–1108.

Activity of immobilized atrazine-degrading *Pseudomonas* sp. ADP after long-term storage

M. Vogel, A. Pannier,¹ J. Raff, K. Pollmann²

¹GMBU e. V., Dresden, Germany; ²Helmholtz-Zentrum Dresden – Rossendorf, Helmholtz Institute Freiberg for Resource Technology, Freiberg, Germany

The atrazine-degrading bacterial strain *Pseudomonas* sp. ADP was immobilized by the sol-gel process within thin silica layers coated onto water-retaining carrier materials (expanded clay pellets and scoria). The performance of the obtained biohybrid material has been investigated concerning activity under non-growth conditions after long-term storage. Even after 6 month of storage without nutrition the immobilized cells were able to degrade atrazine.

This study focuses on the development of innovative biohybrid materials for biotechnological applications, e. g. for the removal of harmful organic substances from water. For example the efficient removal of residues of the s-triazine herbicide atrazine in environmental soil and water is of considerable interest. As an alternative to conventional often expensive removal methods biological degradation of atrazine by *Pseudomonas* sp. ADP (*P. ADP*), being one of the fastest atrazine degrading bacterial strains, is considered. To use the capability of atrazine-degrading *P. ADP* for remediation, the cells have to be prevented from being washed out as well as protected from physical and chemical damage. Cell immobilization could therefore be advantageous. Additionally, a suitable immobilization matrix offers the possibility of long-term storage of the biohybrid material by preserving viability and degradation activity of the immobilized cells over several months.

EXPERIMENTAL. Cultivation of the bacterial strain *Pseudomonas* sp. ADP, synthesis of silica nanosols, immobilization procedure of bacterial cells and the characterization of the carrier material are described in Pannier et al. [1]. Biohybrid materials were stored within tightly closed screw cap bottles under humid conditions at 4 °C. After storage for differing time intervals, the atrazine-degradation activity was investigated according to the initial atrazine degradation experiments conducted directly after immobilization. Onto clay (2 g) and scoria (4.4 g) immobilized *P. ADP* were cultivated in 30 mL of phosphate buffer (20 mM, pH 7.4) with 20 mg L⁻¹ atrazine (BPA) solution and samples for atrazine analysis were taken at specific periods of time. Atrazine degradation was monitored by HPLC analysis [1].

RESULTS. As previous studies showed, sol-gel immobilized *P. ADP* cells are actively degrading atrazine under non-growth conditions over one year [1]. The biohybrid materials were now tested regarding atrazine degrading ability after long-term storage in humid atmosphere. Although, both carrier materials show high water retaining capabilities they differ to some extent in in pore structure and open pore volume which might influence efficiency of cell immobilization and subsequent diffusion of nutrients. For example clay showed a 3 times higher total open pore volume compared to scoria, further details of material characteristics are described in [1].

As shown in Fig. 1, both materials show atrazine degradation after storage at 4°C for up to six month. With cells

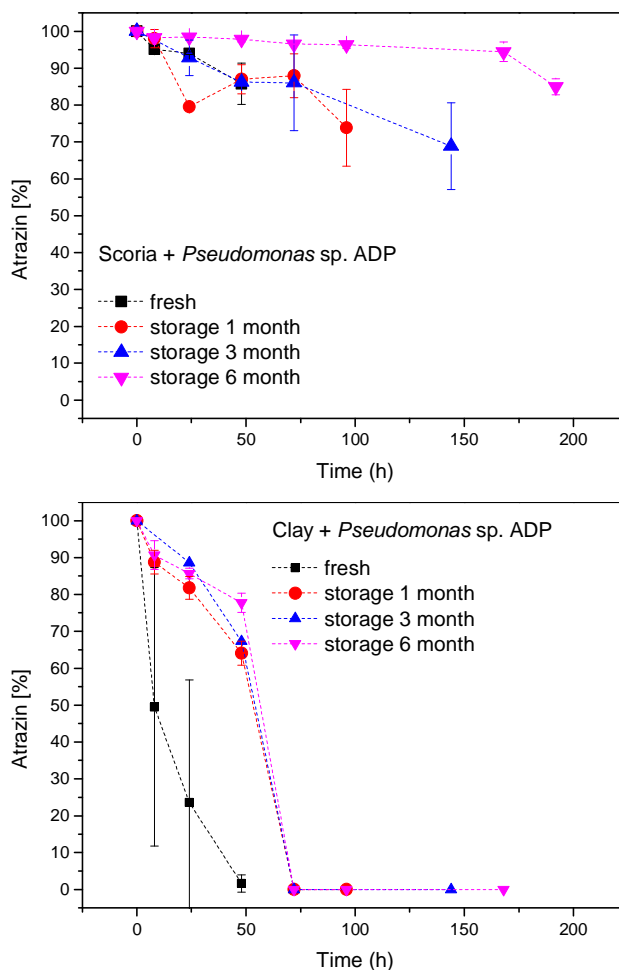


Fig. 1: Atrazine removal by *P. ADP* immobilized within thin silica layers onto scoria and clay. Degradation capacity was monitored directly after immobilization as well as after 1 to 6 months of storage at 4 °C.

immobilized in clay, atrazine was always fully degraded within 72 h even after 6 month of storage. With cells immobilized in scoria, only 30% atrazine degradation was reached within the tested time frame. In contrast to previous experiments [1], this poor scoria activity was already observed immediately after the immobilization procedure which makes a comparison of the results for both materials quite difficult. Nevertheless, these results provide a promising basis for the application of sol-gel immobilized bacteria on porous carrier materials for the removal of atrazine from contaminated water even after long-term storage of the biohybrid material before first usage. Hence, both biohybrid materials should be further considered for immobilization of microorganisms with preservation of viability and metabolic activity.

ACKNOWLEDGEMENTS. The authors thank the BMBF-MOST German-Israeli Water Technology Research Fund (WT1103/02WA1223).

[1] Pannier, A. et al. (2014) *RSC Adv.* 4, 19970–19979.

SCIENTIFIC CONTRIBUTIONS (PART II)

**LONG-LIVED RADIONUCLIDES IN
GEOLOGICAL SYSTEMS**

A macroscopic and spectroscopic investigation of neptunium(V) adsorption on montmorillonite and corundum

O. Elo,¹ N. Huittinen, K. Müller, A. Ikeda-Ohno, A. C. Scheinost, P. Hölttä,¹ J. Lehto¹

¹Laboratory of Radiochemistry, University of Helsinki, Helsinki, Finland

This work studied the adsorption of neptunium(V) on montmorillonite and corundum. The macroscopic sorption behavior was investigated in batch sorption experiments as a function of both pH and neptunium concentration. The speciation of the actinide on the solid surfaces was investigated by *in situ* ATR-FT IR and EXAFS spectroscopic experiments. Np(V) adsorbs on both mineral surfaces as an inner-sphere complex, presumably in a bidentate fashion.

EXPERIMENTAL. The Na-montmorillonite used in this work has been extracted and purified from MX-80 Volclay bentonite. α -Al₂O₃ powder (corundum) was obtained from Taimicron Chemicals, Tokyo, Japan (TAIMICRON TM-DAR). All experiments were performed under carbonate-free N₂-atmosphere in 10 mM NaClO₄ (batch sorption experiments) or NaCl (spectroscopic investigations). The Np(V) concentration was varied between 5×10^{-10} M and 5×10^{-6} M in the batch sorption investigations, while a higher concentration of 20 μ M was required for the spectroscopic experiments. The solid concentration used in the batch sorption experiments was either 0.5 g/L (simulating the low solid/liquid ratio in our *in situ* ATR FT-IR investigations) or 5 g/L (used in the EXAFS experiments).

RESULTS. The uptake of 10^{-6} M Np(V) on montmorillonite and corundum as a function of pH is presented in Fig. 1. At pH 8, i.e. the pH-value expected to prevail in the final disposal site for the Finnish SNF in Olkiluoto, Finland, corundum shows a very low uptake of the pentavalent actinide. A higher sorption percentage is obtained for montmorillonite, but only for the higher solid concentration of 5 g/L. Montmorillonite also shows a small but constant uptake of neptunium in the acidic to neutral pH range that could speak for cation exchange on the permanently charged planar sites.

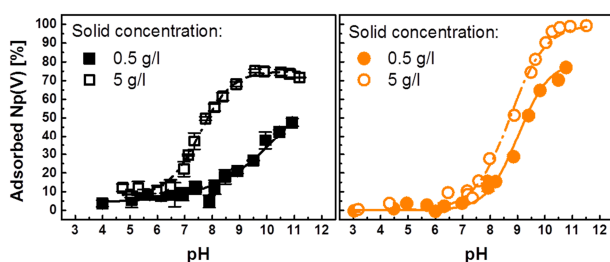


Fig. 1: Sorption of 10^{-6} M Np(V) on montmorillonite (left) and corundum (right) as a function of pH.

To further investigate the surface speciation of Np(V) on the solids, we performed *in situ* ATR-FT IR investigations in 10 mM NaCl at pD 9.6 (pH = 10). Upon Np(V) sorption onto corundum and montmorillonite we observe a shift of the antisymmetric NpO₂ stretching vibration from 818 cm⁻¹, obtained for the free aquo ion, to 790 cm⁻¹, indicating a formation of an inner-sphere bound neptunium complex on the mineral surfaces (Fig. 2, black traces).

This complex is easily removed from the solid surfaces when the mineral film on the ATR crystal is flushed with

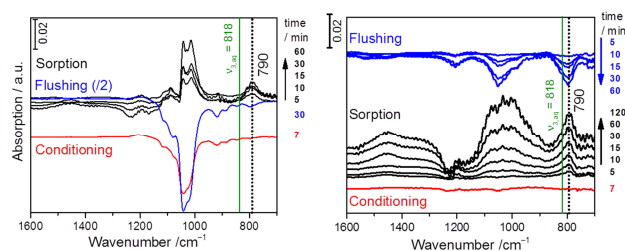


Fig. 2: Sorption of 20 μ M Np(V) on montmorillonite (left) and corundum (right) in 10 mM NaCl at pD 9.6, flow rate 0.1 mL/min.

the background electrolyte (Fig. 2, blue traces). A similar desorption behavior is obtained in batch desorption experiments upon exchange of the electrolyte only (data not shown). To examine the reason for the fast desorption kinetics observed in the IR experiments we performed Np L_{III}-edge EXAFS investigations on corundum samples at pH 9 and 10. The k^3 -weighted Np L_{III}-edge EXAFS spectra for both corundum samples and their corresponding Fourier transforms (FTs) are presented in Fig. 3.

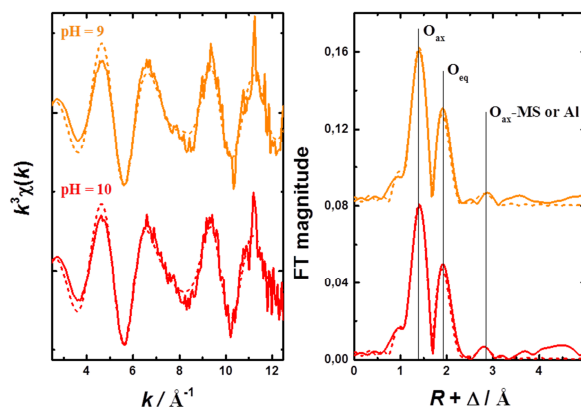


Fig. 3: k^3 -weighted Np L_{III}-edge EXAFS spectra for Np adsorbed on corundum (left) and their corresponding Fourier transforms (right). Solid lines; experimental data, dotted lines; theoretical fitting. Phase shifts (Δ) are not corrected on the FTs.

In contrast to a weakly bound monodentate surface complex that could have explained the fast neptunium desorption behavior in the studied system, our EXAFS structural parameters obtained from theoretical curve fitting indicate the formation of a bidentate inner-sphere complex with an average Np-O equatorial oxygen distance of 2.45 Å and a Np-Al distance of 3.36 Å. Thus, no apparent conclusion for the fast desorption behavior can be drawn from these results.

ACKNOWLEDGEMENTS. The authors would like to thank the ROBL staff at BM20 for help and support during the EXAFS measurements. Karsten Heim is thanked for his help with the ATR-FT IR investigations.

Complementary spectroscopic investigation of Np(V) sorption on birnessite

K. Müller, B. Simon,¹ A. Rossberg

¹National Graduate School of Chemistry, Paris, France

The Np(V) sorption onto birnessite has been studied in-situ by application of ATR FT-IR and EXAFS spectroscopy. The formation of a single bidentate inner-sphere complex has been derived.

Manganese oxides play a decisive role in regulating the mobility of contaminants even at tracer concentrations due to their high sorption and redox capacity and scavenging capability [1]. In this work, Np(V) sorption on amorphous birnessite (Bs) is investigated at micromolar Np concentrations using ATR FT-IR and EXAFS spectroscopy on a molecular level.

EXPERIMENTAL. Bs was synthesized and characterized as described in [2]. The N₂-BET specific surface area was found to be 219 m² g⁻¹. The isoelectric point determined by zeta potential is at pH 2.5. For infrared sorption experiments, Np(V) concentration was set to 50 μM at an ionic strength of 0.1 M adjusted by NaCl at pH 8. All measurements were performed with D₂O (Sigma Aldrich, isotope purity > 99%). The ATR FT-IR accessory and the procedure for the in-situ sorption measurement were described in detail previously [3]. EXAFS was applied to one batch sorption sample (10 μM Np, 0.1 M NaCl, pH 8.0, 0.6 g L⁻¹ Bs). Experimental details are given in [4].

RESULTS. The IR spectra obtained are shown in Fig. 1. The absence of significant negative bands in the spectrum of the conditioning stage confirms the stability of the stationary Bs film on the ATR crystal [3]. Upon Np(V) sorption, one distinct band at 789 cm⁻¹ increases with time and is assigned to the antisymmetric stretching vibrational mode (ν₃) of the sorbed neptunyl ion. The IR spectrum obtained from an aqueous solution at 50 μM Np(V), 0.1 M, pH 6 shows the absorption of ν₃(Np^VO₂) at 818 cm⁻¹. The red shift of ν₃ to 789 cm⁻¹ can be assigned to an inner-sphere monomeric sorption complex, as previously reported for hematite and other mineral oxides [3]. In the flushing stage, a less intense negative band at equal frequency is observed indicating that parts of the bound Np(V) are released from the stationary Bs phase. The very small band at 1025 cm⁻¹ is due to rear-

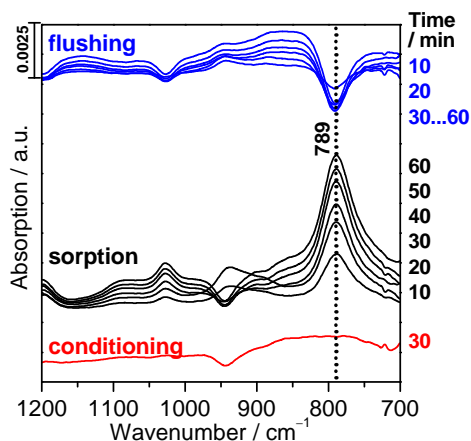


Fig. 1: ATR FT-IR spectra of 50 μM Np(V) sorbed onto Fh at pH 8, 0.1 M NaCl, D₂O, N₂. Spectra are equally scaled. Indicated values are in cm⁻¹.

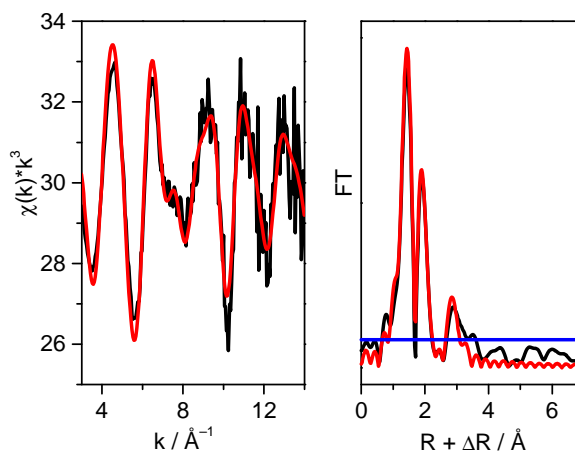


Fig. 2: NpL_{III}-edge k³-weighted EXAFS spectra from batch sorption sample (black, left) and corresponding Fourier- transform (FT) (black, right). Shell fits (red), estimated level of experimental error (blue horizontal line) (10 μM Np, 0.1 M NaCl, pH 8.0, 0.6 g L⁻¹ Bs).

Tab. 1: EXAFS structural parameters (^a coordination number, ^b atomic distance, ^c Debye-Waller factor).

Shell	CN ^a	R / Å ^b	σ ² ·10 ³ / Å ² ^c
Np=O _{ax}	2	1.87	2.2
Np-O _{eq}	5	2.46	8.3
Np-Mn	1.4	3.41	6

angement processes at the mineral oxide surface upon sorption and is similarly observed for interactions on amorphous iron oxides [3].

To obtain further structural information, Np L_{III}-edge EXAFS investigations were performed. The experimental spectrum (black) and the fitted structural parameters are shown in Fig. 2 and the fitted structural parameters are summarized in Tab. 1. Three FT peaks show magnitudes that are significant higher than the level of the experimental error (blue line): the scattering contributions of the two axial oxygen atoms of NpO₂⁺ (O_{ax}) at 1.87 Å, the oxygen atoms in the equatorial plane (O_{eq}) at 2.46 Å and a third scattering contribution at 3.41 Å. The origin of the latter peak is likely due to the scattering contribution of Mn atoms stemming from binary edge-sharing sorption complexes.

In summary, IR and EXAFS spectra evidence the formation of a single Np surface species, most probably a mononuclear bidentate edge-sharing complex.

ACKNOWLEDGEMENTS. The authors are grateful to C. Eckardt, S. Weiss, K. Heim, A. Scholz and E. Christalle and the ROBL staff at ESRF for support during the EXAFS measurements. The funding of this work by Deutsche Forschungsgemeinschaft (MU 3207/1-1) is greatly acknowledged.

- [1] Post, J. E. (1999) *Proc. Natl. Acad. Sci. U. S. A.* **96**, 3447–3454.
- [2] Händel, M. et al. (2013) *Geoderma* **193**, 117–121.
- [3] Müller, K. et al. (2009) *Environ. Sci. Technol.* **43**, 7665–7670.
- [4] Gückel, K. et al. (2013) *Environ. Sci. Technol.* **47**, 14418–14425.

Np(V) retention by magnetite

R. Steudtner, A. C. Scheinost

Anoxic corrosion of the technical barriers in nuclear waste repositories causes formation of secondary minerals like iron oxides and sulphides, which may retain radionuclides by sorption or structural incorporation (solid-solution formation). In this context, we investigated the interaction of Np(V) in the presence of a highly redox-reactive mineral, magnetite $\text{Fe}^{\text{II}}(\text{Fe}^{\text{III}})_2\text{O}_4$.

EXPERIMENTAL. The mineral magnetite was synthesized as described in [1]. Sorption experiments were conducted with an initial Np(V) concentration of $2 \times 10^{-5} \text{ mol}\cdot\text{L}^{-1}$ in solutions with an ionic strength of 0.1 M. The retention of Np was studied as function of the pH, the solid-to-liquid ratio and the reaction time, respectively. Mineral synthesis and sorption experiments were performed under strictly anoxic conditions in a glove box at $< 2 \text{ ppm O}_2$. The distribution coefficient (R_d in $\text{mL}\cdot\text{g}^{-1}$) was determined from the remaining Np concentration in the supernatant measured by liquid scintillation counting. ATR FT-IR and EXAFS measurements were applied for identification and structural characterization of the formed Np species in presence of the minerals.

RESULTS. The Np(V) retention in presence of magnetite is depending on the pH and reaction time (Fig. 1). The $\log R_d$ generally increases to a maximum at pH 12 with increasing the pH value. At pH 2 and 4 the $\log R_d$ values are independent from the reaction time, at higher pH the $\log R_d$ value increases with increasing reaction time.

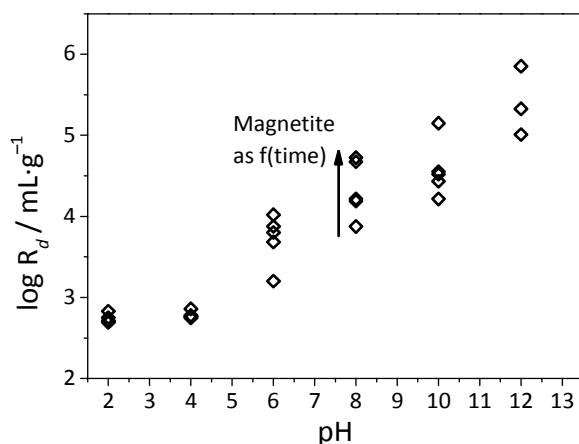


Fig. 1: Sorption edges of Np(V) onto magnetite. $s/l = 1 \text{ g}\cdot\text{L}^{-1}$, $I = 0.1 \text{ M}$, $[\text{Np(V)}]_{\text{initial}} = 2 \times 10^{-5} \text{ M}$, after 1 h, 1 d, 1 and 4 weeks, N_2 .

The *in situ* ATR-FTIR spectrum of Np(V) reacted magnetite under inert gas shows in the antisymmetric stretching vibration of the NpO_2^+ ion, ν_3 , demonstrating sorption of Np(V) to the magnetite surface (Fig. 2). In comparison to ν_3 of the aquo ion at 818 cm^{-1} , that of the sorption complex is shifted by 30 cm^{-1} to lower wavenumbers, suggesting formation of an inner-sphere sorption complex of Np(V) [2]. A similar frequency of this vibrational mode was observed for NpO_2^+ sorption complexes on other iron(III) minerals.

XAFS analysis, in contrast, showed a complete reduction of Np(V) to Np(IV) already after the shortest reaction times of 1 h. This contradiction is resolved by assuming a rapid sorption of Np(V) observed by ATR-FTIR (note

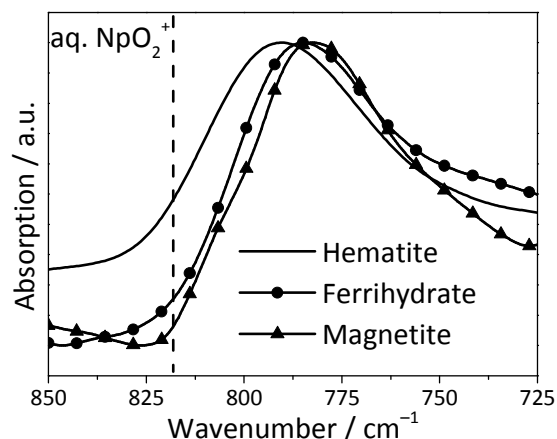


Fig. 2: IR spectra of *in situ* Np(V) sorption experiments on magnetite in comparison with other iron(III) minerals after 120 min. $[\text{Np(V)}]_{\text{initial}} = 2 \times 10^{-5} \text{ M}$, 0.1 M NaCl, D_2O , N_2 , pH 8.

that Np(IV) is silent in this spectral region), followed by a reduction to Np(IV) observed by XAFS. The local structure of this Np(IV) sorption complex consists of 6 oxygen atoms at a distance of 2.43 \AA and of 3 iron atoms at a distance of 3.45 \AA , revealing formation of a tridentate Np(IV) sorption complex, which dominates at pH 6 and at the short reaction times. With increasing pH and sorption time a Np-Np shell becomes visible, with a distance of 3.83 \AA and a coordination number of 3.5, indicative of formation of NpO_2 nanoparticles or of poorly ordered NpO_2 precipitates.

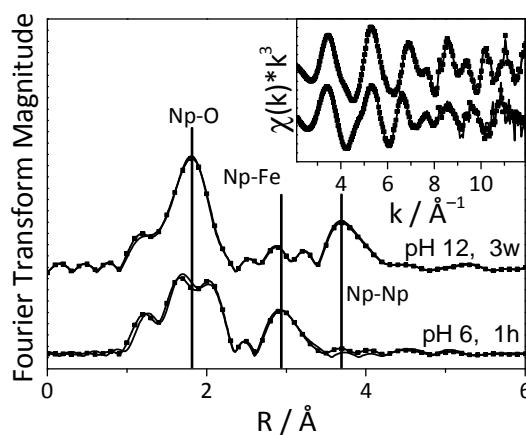


Fig. 3: Fourier transform magnitude spectra of magnetite-reacted Np as function. $s/l = 1 \text{ g}\cdot\text{L}^{-1}$, $I = 0.1 \text{ M}$, $[\text{Np(V)}]_{\text{initial}} = 2 \times 10^{-5} \text{ M}$, N_2 .

ACKNOWLEDGEMENT. This work is part of the IMMORAD project, funded by BMWi through contract 02NUK019D.

- [1] Kirsch, R. et al. (2011) *Environ. Sci. Technol.* **45**, 7267–7274.
 [2] Müller, K. et al. (2009) *Environ. Sci. Technol.* **43**, 7665–7670.

Np(V)-ferrihydrite sorption complexes at high pH: An EXAFS Monte Carlo approach

A. Rossberg, K. Müller

We used EXAFS Monte Carlo simulation (MC) to determine the structure of two Np(V)-ferrihydrite (Fh) sorption complexes prepared under inert gas atmosphere at high pH.

MC and EXAFS [1] can be used to solve the molecular structure of surface complexes, even if this method may become complicated in the case of higher-order scattering. MC requires the structure of the interacting ligand or surface besides the experimental data and FEFF calculated theoretical phase and amplitude functions.

EXPERIMENTAL. Two batch sorption samples were prepared with the same solid(Fh)-solution ratio: sample a) 0.12 g Fh in 200 mL water, 0.95 mg Np(V), pH = 9.4, freshly prepared, specific surface area (BET): 209 m²/g; sample b): 0.30 g Fh in 500 mL water, 1.19 mg Np(V), pH = 10.8, aged for 3 months at pH 5.5 in suspension at 25 °C and N₂, BET: 162 m²/g. The resulting Np(V) surface loadings were 7.9 mg/g (0.038 mg/m²) and 3.9 mg/g (0.024 mg/m²). For each sample eight Np L_{III} edge spectra were measured at ROBL in fluorescence mode at low temperature (15 K) and then averaged.

RESULTS. The MC consists of two steps: 1. Determination of the most probable location of the Np atom at the substrate. 2. Refinement of the local structure of the surface complex to gain the radial pair distribution function (PDF) for measuring bond distances and Debye-Waller factors (DW). For both samples, a simple shell fit of the axial O_{ax} and equatorial O_{eq} shell was performed to determine the threshold energy ΔE_0 , which is needed for the MC. In the case of sample a), during the first step of MC the fitted signal of the O_{ax} shell and the half signal of the O_{eq} shell were taken as a constant scattering contribution, while guessed DW with a radial dependency were used for the substrate atoms. The crystallographic unit cell of Fh was taken to simulate the substrate [2]. After probing randomly about four million Np-positions at the unit cell, four structurally equivalent Np-locations were found which are in agreement with a double corner sharing (DC₁) sorption complex (Fig. 1a). The second step yields the refined structure of the DC₁ complex (Fig. 1b) and the PDF (Fig. 2c). In the case of sample b), the Fe signal is twice in intensity when compared with sample a) (FT peak at 3.5 Å in Fig. 2b), yielding a four-fold degeneracy for the Np-Fe path, with the Np-Fe distance of 4.02 Å being identical to the one found for sample a). The only meaningful interpretation of this Np-Fe path is the formation of a DC₂ complex (Fig. 1c), hence, the first MC step would imply the probing of Np-positions at two different surfaces at the same time, which is not possible. Accordingly, for sample b) only the second MC step was performed. The starting structure of the DC₂ complex was constructed by using bond distances supplied by the shell fit. The refined structure and the resulting PDF is shown in Fig. 1c and Fig. 2c, respectively. For both samples, the EXAFS spectrum and the MC-Fit is shown in Fig. 2a. In the case of sample a) the short O_{ax}-O_{Fe} distance of 2.79 Å–2.81 Å is typical for two oxygen atoms connected via a hydrogen bond (Fig. 1b) [3,4]. The Np-O_{ax} distance of 1.86 Å (Fig. 1b) is significantly higher than in the case

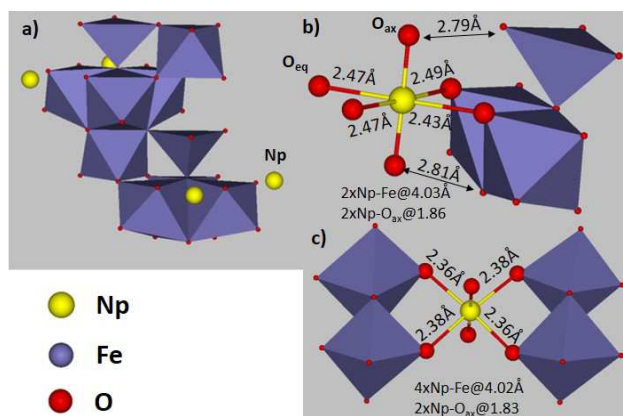


Fig. 1: (a) Most probable positions of Np(V) at the surface (Fh unit cell), (b) refined structure of the DC₁ complex (sample a), (c) refined structure of the DC₂ complex (sample b).

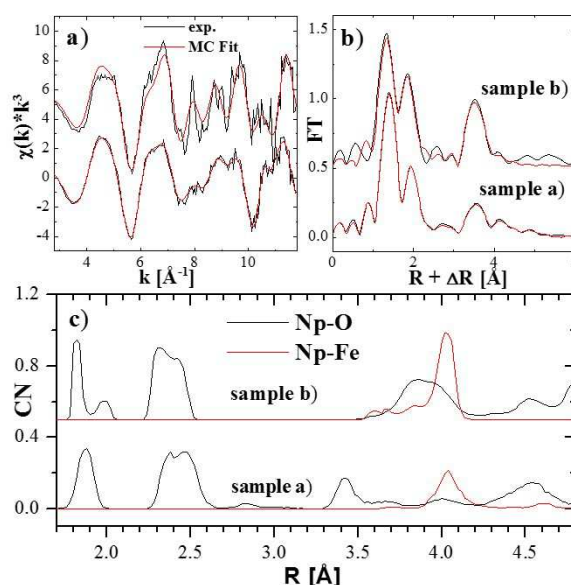


Fig. 2: (a) EXAFS spectra with MC Fit, (b) corresponding Fourier transforms (FT), (c) Np-O and Np-Fe PDF.

of Np(V)-hydrate (Np-O_{ax} 1.83 Å [5]). Such strong increase would be in line with an O_{ax}-hydrogen interaction [6]. Further investigations will be accomplished in order to understand the dependency between the formed complex structures and the experimental parameter, like the influence of the different number of available surface sites and/or the influence of the aging time.

- [1] Rossberg, A. and Scheinost A. C. (2005) *Anal. Bioanal. Chem.* **383**, 56–66.
- [2] Michel, F. M. et al. (2007) *Science* **316**, 1726–1729.
- [3] Krot, N. N. et al. (2010) *Radiochem.* **52**, 12–16.
- [4] Roques, J. et al. (2009) *Int. J. Mol. Sci.* **10**, 2633–2661.
- [5] Ikeda-Ohno, A. et al. (2008) *Inorg. Chem.* **47**, 8294–8305.
- [6] Lucks, C. et al. (2013) *Dalton Trans.* **42**, 13584–13589.

U(VI) surface complexation on montmorillonite at high ionic strengths

K. Fritsch, K. Schmeide

Surface complexation constants for U(VI) sorption on montmorillonite were determined with sorption data acquired at ionic strengths of 1 to 3 mol kg⁻¹.

The generation of thermodynamic data is necessary to be able to describe and predict radionuclide retention by minerals and rock. Surface complexation modeling yields thermodynamic constants for the formation of sorption complexes on mineral surfaces. So far, studies have mostly focused on low ionic strength media.

EXPERIMENTAL. After purification according to Poinsot and Bradbury and Baeyens [1, 2], montmorillonite was used as substrate. Cation exchange capacity was determined to have a value of 85 mmol_c (100 g)⁻¹. The following conditions were used for the batch sorption experiment: S/L = 4.00 ± 0.01 g L⁻¹, c_{NaCl} = 1...3 mol kg⁻¹, pH = 4...10, room temperature, absence and presence of CO₂ (p_{CO2} = 10^{-3.5} atm), c_{U(VI)} = 1 × 10⁻⁶ mol kg⁻¹, sorption time 5 to 7 days.

RESULTS. Surface complexation constants were determined according to the two site protolysis non-electrostatic surface complexation and cation exchange model (2SPNE SC/CE) [3]. For aqueous geochemistry modeling, PHREEQC v3.1.2 was used [4]. For parameter estimation, PEST v13.0 was employed [5]. THEREDA release 9 [6] was used as thermodynamic database; surface site density and protolysis constants for the surface sites were taken from [3]. Due to the high ionic strengths, the Pitzer ion interaction approach was used [7].

U(VI) sorption on montmorillonite in absence of CO₂ (c.f. Fig. 1a) can be described by cation exchange and several uranyl hydroxide complexes. Bradbury and Baeyens [2] used four hydroxide complexes – ≡S^SOUO₂⁺, ≡S^SOUO₂OH, ≡S^SOUO₂(OH)₂⁻ and ≡S^SOUO₂(OH)₃²⁻ – on the strong surface sites as well as two uranyl hydroxide complexes on weak binding sites. The ≡S^SOUO₂(OH)₂⁻ complex was not included in the present model, because the modeling calculation proved to be more stable without it. Furthermore, no surface complexes of U(VI) on weak surface sites were used, as the respective complexation constants had error margins several times the size of the value itself and were therefore deemed unreliable.

In presence of CO₂ (c.f. Fig. 1b), Marques Fernandez et al. [8] proposed to use two complexes on strong surface sites, ≡S^SOUO₂(CO₃)⁻ and ≡S^SOUO₂(CO₃)₂³⁻. However, in this work, only the ≡S^SOUO₂(CO₃)₂³⁻ complex was used to prevent overestimation of the system. Spectroscopic investigations to confirm this choice of uranyl hydroxide and carbonate surface complexes are currently performed.

Tab. 1: Surface complexation constants for U(VI) sorption to purified montmorillonite at high ionic strengths (1 to 3 mol kg⁻¹).

	Surface complex	log k
CEC	Cation exchange	0.50 ± 0.05
k1	≡S ^S OUO ₂ ⁺	1.70 ± 0.15
k2	≡S ^S OUO ₂ OH	-3.69 ± 0.03
k3	≡S ^S OUO ₂ (OH) ₃ ²⁻	-19.7 ± 0.1
k4	≡S ^S OUO ₂ (CO ₃) ₂ ³⁻	18.3 ± 0.2

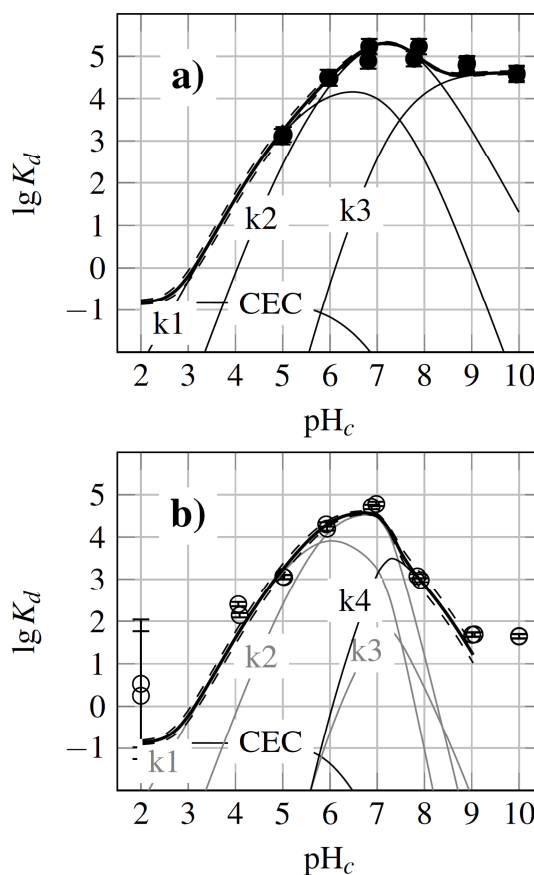


Fig. 1: U(VI) sorption on montmorillonite at 3 mol kg⁻¹ NaCl, in absence (Fig. 1a) and presence (Fig. 1b) of CO₂.

ACKNOWLEDGEMENT. This work was funded by the BMWi (No. 02 E 10971).

- [1] Poinsot, C. et al. (1999) *Nagra Technical Report 99-04*.
- [2] Bradbury, M., Baeyens, B. (2009) *Geochim. Cosmochim. Acta* **73**, 990–1003.
- [3] Bradbury, M., Baeyens, B. (1997) *J. Contam. Hydrol.* **27**, 223–248.
- [4] Parkhurst, D. L., Appelo, C. A. J. (2013) *Description of input and examples for PHREEQC version 3—A computer program for speciation, batch-reaction, one-dimensional transport, and inverse geochemical calculations*, USGS Techniques and Methods, book 6, ch. A43, 497.
- [5] Doherty, J. E., Hunt, R. J. (2010) *Approaches to highly parameterized inversion—A guide to using PEST for groundwater-model calibration*, USGS Scientific Investigations Report 2010–5169, 59.
- [6] Thermodynamic Reference Database (www.thereda.de), Data Release No. 9 (2014).
- [7] Pitzer, K. S. (1991) *Activity Coefficients in Electrolyte Solutions*, CRC Press, Boca Raton, Florida.
- [8] Marques Fernandes, M. et al. (2012) *Geochim. Cosmochim. Acta* **93**, 262–277.

The sorption behavior of U(VI) onto orthoclase and muscovite – Impact of U(VI) concentration and calcium ions

C. Richter, V. Brendler, K. Großmann

Long term safety analysis requires thermodynamic data based on sorption experiments. As for feldspars and mica only a few data is available [1–5], sorption experiments with U(VI) and orthoclase as a representative for feldspars and muscovite as mica were performed. The results showed that parameters like the concentration of U(VI) and the presence of Ca as a competitive sorbing ion have a significant influence on the sorption behavior.

EXPERIMENTAL. U(VI) batch sorption experiments onto orthoclase and muscovite were performed, varying the following parameters: concentration of U(VI) (10^{-5} and 10^{-6} M), solid-to-liquid ratio (1/20 and 1/80 g/mL), pH values (5 to 8), ionic strength (0.01 and 1 M). The concentration of Ca as a competing cation was set to 1.5×10^{-3} M. All experiments were performed in triplicate, under ambient air, at room temperature, and with a sample volume of 10 mL. Prior to the incubation of U(VI), the pH of each sample was adjusted until it was stable. After one week of sorption, the samples were centrifuged and the supernatant was analyzed with ICP-MS (ELAN 9000 from Perkin Elmer).

RESULTS. From the experiments of both minerals the highest sorption capacity is found in the circumneutral pH range (solid-to-liquid ratio of 1/80) which decreases at more acidic and basic pH values. In general, orthoclase shows a lower sorption capacity than muscovite. An increased solid-to-liquid ratio (1/20) results in an increased amount of U(VI) sorbed onto the surfaces which is due to a higher amount of potential binding sites.

The influence of the concentration of U(VI) on the sorption is exemplarily shown for orthoclase in Fig. 1. At a higher concentration of U(VI) less sorption is observed because of increased competition for the available surface binding sites. Experiments at a higher ionic strength show a small shift of the sorption curve to lower pH values indicating the predominance of outer-sphere complexation (data not shown).

In the presence of Ca, the sorption is decreased in the pH range above 8 (Fig. 2) which is mainly due to the presence of the $\text{Ca}_2(\text{UO}_2(\text{CO}_3)_3)$ (aq) complex in solution as

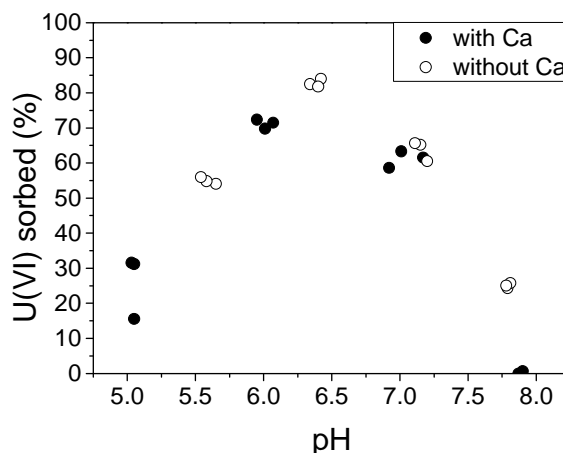


Fig. 2: Sorption of 10^{-5} M U(VI) onto orthoclase in presence and absence of 1.5×10^{-3} M Ca at a solid-to-liquid ratio of 1/20 and in 0.01 M NaClO_4 .

described in [6]. This neutral complex shows only a low affinity to the mineral surfaces. At lower pH values, this complex does not occur in solution and, thus, the sorption behavior of U(VI) is not impacted. In addition, a high affinity of Ca^{2+} ions to the surfaces might reduce the number of potential binding sites for U(VI).

The comprehensive evaluation of the impact of these parameters on the U(VI) sorption processes onto orthoclase and muscovite is in progress and will significantly contribute to future long term safety analysis. This comprises the derivation of thermodynamic surface complexation parameters.

- [1] Ames, L. L. et al. (1983) *Clays .Clay Min.* **31**, 343–351.
- [2] Arnold, T. et al. (2006) *Environ. Sci. Technol.* **40**, 4646–4652.
- [3] Arnold, T. et al. (2001) *J. Contam. Hydrol.* **47**, 219–231.
- [4] Moyes, L. N. et al. (2000) *Environ. Sci. Technol.* **34**, 1062–1068.
- [5] Nebelung, C. et al. (2010) *Radiochim. Acta* **98**, 621–625.
- [6] Bernhard, G. et al. (2001) *Radiochim. Acta* **89**, 511–518.

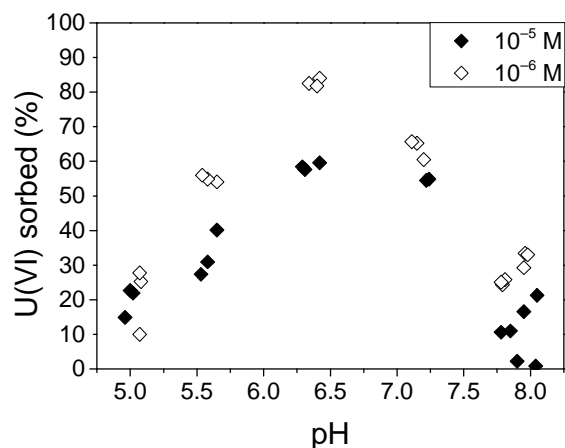


Fig. 1: Sorption of 10^{-5} M and 10^{-6} M U(VI) onto orthoclase at a solid-to-liquid ratio of 1/20 in 0.01 M NaClO_4 .

Uranium(VI) sorption onto gibbsite: Increasing confidence in surface complexation models by combining spectroscopy and batch sorption experiments

F. Bok, K. Gückel¹

¹Helmholtz Zentrum München Deutsches Forschungszentrum für Gesundheit und Umwelt (GmbH), Institut für Strahlenschutz, Neuherberg, Germany

Surface complexation data have been created for various combinations of ligands sorbing on mineral surfaces. In contrast to thermodynamic data, for the speciation in aqueous solution there is no unified and consistent data collection for surface complexation so far. This work describes the benefit of combining spectroscopic and batch sorption experimental data to create a reliable and consistent surface complexation data set.

Surface complexation models differ in their way to represent the electric double layer and the surface protolysis steps. Moreover, aqueous and surface speciation and thermodynamic data thereof affect the outcome of such models, rendering modeling results hardly comparable. For uranium(VI) sorption onto gibbsite, e.g., various surface complexes and their formation constants are published [1–4]. The proposed uranium-gibbsite surface complexes vary from simple 1:1 complexes ($\equiv\text{Al}-\text{O}-\text{UO}_2^+$, [1–3]) up to highly hydrolyzed, trimeric surface complexes ($\equiv\text{Al}-\text{O}-(\text{UO}_2)_3(\text{OH})_5$, [1, 2, 4]) and combinations thereof. Depending on the specific species set, the published reaction constants ($\log_{10}K$) differ for identical complexes up to 16 orders of magnitude.

In contrast to the published surface speciation [1–4], results of spectroscopic investigations (EXAFS, ATR FT-IR) indicate only a monomeric, bidentate surface complex with the generic formula ($\equiv\text{Al}-\text{O})_2\text{UO}_2(\text{OH})_x(\text{H}_2\text{O})_{3-x}^{x-}$, $x = 0-3$) in the absence of carbonate [5].

CALCULATIONS. No batch sorption experiments have been done in [5] to obtain a $\log_{10}K$ value for the formation reaction of the bidentate complex. Thus, three data sets of 48 batch sorption experiments have been re-digitized from [4, pp. 143–144] to fit the $\log_{10}K$ value. The number of hydroxyl groups in this surface complex is not detectable with spectroscopic methods, so $\log_{10}K$ value fits were done for all possible degrees of hydrolysis ($x = 0-3$) and a simultaneous fit of the two with the best single fit's mean residuals ($x = 0$ & 1). To do so, the speciation code PHREEQC [6] was coupled with the parameter estimation software UCODE2005 [7], using the aqueous speciation based on the OECD/ NEA TDB [8].

RESULTS. The $\log_{10}K$ values for each hydrolyzed version of the surface complex and their mean residuals of the calculated sorption data from the experimental results are given in Table 1. The best fit was obtained using a degree of hydrolysis of $x = 0$ or 1, the respective mean re-

Tab. 1: Fitted $\log_{10}K$ values and mean residuals for surface complex differing in their degree of hydrolysis (x).

x	$\text{Log}_{10}K$	Mean residuals
0	-6.029	7.10%
1	-13.87	7.33%
2	-21.66	9.70%
3	-29.41	12.56%
0 & 1	-7.051 & -13.79	6.99%

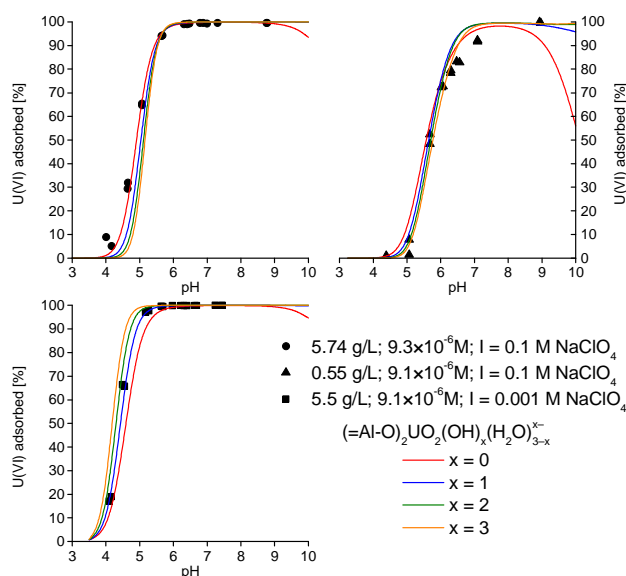


Fig. 1: Fitted $\log_{10}K$ values results the surface complex depending on the degree of hydrolysis (x).

siduals are nearly identical (Tab. 1). Calculating the surface speciation with the simultaneously fitted $\log_{10}K$ values for the degrees of hydrolysis $x = 0$ and 1 even gave a slightly better agreement with the experimental results but the complex with $x = 0$ is a minor species with less than 10%.

CONCLUSIONS. The sorption of U(VI) onto gibbsite can be modelled using only one surface complex, which is ($\equiv\text{Al}-\text{O})_2\text{UO}_2(\text{OH})(\text{H}_2\text{O})_2^-$). Although only a single surface complex is used, the modeling results match better to the experimental values than the results of calculations based on previously published surface complexation parameters [1–4].

Batch sorption experiments of U(VI) onto gibbsite in the presence of carbonate are necessary to obtain a $\log_{10}K$ value for the trimeric bidentate surface complex ($\equiv\text{Al}-\text{O})_2(\text{UO}_2)_2\text{CO}_3(\text{OH})_x(\text{H}_2\text{O})_{3-x}^{x-}$, $x = 0-3$) also detected in [5]. This would lead to a consistent and complete surface complex data set to describe the sorption of U(VI) onto gibbsite.

- [1] Zachara, J.M. et al. (1993) *Aquat. Sci.* **55**, 250–261.
- [2] McKinley, J.P. et al. (1995) *Clays Clay Miner.* **5**, 586–598.
- [3] Del Nero, M. et al. (1998) *OKLO Working Group, Report No. EUR 18314 EN*, 277–290.
- [4] Karamalidis, A.K., Dzombak, D.A. (2010) *Surface complexation modeling: Gibbsite*. John Wiley & Sons, Hoboken.
- [5] Gückel, K. (2013) *Structural analysis of ternary actinyl(V/VI) sorption complexes on gibbsite – A combined quantum chemical and spectroscopic approach*, Ph.D. thesis, Technische Universität Dresden.
- [6] Parkhurst, D. L. et al. (2013) *U.S. Geological Survey Techniques and Methods, Vol. book 6-A43*, 497 p.
- [7] Poeter, E. P. et al. (2005) *U.S. Geological Survey Techniques and Methods, Vol. book 6-A11*, 283 p.
- [8] Guillaumont, R. et al. (2003) *Update on the chemical thermodynamics of U, Np, Pu, Am and Tc*. Elsevier, Amsterdam.

Effects of the background electrolyte on Th(IV) sorption behavior

M. Schmidt, S. Hellebrandt, K. E. Knope,¹ S. S. Lee,¹ R. E. Wilson,¹ J. E. Stubbs,² P. J. Eng,² L. Soderholm,¹ P. Fenter¹

¹Argonne National Laboratory, Argonne, IL, U.S.A.; ²University of Chicago, Chicago, IL, U.S.A.

The adsorption of Th(IV) on the muscovite (001) basal plane was studied by Resonant Anomalous X-ray Reflectivity (RAXR), Crystal Truncation Rods (CTR) and α -spectrometry in the presence of LiClO₄ and NaClO₄ ([Th(IV)] = 0.1 mM, I = 0.1 M, pH = 3.3 ± 0.3). RAXR data show strong influence of the background electrolyte on the sorption behavior of the actinide. We find no significant Th adsorption in 0.1 M NaClO₄. These results are in clear contrast to the behavior of Th in 0.1 M NaCl which showed a coverage of 0.4 Th/A_{UC} (area of the unit cell, A_{UC} = 46.7 Å²)[1]. In contrast, strong adsorption is found with 0.1 M LiClO₄ media (θ (Th) = 4.9 Th/A_{UC}). These findings are confirmed independently by α -spectrometry, where no measurable coverage of Th is observed from 0.1 M NaClO₄ background, and a large coverage of 1.6 Th/A_{UC} for 0.1 M LiClO₄, can be detected. CTR/RAXR analyses of the Th distribution from 0.1 M LiClO₄ suggests that this behavior is due to the formation of Th nanoparticles.

We explore differences in the sorption behavior of Th(IV) from NaCl [1] and LiClO₄, and NaClO₄ media. Sorption was studied on the molecular level by surface X-ray diffraction and was independently quantified by α -spectrometry. For geochemical studies perchlorate salts, particularly sodium perchlorate NaClO₄, are frequently chosen, due to the perchlorate ion's very weak coordination strength with nearly all cations. However, recent results highlight that even minor changes in the background electrolyte composition can drastically alter the reactivity of a mineral surface [2].

RESULTS. Solutions were prepared from ²³²Th stock solutions by appropriate dilution with the respective background electrolyte. Slight variations in pH values aside, the background electrolyte cation (Li⁺/Na⁺) is the only difference between the samples.

Yet, the sorption behavior is vastly different. In the case of LiClO₄, strong RAXR modulations are observed which can be fit with the structural model presented in Fig. 1. The structure consists of two peaks at ~4.1 Å and ~29 Å, respectively, indicating the coexistence of two Th sorption modes. The model is associated with a fairly small uncertainty and reproduces the data ($\chi^2 = 5.0$, R = 4.1%). The first peak is closer to the surface than the extended outer sphere complex observed for Th-NaCl [1]. It covers the range of adsorption heights typically occupied by sorption complexes of hydrated and partly hydrated cations [3]. The second peak has a adsorption height too large to be explained by adsorption of hydrated cations. Rather, it is similar to species observed after the interfacial formation of nanoparticles from a Pu solution [4].

In contrast, no discernible modulations are detectable after reaction in NaClO₄. The background electrolyte completely suppresses the adsorption of thorium. The total electron density obtained from CTR consists of two layers of adsorbed water and ions other than thorium, presumably mostly Na⁺. The electron density differs from that ob-

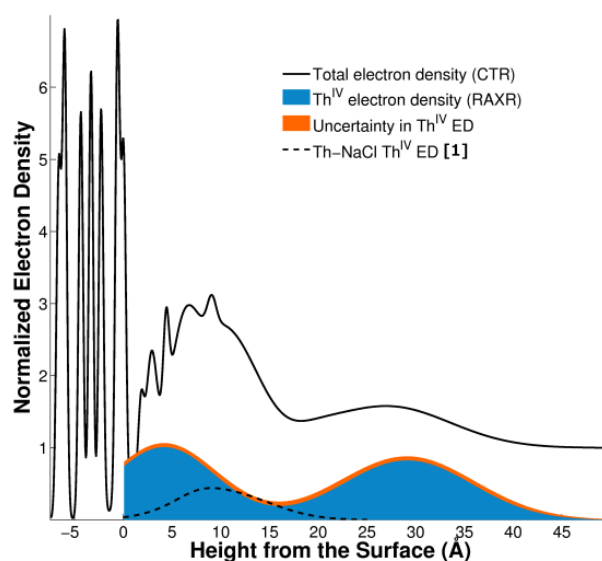


Fig. 1: Total electron density (ED) profile derived from CTR and Th ED distribution derived from RAXR. ED is normalized to that of bulk water $\rho(\text{bulk water}) = 0.33e^-/\text{\AA}^3$, so that the normalized ED of water is 1.00.

served in NaCl in the absence of Th(IV),[3] indicating an effect of ClO₄⁻ also on the adsorption of Na⁺.

The findings are supported by α -spectrometry. For Th-NaClO₄ no signal above background can be detected. This result is constrained by the low specific activity of ²³²Th. In the case of Th-LiClO₄ α -spectrometry finds a thorium coverage of $\theta_a = 1.6 \text{ Th/A}_{UC}$. The lower coverage compared to the RAXR results ($\theta_{RAXR} = 4.9 \text{ Th/A}_{UC}$) must be related to partial desorption of Th. Samples for α -spectrometry were measured *ex situ*, after washing with background electrolyte solution and deionized water. The same washing procedure was shown to partly remove thorium adsorbed from NaCl solution as well [1].

DISCUSSION. It is evident that the background electrolyte has a significant effect on the sorption behavior of thorium. Comparison of NaCl and NaClO₄ solutions clearly shows the adverse effect of the perchlorate anion in this reaction, which fully inhibits the sorption reaction. In LiClO₄, on the other hand, enhanced uptake is observed relative to NaCl. Assuming the adverse role of perchlorate persists in this system, the enhanced uptake must be related to the presence of lithium, e.g. by a beneficial effect on the oligomerization of Th in solution, or by increasing sorption of thorium, leading to the interfacial formation of nanoparticles. The observed anion effect cannot be explained by complexation, which is weak in NaCl and not existent in NaClO₄. Further research will be required to clarify whether the effects are interface or solution related.

[1] Schmidt, M. et al. (2012) *Geochim. Cosmochim. Acta*. **88**, 66–76.

[2] Hofmann, S. et al. (2014) *Geochim. Cosmochim. Acta*. **125**, 528–538.

[3] Lee, S. S. et al. (2012) *Langmuir* **28**, 8637–8650.

[4] Schmidt, M. et al. (2013) *Environ. Sci. Technol.* **47**, 14178–14184.

Uptake of selenium by δ -alumina

C. Franzen, N. Jordan

The sorption of Se(VI) and Se(IV) onto δ -alumina (Al_2O_3) was investigated at different temperatures and ionic strengths. The sorption capacity of alumina towards Se(VI) and Se(IV) is significantly lowered at both higher temperatures and ionic strengths. However, the impact was more pronounced for Se(VI) at higher ionic strength.

One major process controlling the mobility of selenium, a long-lived fission product found in nuclear waste, is the adsorption onto minerals. In this context, it is important to understand to what extent this sorption is influenced particularly by characteristic parameters as expected in deep underground. These parameters include inter alia the presence of different background salts and temperature. For the investigation of the sorption processes, δ - Al_2O_3 was chosen because it is omnipresent in the environment and it represents a model oxide for more complex aluminosilicates.

EXPERIMENTAL. Batch experiments were conducted at a solid-to-solution ratio of 0.5 g L^{-1} and an initial Se concentration of $1 \times 10^{-5} \text{ mol L}^{-1}$. The suspensions were equilibrated for 48 hours. All experiments were conducted in N_2 atmosphere. After centrifugation for two hours at $6,800 \times g$, the remaining selenium concentration in the supernatant was determined by ICP-MS. For the batch experiments, corrections for H^+ concentrations due to the high ionic strengths were done as already published [1].

RESULTS. The effect of temperature and ionic strength on the removal of selenium(IV) and selenium(VI) by δ -alumina is comparatively shown in Fig. 1. At elevated temperature, the influence of the pH on the sorption of Se(IV) and Se(VI) onto δ -alumina shows a similar general tendency, that is, a decrease in the sorption with increasing pH. However, the sorption capacity of alumina towards Se(IV) and Se(VI) is significantly lowered with increasing temperature. This is in agreement with the formerly observed decrease of Se(VI) and Se(IV) sorption onto goethite [2] and alumina (α - Al_2O_3 and γ - Al_2O_3) [3], respectively, with increasing temperature. These findings may significantly increase the mobility of these Se-species and must be taken into account in future safety assessments of nuclear waste repositories.

An increase of the ionic strength from 0.01 to 1 M NaCl led to a significant decrease of Se(VI) sorption. For example, at pH 5 and at 0.01 M NaCl, 88% of Se(VI) was sorbed, whereas at an ionic strength of 1 M, Se(VI) sorption completely vanished. The sorption of Se(IV) onto alumina also showed an ionic strength dependency. However, the impact was not as high as for Se(VI). For example at pH 5, 90% Se(IV) was sorbed at 0.01 M NaCl and 42% Se(IV) was sorbed at 1 M NaCl. These results demonstrate that the oxidation state of selenium is essential in terms of retention by minerals particularly with respect to ionic strengths which might become relevant in deep ground repository.

ACKNOWLEDGEMENTS. The authors thank Aline Ritter, Sabrina Gurlit and Ina Kappler for ICP-MS measurements.

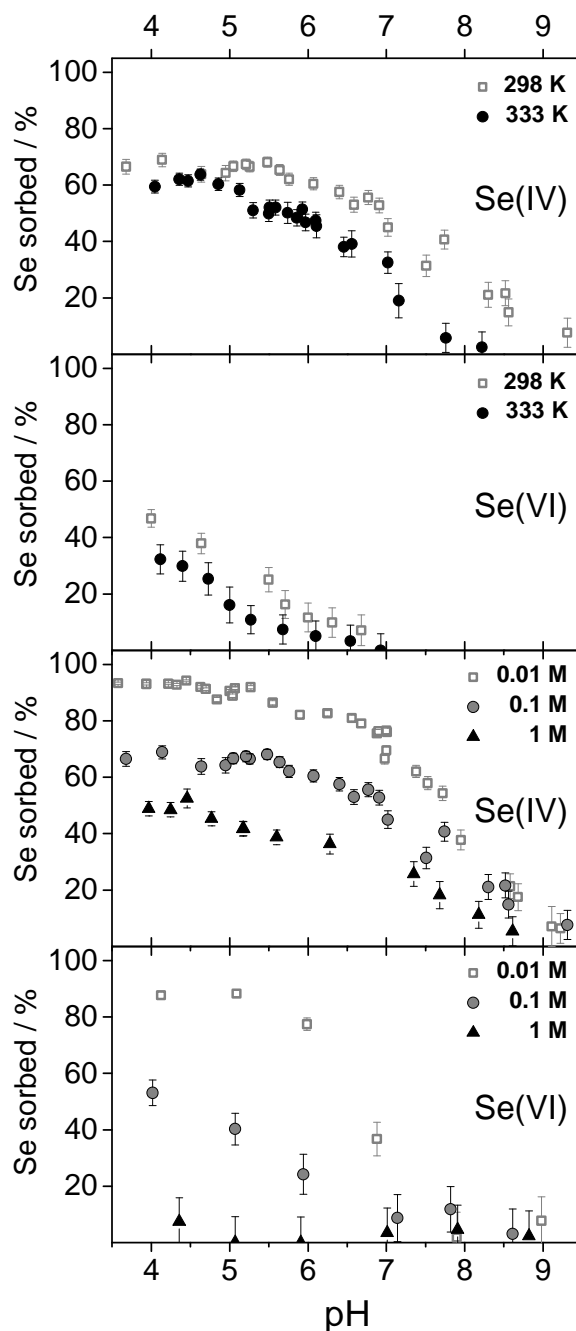


Fig. 1: Sorption edges of Se(IV) and Se(VI) onto δ -alumina for $T = 298 \text{ K}$ and $T = 333 \text{ K}$ (upper panels; $I = 0.1 \text{ M}$) and for different ionic strengths in NaCl (lower panels; $T = 298 \text{ K}$); $[\text{Se}]_{\text{initial}} = 1 \times 10^{-5} \text{ mol L}^{-1}$, $m/v = 0.5 \text{ g L}^{-1}$, 2 days of shaking.

[1] Altmair, M. et al. (2003) *Geochim. Cosmochim. Acta.* **67**, 3595–3601.

[2] Kersten, M. et al. (2013) *Radiochim. Acta* **101**, 413–419.

[3] Parida, K. M. et al. (2003) *Int. J. Environ. Stud.* **60**, 75–86.

Effect of ionic strength on the adsorption of Tb^{3+} onto clay in the presence of fulvic acid

M. Poetsch, H. Lippold

The migration behavior of radionuclides in aquifer systems is influenced by their interactions with rocks and colloid surfaces and by the solvent composition [1]. However, the influence of high ionic strength on reactions in this ternary system has not been examined so far. We investigated the adsorption of Tb^{3+} as an analogue for trivalent actinides onto clay in an aqueous system with ionic strengths up to 4 M in the presence of fulvic acid.

EXPERIMENTAL. ^{160}Tb (half-life 72.3 d) was produced at the TRIGA Mark II reactor at the University of Mainz, Germany. A stock solution of 10^{-4} M [^{160}Tb]terbium in 0.1 M $HClO_4$ was used for the experiments. An Opalinus clay sample (BHE-241) from the Mont Terri rock laboratory (Switzerland) prepared as a suspension with a concentration of $4.8\text{ g}\cdot\text{L}^{-1}$. The fulvic acid was obtained from the moor *Kleiner Kranichsee* in Carlsfeld (Germany) and purified by intermittent precipitation and redissolution with HCl and NaOH.

For the adsorption experiments, variable amounts of NaCl, $CaCl_2$, or $MgCl_2$ were added to the clay suspension. The suspensions were adjusted to pH 5 using HCl. Subsequently, the [^{160}Tb]terbium stock solution was added to achieve a concentration of 10^{-6} M Tb^{3+} . Fulvic acid was dissolved in water (pH 5) and added to the clay suspension resulting in a concentration of $40\text{ mg}\cdot\text{L}^{-1}$.

After equilibrium was reached, the remaining ^{160}Tb concentration in the supernatant was determined by gamma spectrometry.

RESULTS. First, the effect of high ionic strength on the adsorption of Tb^{3+} onto clay was investigated (Fig. 1). The data are presented as solid-liquid distribution coefficient K_d [$L\cdot g^{-1}$]. With increasing ionic strength I (up to almost saturated solutions, $I = 4$ M for NaCl or $I = 12$ M for $CaCl_2$ and $MgCl_2$), K_d values strongly decrease from about $0.75\text{ L}\cdot\text{g}^{-1}$ to $0.01\text{ L}\cdot\text{g}^{-1}$ and $0\text{ L}\cdot\text{g}^{-1}$ for $MgCl_2$ and $CaCl_2$, respectively. Both bivalent cations show a strong influence on the adsorption of Tb^{3+} onto clay at higher concentrations. The K_d values for NaCl decrease from $0.75\text{ L}\cdot\text{g}^{-1}$ to $0.01\text{ L}\cdot\text{g}^{-1}$. The percentage of adsorbed Tb^{3+} decreases from about 80% to 6%, 5% and 0% for NaCl, $CaCl_2$ and $MgCl_2$, respectively.

Figure 2 shows the impact of fulvic acid on the ionic strength-dependent adsorption of Tb^{3+} onto clay. In the presence of fulvic acid, the K_d values are higher compared to the systems without fulvic acid. With increasing ionic strength, the K_d values decrease from $1.49\text{ L}\cdot\text{g}^{-1}$ to $0.02\text{ L}\cdot\text{g}^{-1}$ for $CaCl_2$, to $0.01\text{ L}\cdot\text{g}^{-1}$ for $MgCl_2$ and to $0.16\text{ L}\cdot\text{g}^{-1}$ for NaCl. The percentage of adsorbed Tb^{3+} decreases from about 90% to 40% (NaCl), 8% ($CaCl_2$) and 5% ($MgCl_2$).

CONCLUSIONS. In general, humic substances influence the adsorption of radiometals onto clay minerals [2]. At high ionic strength, slightly increased K_d values were found in the presence of fulvic acid. We conclude that a high ionic strength causes competition and shielding effects and, thus, significantly suppresses adsorption of Tb^{3+} onto clay.

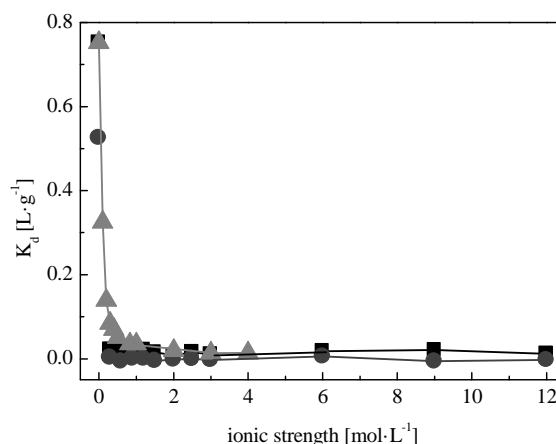


Fig. 1: Plot of K_d values as a function of ionic strength for different electrolytes (▲ NaCl, ■ $CaCl_2$, ● $MgCl_2$).

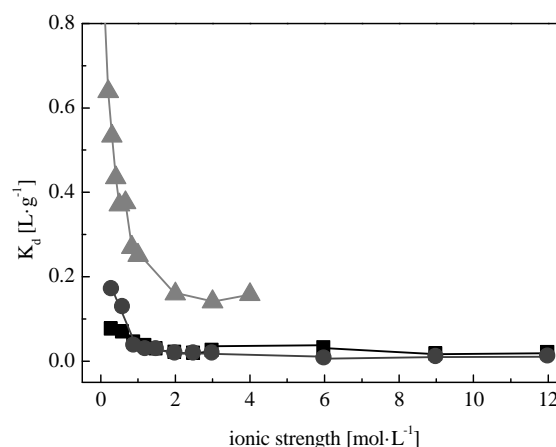


Fig. 2: Plot of K_d values in the presence of fulvic acid (▲ NaCl, ■ $CaCl_2$, ● $MgCl_2$).

ACKNOWLEDGEMENTS. The authors thank the Federal Ministry for Economic Affairs and Energy for financial support of this study (grant no. 02E10971) and the Project Management Agency Karlsruhe (Water Technology and Waste Management Division) for administration.

[1] Geckeis, H. et al. (2008) *J. Contam. Hydrol.* **102**, 187–195.

[2] Lippold, H. et al. (2009) *J. Contam. Hydrol.* **109**, 40–48.

SCIENTIFIC CONTRIBUTIONS (PART III)

**THE CHEMISTRY OF
LONG-LIVED RADIONUCLIDES**

Speciation studies of uranyl(VI) using PARAFAC and luminescence spectroscopy

B. Drobot, R. Steudtner, J. Raff, G. Geipel, V. Brendler, S. Tsushima

This study of uranyl(VI) hydrolysis is an advanced combination of theoretical and experimental methods. Continuous wave luminescence spectroscopy data of uranyl(VI) hydrolysis were analyzed using parallel factor analysis (PARAFAC). Distribution patterns of five major species were thereby derived under a fixed uranyl concentration (10^{-5} M) over a wide pH range from 2 to 11. UV (180 nm to 370 nm) excitation spectra were extracted for individual species. Thus excitation in the UV region is extreme ligand sensitive and specific.

EXPERIMENTAL. Sample preparation was carried out in an inert gas glove box. Uranyl(VI) solutions (10^{-5} M U(VI) in 10^{-2} M NaClO_4) were prepared directly before the experiment. Same solutions without uranyl(VI) were used as blank.

Continuous Wave Luminescence spectroscopy measurements were performed on a fluorescence spectrofluorometer (QuantaMaster 40) equipped with a 75 W xenon arc lamp. Wavelengths were chosen by motorized excitation and emission monochromators with a bandwidth of 10 and 2 nm. Spectra were recorded by scanning emission with 1 nm resolution at each excitation wavelength. This procedure was iterated for the entire excitation range with 5 nm resolution. An integration time of 1 s was chosen. Sample temperature was fixed to 1 °C with a Peltier element. Data from CW spectroscopy were baseline corrected with the recorded blanks.

Data deconvolution was performed by PARAFAC as the N-way [1] toolbox for Matlab software as previously described [2].

RESULTS. PARAFAC was developed as a robust method to determine a unique set of explanatory factors that describe the data.

Data deconvolution with PARAFAC reveals five major species of uranyl(VI) hydrolysis. The preliminary assignment of the species is based on comparison with TRIFS experiments and literature (see [2] and references therein). The species distribution (Fig. 1) is consistent with calculated speciation. Corresponding emission spectra are shown in Fig. 2.

Excitation wavelength was used as the third parameter for 3D data deconvolution. Although differences in UV absorption between 380 and 450 nm are known, the common assumption is that the absorption below 380 nm is structureless and not specific. In this study we focus on the UV range from 180 to 370 nm to verify this thesis.

PARAFAC deconvolution provides individual excitation spectra of uranyl(VI) hydrolysis species. The excitation maxima shift for more than 50 nm from 270 nm (aquo ion) to 325 nm (3:7 complex). Site sensitive excitation is thus demonstrated.

CONCLUSION. The luminescence of uranyl(VI) species is influenced by experimental conditions. Parameters like ionic strength and temperature not only affect the quantum yield but furthermore the lifetime. The same uranyl complex therefore shows different lifetimes under different conditions.

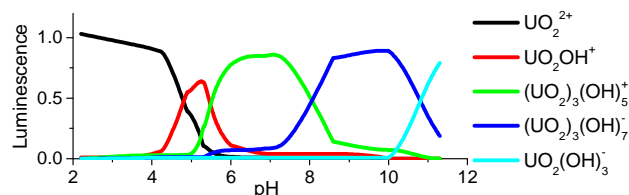


Fig. 1: Distribution of U(VI) hydrolysis species along the pH.

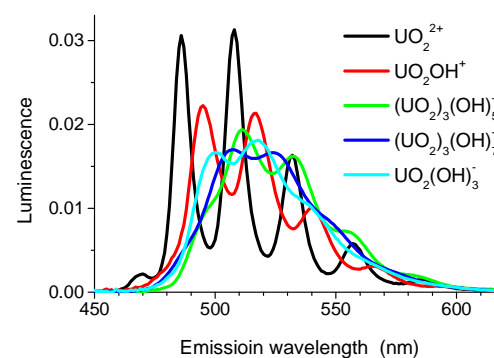


Fig. 2: Emission spectra of 5 major species.

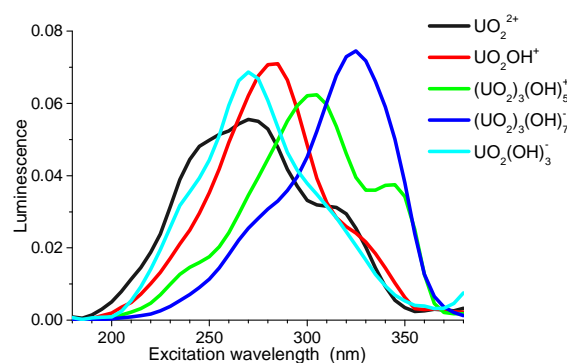


Fig. 3: Excitation spectra of 5 major species.

Contrary to lifetime, the shape of excitation spectra is not affected by those conditions. Furthermore, structural information can be achieved from excitation using quantum chemistry [2].

Here, we demonstrate that strong overlapping bands in excitation spectra can be reliably deconvoluted using multiway methods like PARAFAC. The application of site sensitive excitation is thus very useful for uranyl(VI) speciation studies.

- [1] Anderson, C. A. et al. (2000) *Chemom. Intell. Lab. Syst.* **52**, 1–4.
[2] Drobot, B. et al. (2015) *Chem. Sci.* **6**, 964–972.

How does uranium photochemically trigger DNA cleavage?

S. Tsushima, K. Fahmy

Uranyl(VI) binds to DNA through the phosphate backbone and upon photoexcitation charge transfer from DNA to uranium occurs. During this process U(VI) gets reduced to U(V). The corresponding electron deficiency in the DNA is centred mainly on guanine but gets partly localized also on uranyl free phosphate which may represent a state that precedes DNA strand breakage.

Photocleavage of DNA in the presence of uranium is a well-known phenomenon, yet the reaction mechanism is not fully elucidated. It is believed to occur through hydrogen atom abstraction from DNA by photoexcited uranyl(VI). The “yl”-oxygen in the excited uranyl(VI) is indeed a strong hydrogen acceptor and it can oxidize small organic molecules such as methanol [1] and oxalic acid [2]. In the highest occupied molecular orbitals (HOMOs) of methanol and oxalic acid there is a large contribution from the hydrogen 1s atomic orbitals (AOs) which leads to the involvement of hydrogen atoms in HOMO–LUMO transitions. On the other hand, the HOMOs of the ground state DNA are mainly localized on phosphate groups and on the aromatic rings of the base pairs with little contribution from hydrogen AOs. Thus, it is unlikely that photoexcited uranyl(VI) can abstract hydrogen from DNA. Consequently, we will focus here on the alternative scenario, i.e., direct charge transfer from DNA to uranyl(VI) in the excited state of the uranyl(VI)–DNA adduct.

CALCULATIONS. DFT calculations were performed in gas phase using Gaussian 09 program employing B3LYP hybrid DFT method. The energy-consistent small-core effective core potential and the corresponding basis set were used for U. For H, C, N, O, and P, the 6-31G basis set was used.

RESULTS. Three sets of base pairs (GC and two ATs) linked by phosphate-deoxyribose di-ester backbones were used as a model of DNA (hereafter called “GC/AT/AT”). The structure of the uranyl(VI)–GC/AT/AT adduct where uranyl(VI) is bound through the phosphate group has been calculated at the B3LYP level. To be consistent with previous findings uranyl-to-phosphate coordination was assumed to be unidentate. Figure 1 shows the Mulliken spin density α - β of the lowest-lying triplet state of the U-GC/AT/AT adduct. In the lowest triplet state of the U-GC/AT/AT, the electron deficiency is centered mainly on guanine (G) and adenine (A). Surprisingly, electron deficiency is observed partly also on two phosphate groups sitting opposite of the uranyl binding phosphate. Upon photoexcitation there is electron transfer from DNA to uranyl. It is known that oxidative DNA damage can occur through long-range electron transfer (up to 37 Å, [3]). Hence, the present result, in which long range electron transfer is observed, is not surprising.

Half of the two unpaired electrons is localized on uranyl and the rest is distributed on guanine, adenine, and free phosphate. The spin density of the UO_2 moiety is close to 1.00 and the unpaired electron on uranium is localized on the non-bonding U $5f_8$ or $5f_0$ orbitals constituting a $5f^1$ electronic configuration. Therefore, one can reasonably assume that the oxidation state of uranium is U(V). The

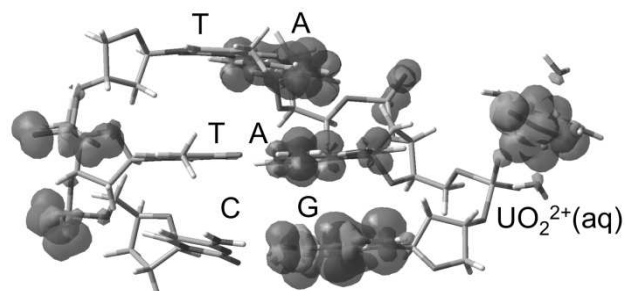


Fig. 1: Structures and Mulliken spin density α - β of the lowest-lying triplet states of U-GC/AT/AT adduct. Isovalue of the surface is 0.0004 a.u.

GC/AT/AT part is oxidized with a loss of one electron. The electron deficiency gets mainly centered on guanine because of the low oxidation potential of this residue compared to cytosine, thymine, and adenine [4]. The model having only two AT pairs (AT/AT) has been also tested. Similar to the GC/AT/AT case, photoinduced electron transfer from AT/AT to uranyl is observed in the lowest-lying triplet state of the U-AT/AT adduct. Roughly half of the spin density is localized on the uranyl unit and the rest is distributed on adenine and thymine and on free phosphate group. Therefore, also in the U-AT/AT adduct upon photoexcitation there is a DNA-to-uranyl charge transfer and U(VI) gets reduced to U(V). However, in the lowest triplet state of the U-AT/AT adduct, when compared to U-GC/AT/AT, there is larger electron deficiency in the free phosphate group. Apparently, guanine is the best electron donor and in its absence, its role is substituted by phosphate and/or other nucleobases. From this result, it appears that the efficiency of phosphate oxidation and, thereby, the cleavage of DNA, increases if guanine is absent in the vicinity of uranium.

ACKNOWLEDGEMENTS. We acknowledge generous access to the supercomputer at the Center for Information Services and High Performance Computing, Technische Universität Dresden, Dresden, Germany.

- [1] Tsushima, S. (2009) *Inorg. Chem.* **48**, 4856–4862.
- [2] Tsushima, S. et al. (2010) *Dalton Trans.* **39**, 10953–10958.
- [3] Hall, D. B. et al. (1996) *Nature* **382**, 731–735.
- [4] Steenken, S. et al. (1997) *J. Am. Chem. Soc.* **119**, 617.

The formation of intrinsic actinide colloids under nuclear waste repository conditions

H. Zänker, S. Weiss, C. Hennig, A. Ikeda-Ohno, V. Brendler

Trivalent and tetravalent actinides form “intrinsic” (or “homogeneous”) colloids in the laboratory. However, little is known about the occurrence of such colloids in natural aquatic environments. In this short review, consequences of their potential formation in nature are discussed.

Due to their low solubility, trivalent actinides (An(III)) and tetravalent actinides (An(IV)) are often assumed to be immobile in natural aquatic environments. However, they can also become mobile if they occur as colloids. Colloids are generally classified into two types: “pseudocolloids” and “intrinsic” colloids. The latter – which have also been referred to as “homogeneous” colloids [1] and which are the subject of this review – consist of polymerized An complexes linked with anions [2]. This type of colloids is formed via condensation induced by hydrolysis.

FORMATION OF INTRINSIC AN COLLOIDS. Stable intrinsic An colloids can easily be produced in the laboratory (cf. [3] and references therein) – but little is known about the occurrence of such colloids in nature. Most laboratory experiments have been done on water-borne *An(IV) oxyhydroxide colloids* [2, 4]. They are formed by neutralizing acidic solutions of An(IV) species. *An(III)- and An(IV)-silica colloids* are produced by neutralizing acidic solutions or alkaline carbonate solutions of An(III) or An(IV) in the presence of silicic acid [5–7]. They can be stabilized in the water-borne form with significantly higher concentrations than those for the An(IV) oxyhydroxide colloids. The silica is incorporated into the matrix of the colloidal particles. Figure 1 illustrates this silica incorporation in Np(IV)-silica colloids (the Si/An ratio may increase from the particle center to the particle surface).

Geckeis et al. [2] have defined intrinsic colloids as those formed by condensation of hydrolyzed metal ions linked with anions. According to this definition, we would classify the An(III)- and An(IV)-silica colloids as intrinsic colloids. However, since the silica/An ratio within such colloids can be relatively high, these colloids could also be referred to as pseudocolloids (not following the Geckeis definition). Another example is *An(III)-aluminosilicate colloids*. Kim et al. [8] produced Cm(III)-aluminosilicate colloids by neutralizing solutions containing Cm(III), silicic acid and Al(III). Here, Cm(III) acts as an isomorphic substitution to Al(III); structural incorporation of Cm(III) into the aluminosilicate matrix is assumed. These particles could be referred to as intrinsic colloids according to the definition by Geckeis et al. However, they would also be classified as pseudocolloids because their silica/Cm ratio can be very high. A last example is *An(IV) clusters* [9]. The size of these clusters approaches or lies in the lower colloidal size range. They show very well defined structures. Chloride or organic acids such as carboxylic acids or amino acids act as bridging ligands which stabilize these clusters with specific atomic numbers such as 6, 10, 38 etc. The clusters are stable in the water-borne state at relatively low pH (< 3 ~ 4) only.

GEOCHEMICAL IMPLICATIONS. All the colloids and clusters summarized here have the potential to in-

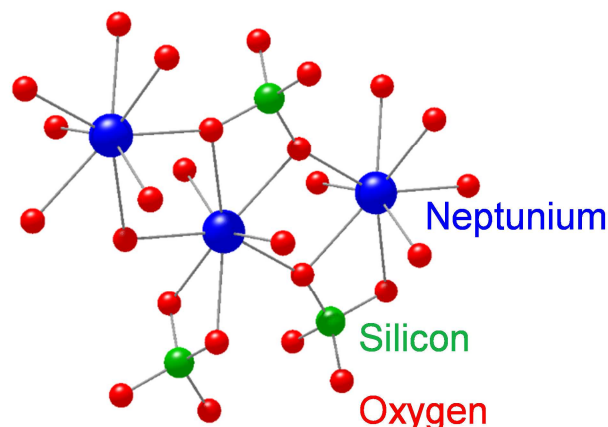


Fig. 1: Structure model of Np(IV)-silica colloids according to EXAFS.[7]

crease the concentration of An(III) or An(IV) by several orders of magnitude compared to their thermodynamic solubility. The question is if such water-borne An(III) or An(IV) particles would be formed in a nuclear waste repository after the access of groundwater or surface water. The formation of *An(IV) clusters* according to [9] is less likely under the actual geological conditions since acidic conditions are not expected in a nuclear waste repository. However, such clusters may play an important role in abandoned uranium mines where acidic leaching was applied. On the other hand, the formation of other intrinsic colloids cannot be ruled out in a nuclear waste repository because they are stable at near-neutral pH and requisite chemicals (e.g. dissolved silicic acid or aluminum) could be found in significant amounts. Based on this fact, the following points should be clarified for the safety assessment of nuclear waste repositories:

- (i) the formation of intrinsic An colloids under the complex chemical conditions of a nuclear waste repository should be assessed;
- (ii) if intrinsic An colloids could be present, their ability to diffuse through the geochemical and the geological barriers should be evaluated;
- (iii) the behavior of intrinsic An colloids in the bentonite porewater/groundwater mixing zone should be identified;
- (iv) the behavior of intrinsic An colloids after the access of glacial melt water due to a future ice age should be assessed.

Answering these questions will help to develop better models for describing the colloid-facilitated transport of actinides in the environment.

-
- [1] Möri, A. et al. (2003) *Coll. Surf. A: Physicochem. Eng. Aspects* **217**, 33–47.
 - [2] Geckeis, H. et al. (2011). In: Kalmykov, S., Denecke, M.A. (Eds.), *Actinide Nanoparticle Research*, p. 1–30, Springer.
 - [3] Zänker H. et al. (2014) *J. Contam. Hydrol.* **157**, 87–105.
 - [4] Altmaier, M. et al. (2004) *Radiochim. Acta* **92**, 537–543.
 - [5] Panak, P. J. et al. (2003) *Coll. Surf. A: Physicochem. Eng. Aspects* **227**, 93–103.
 - [6] Dreissig, I. et al. (2011) *Geochim. Cosmochim. Acta* **75**, 352–367.
 - [7] Husar, R. et al. (2015) *Environ. Sci. Technol.* (DOI: 10.1021/es503877b).
 - [8] Kim, M. A. et al. (2005) *Coll. Surf. A: Physicochem. Eng. Aspects* **254**, 137–145.
 - [9] Knope, K. E. et al. (2013) *Chem. Rev.* **113**, 944–994.

Ionic strength dependency of the Eu(III)-(poly)borate complexation

J. Schott,¹ J. Kretzschmar, M. Acker,¹ A. Barkleit, S. Taut,¹ V. Brendler

¹Central Radionuclide Laboratory, Technische Universität Dresden, Dresden, Germany

The Eu(III)-(poly)borate complexation was studied at $\text{pH}_c = 6$ as a function of ionic strength ($I_m = 0.1 \dots 3 \text{ m}$ ($\text{m} \equiv \text{mol/kg}$), NaCl) by means of time-resolved laser-induced fluorescence spectroscopy (TRLFS).

By now, (poly)borates are regarded as relevant ligands in a nuclear waste repository (occurrence in natural salt deposits and brines, corrosion products of glass coquilles). Hence, it is necessary to study their potential to mobilize actinides, e.g. in the near and far field of a nuclear waste repository [1, 2].

Recently, a better understanding of chemical processes (complexation, formation of solid phases) in the M(III)-(poly)borate ($M = \text{Eu, Nd, Cm}$) system was obtained [3, 4]. (Poly)borates are weak complexing agents for trivalent actinides/lanthanides ($\lg \beta_1 = 2.0 \dots 2.5$, $I_m = 0.1 \text{ m}$). In the case of water ingress into a repository, conditions of high ionic strengths are to be expected. Hence, the aim of this work was to study the influence of higher ionic strengths ($I_m > 0.1 \text{ m}$, NaCl) on the Eu(III)-(poly)borate complexation. From this ionic strength dependency the complexation constant at infinite dilution ($\lg \beta^0$) and ion interaction coefficients ($\Delta\epsilon$, $\epsilon(\text{K}^{n+}$, A^{m-}) are deducible using the "Specific Ion Interaction Theory" (SIT) [5], Eq. 1:

$$\lg \beta_n = \lg \beta_n^0 + D \cdot \Delta z^2 - \Delta\epsilon \cdot I_m \quad (1)$$

D ...Debye-Hückel term, Δz^2 ...difference of ion charges, $\Delta\epsilon$...difference of ion interaction coefficients, I_m ...ionic strength.

EXPERIMENTAL. Solutions with variable total boron content (0, 0.1–0.7 m, $\text{B}(\text{OH})_3$) and $I_m = 0.1 \text{ m}$ (NaCl) were prepared at $\text{pH}_c = 6$ under ambient conditions ($T = 22 \text{ }^\circ\text{C}$, $p_{\text{CO}_2} = 10^{-3.5} \text{ bar}$), and were equilibrated at least one week. Appropriate amounts of NaCl were added to the borate solutions to adjust ionic strengths up to 3 m. The solutions were equilibrated at least four days. Eu(III) ($3 \times 10^{-5} \text{ m}$) was added to each solution prior to the TRLFS measurements. TRLFS was carried out with a Nd:YAG-OPO laser system (Continuum, USA). Stationary and time-resolved spectra of the solutions were recorded (pulse energy: 2 mJ, $\lambda_{\text{exc}} = 394 \text{ nm}$, delay time: 20 μs).

RESULTS. As it was already shown in our recent study [6] and in literature [7, 8], the polyborate speciation is not significantly influenced by ionic strength (NaCl). Therefore, the formation constants of polyborates from literature [7] were applied for ionic strengths up to 3 m (NaCl). Within a series of constant ionic strength an increase of the ${}^5\text{D}_0 \rightarrow {}^7\text{F}_0$ and ${}^5\text{D}_0 \rightarrow {}^7\text{F}_2$ luminescence transition bands with increasing total boron content was observed (Fig. 1a). This illustrates the Eu(III) complexation by polyborates at $\text{pH}_c = 6$. With increasing ionic strength (NaCl), the F_1/F_2 ratio increased for samples of same composition indicating a reduction of complexation strength in the Eu(III)-(poly)borate system (Fig. 1b). The analysis of the ionic strength dependency of the complexation (Eq. 1) yielded a linear correlation (Fig. 1c).

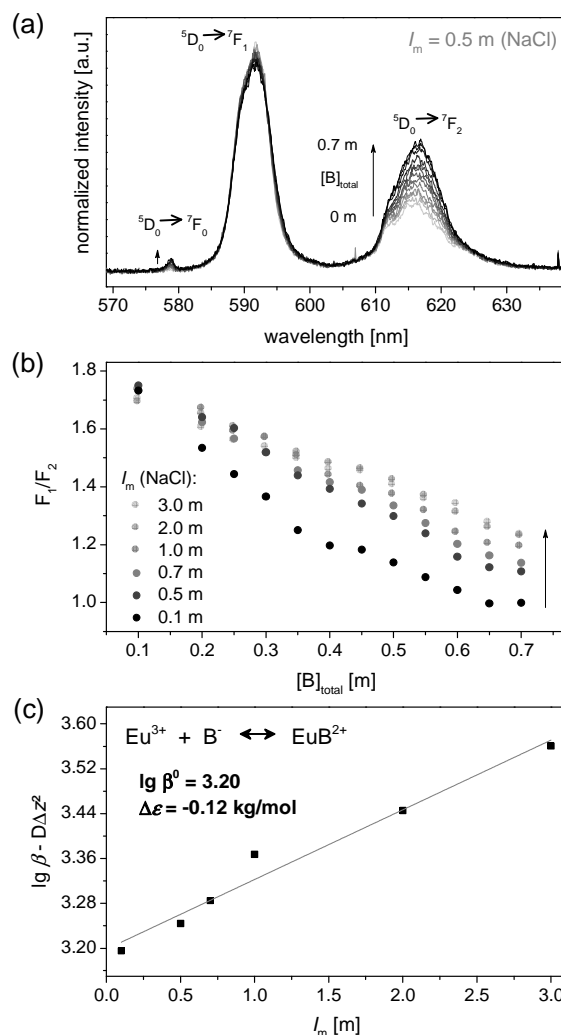


Fig. 1: (a) Europium luminescence spectra and (b) F_1/F_2 ratio in dependency on total boron content, (c) SIT plot for the studied system.

From the intercept and slope of the regression line, values for $\lg \beta^0$ and $\Delta\epsilon$ were derived (summarized in Fig. 1c).

SUMMARY. The weak An/Ln(III) complexation by (poly)borates and, hence, the minor mobilization potential of borates regarding An/Ln(III) are additionally reduced by high ionic strength conditions.

ACKNOWLEDGEMENT. This work is funded by BMWi under contract number 02E11021.

[1] Borkowski, M. et al. (2010) *Radiochim. Acta* **98**, 577–582.
 [2] Altmairer, M. et al. (2013) *Chem. Rev.* **113**, 901–943.
 [3] Schott, J. et al. (2014) *Dalton Trans.* **43**, 11516–11528.
 [4] Hinz, K. et al. (2014) *New J. Chem.* **39**, 849–859.
 [5] Hummel, W. (2005) *Chem. Thermodyn.* 9, Elsevier, Amsterdam.
 [6] Schott, J. et al. (2013) *Report HZDR-030*, p. 56.
 [7] Ingri, N. et al. (1962) *Acta Chem. Scand.* **16**, 439–448.
 [8] Mesmer, R. E. et al. (1972) *Inorg. Chem.* **11**, 537–543.

Spectroscopic studies on the Eu(III)/Am(III)-oxalate systems at high ionic strengths

F. Taube,¹ M. Acker,¹ B. Drobot, S. Taut¹

¹Central Radionuclide Laboratory, Technische Universität Dresden, Dresden, Germany

The complex stability constant (extrapolated to I = 0 using the Specific Ion Interaction Theory - SIT) of Eu-oxalate was determined by time-resolved laser fluorescence spectroscopy (TRLFS) at high ionic strengths. The 1 : 1 Am-oxalate complex was studied using UV-vis spectroscopy.

Oxalic acid is a widespread metabolite of decomposition processes occurring in soil or in surface waters in the millimolar range [1]. Understanding the migration of radionuclides and small organic molecules (like oxalate) in radioactive waste repositories is crucial for their safety assessment. Thus, respective thermodynamic data at high ionic strengths as present in pore waters of German clay formations are required. [2]

EXPERIMENTAL. The set-up of the fluorescence spectrometer is described in [3]. Stock solutions of 0.05 M oxalic acid and EuCl₃ (5 μM) were prepared at pH ~1.95, with NaCl adjusting the ionic strength (0.05–2 m). Aliquots of the oxalate solution (10–50 μL) were titrated into 2.5 mL of the Eu-solution. The time-resolved spectra were measured in 10–20 μs steps and the decay curves were fitted mono-exponentially using OriginPro 8.6. For UV-vis a 13 μM Am-243 solution was prepared in HCl and NaCl (total proton concentration equals the oxalate solution). 1–2 μL aliquots of 0.05 M oxalic acid were added (pH ~2, at the same ionic strength), stirred for 5 min and the spectra recorded on a Carl Zeiss MCS601 spectrometer.

RESULTS. The europium fluorescence spectra (Fig. 1, left) show typical intensity changes, i.e. an increase of the F₂-transition and the appearance of the F₀-peak with rising oxalate concentration. The lifetime (average over 0.05–2 m NaCl) increases from 112 ± 5 μs (n_{H₂O} = 9.0 ± 0.5, calculated according to [4]) for Eu³⁺ up to 149 ± 8 μs (n_{H₂O} = 6.6 ± 0.5) at ~8 mM oxalate for the dominating 1 : 1 Eu-oxalate-complex. A PARAFAC analysis [5] even confirms the presence of a 1 : 2 complex. Average values for the stability constants of the complexes were generated using SPECFIT and a slope analysis. Extrapolation to infinite dilution (log β⁰) with SIT [6] gave values in good agreement with literature (Tab. 1, SIT plots in Fig. 2). For the first time, the interaction coefficient sums Δε₁ and Δε₂ for the Eu-oxalate complexation were determined. The individual values ε (EuOx⁺, Cl⁻) = -0.13 ± 0.09 kg·mol⁻¹ and ε (EuOx₂⁻, Na⁺) = -0.58 ± 0.47 kg·mol⁻¹ were then derived with ε values for (Eu³⁺, Cl⁻) and (Ox²⁻, Na⁺) taken from [6].

UV-vis spectra of Am(III) showed a red shift of the band from 503 nm to 508 nm with rising oxalate concentration (Fig. 1, right). At given concentrations, the limit of solubility of the 2 : 3 complex was reached and the spectra were impacted at oxalate concentrations above ~2 mM. Hence, these spectra were not included in the spectral analysis. Nevertheless, the experimental data are in good accordance with literature data (Tab. 1). The ε value for (AmOx⁺, Cl⁻) was calculated to be -0.10 ± 0.05 kg·mol⁻¹ using ε (Am³⁺, Cl⁻) and ε (Ox²⁻, Na⁺) according to [6]. As expected, this is close to the respective Eu parameter.

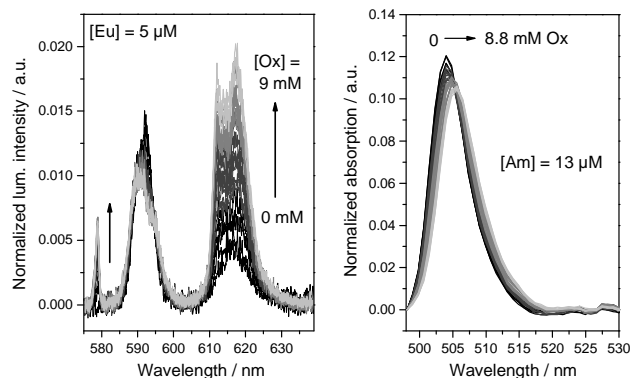


Fig. 1: Spectroscopic studies of Eu/Am-oxalate titration at I = 1 m NaCl and [Ox] = 0.05 M, pH ~2; left: Luminescence spectra of [Eu] = 5 μM, right: UV-vis spectra of [Am] = 13 μM.

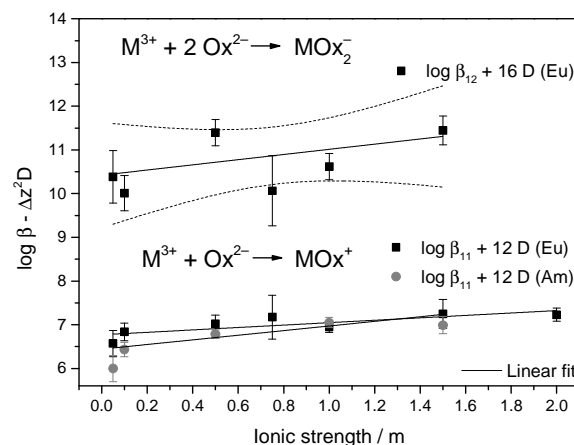


Fig. 2: SIT plots for the 1 : 1 and 1 : 2 complexes of the Eu-oxalate-system including the SIT plot for the 1 : 1 Am-oxalate-complex.

Tab. 1: log β⁰ (T = 25 °C) and Δε values in NaCl extrapolated to I = 0 using SIT.

Metal/ Ligand	log β ₁₁ ⁰	Δε ₁ / mol/kg	log β ₁₂ ⁰	Δε ₂ / mol/kg
Eu-oxalate	6.77 ± 0.09	-0.28 ± 0.09	10.23 ± 0.4	-0.65 ± 0.5
Eu-oxalate*	6.72		11.22	
Am-oxalate	6.67 ± 0.04	-0.25 ± 0.05		
Am-oxalate**	6.51 ± 0.15	-0.33 ± 0.10	10.71 ± 0.2	-0.54 ± 0.1

*: in NaCl/NaClO₄ from [7]; **: in NaCl/NaClO₄, from [6].

ACKNOWLEDGEMENT. The project is funded by BMWi (number: 02E11021).

- [1] Gammons, C. H. et al. (2000) *Chem. Geol.* **166**, 103–124.
- [2] Kienzler, B. (2003) *Report FZK-INE 002/03*.
- [3] Barkleit, A. et al. (2014) *Dalton Trans.* **43**, 11221–11232.
- [4] Horrocks, W. et al. (1979) *J. Am. Chem. Soc.* **101**, 333–340.
- [5] Drobot, B. et al. (2015) *Chem. Sci.* **6**, 964–972.
- [6] Hummel, W. (2005) *Chem. Thermodyn.* **9**, Elsevier, Amsterdam.
- [7] Wood, S. A. (1993) *Engin. Geol.* **34**, 229–259.

Lactate protonation and Eu(III)-lactate complexation studied by ITC (I = variable)

F. Taube, M. Acker, S. Taut

Central Radionuclide Laboratory, Technische Universität Dresden, Dresden, Germany

The lactate protonation as well as the Eu(III)-lactate complexation were studied by Isothermal Titration Calorimetry (ITC) in dependence on the ionic strength I (0.1–2 m NaCl). The enthalpies and stability constants were extracted from the heat curves and extrapolated to infinite dilution (I = 0) using SIT.

Lactate, an α -hydroxycarboxylic anion appears as metabolite in many biological processes. It represents a great variety of small organic molecules. They also occur in ground or pore water in geological formations for potential nuclear waste repositories. It is very important to know thermodynamic data of the complexation reactions of the radionuclide – organic molecule – systems to assess its effects on the contaminant migration.

Isothermal titration calorimetry measures the reaction enthalpies directly, stability constants can be determined simultaneously. Then, the free energy and the entropy of the reaction can be derived. [1]

EXPERIMENTAL. For the lactate protonation sodium lactate solutions (10 or 20 mM, pH ~ 6–7) were titrated with a 0.1 M and a 0.2 M HCl, respectively. For the complexation solutions of 14 mM Eu(III) and 38 mM lactate were prepared and titrated with a 0.1–0.25 M HCl. The ionic strength was adjusted by NaCl.

The experiments used the isothermal microcalorimeter MicroCal iTC₂₀₀ (GE Healthcare) which adds reactants (V = 40 μ L) automatically in 1–2 μ L steps into the reaction cell (analyte, V = 200 μ L). The integrated heat curves are corrected for the dilution heat determined separately by titrating the ligand into the medium. These data are then least-square fitted using the programs Hyp Δ H (Protonic software) [1] and OriginPro, fed with an adequate chemical model.

RESULTS. With increasing ionic strength, both enthalpies (lactate protonation and Eu-lactate complexation) become more exothermic or change from endothermic to exothermic (Fig. 1). This trend was observed previously and can be explained by the agglomeration of sodium ions around the lactate anion or the complex in the second coordination sphere. This agglomeration decreases the energy necessary to dehydrate the analyte so that the binding

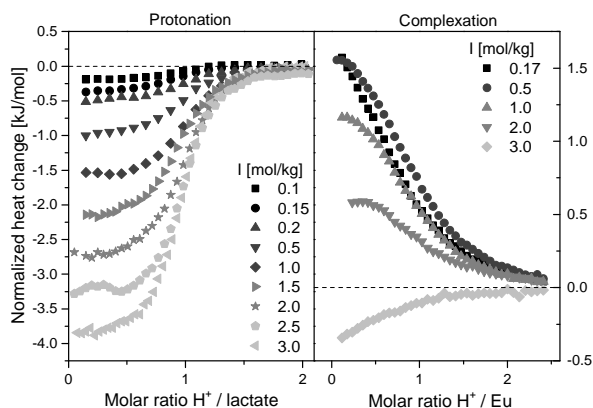


Fig. 1: Heat curves (I variable) of 10 mM lactate (left) and 14 mM Eu and 38 mM lactate (right) with HCl. Heat changes were normalized to the HCl concentration.

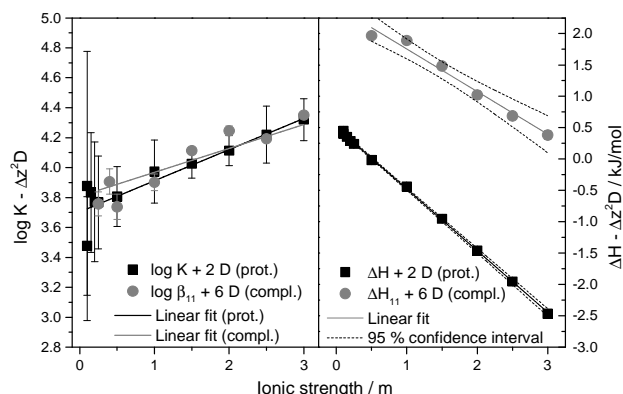


Fig. 2: SIT plots of the lactate protonation and the Eu-lactate complexation; D: Debye-Hückel term, Δz : ion charge difference.

Tab. 1: Extrapolated $\log \beta^0$, ΔH^0 and $\Delta \epsilon$ values at I = 0 using SIT.

Reaction	$\log \beta_{11}^0$	$\Delta \epsilon_1$ / kg mol^{-1}	Ref.
$\text{Lac}^- + \text{H}^+ \rightleftharpoons \text{LacH}$	3.77 ± 0.02	-0.17 ± 0.01	p.w. [5], *
$\text{Eu}^{3+} + \text{Lac}^- \rightleftharpoons \text{EuLac}^{2+}$	3.81 ± 0.09	-0.16 ± 0.04	p.w. [2]**

*: at 1 M NaClO₄; **: Van't Hoff plot.

Reaction	ΔH_{11}^0 / kJ mol^{-1}	$\Delta \epsilon_L \cdot 10^{-3}$ / kg (mol K)^{-1}	Ref.
$\text{Lac}^- + \text{H}^+ \rightleftharpoons \text{LacH}$	0.51 ± 0.02	1.24 ± 0.02	p.w. [5], *
$\text{Eu}^{3+} + \text{Lac}^- \rightleftharpoons \text{EuLac}^{2+}$	2.43 ± 0.10	0.92 ± 0.08	p.w. [2]**

*: at 1 M NaClO₄; **: Van't Hoff plot; OH group not considered.

energy becomes more dominant. [2] The stability constants extrapolated to infinite dilution ($\log \beta^0$) using SIT agree well with literature data (Fig. 2 and Tab. 1). The slope of the SIT plot provides $\Delta \epsilon$ from which the individual interaction coefficients ϵ (short-range forces) of each species can be derived according to the reaction equation. The ϵ -value of $0.05 \pm 0.01 \text{ kg} \cdot \text{mol}^{-1}$ for (Lac^- , Na^+) was calculated using $\Delta \epsilon_1$ (Tab. 1) and ϵ (H^+ , Cl^-) according to [3]. This value is similar to those found for acetate ($0.08 \pm 0.01 \text{ kg} \cdot \text{mol}^{-1}$) used as an analogue for lactate [4]. The value of ϵ (EuLac^{2+} , Cl^-) was calculated to be $0.12 \pm 0.05 \text{ kg} \cdot \text{mol}^{-1}$ using ϵ (Eu^{3+} , Cl^-) according to [3]. For the first time, not only $\Delta \epsilon_1$ and the individual ϵ -values but also the enthalpic $\Delta \epsilon_L$ were determined for the Eu-Ox complexation. With $\Delta \epsilon_L$, one can describe the ionic strength dependency of the reaction heat. The good results demonstrate that ITC can be applied to trivalent actinide complexation, e.g. to Am(III).

ACKNOWLEDGEMENT. The project is funded by BMWi (number: 02E11021).

- [1] Gans, P. et al. (2008) *J. Sol. Chem.* **37**, 467–476.
 [2] Barkleit, A. et al. (2014) *Dalton Trans.* **43**, 11221–11232.
 [3] Hummel, W. (2005) *Chem. Thermodynamics 9*, Elsevier, Amsterdam.
 [4] Ciavatta, L. (1990) *Anal. Chim.* **80**, 255–263.
 [5] Tian, G. et al. (2010) *Inorg. Chem.* **49**, 10598–10605.

Complexation of trivalent *f*-elements with amides in solution

J. März, H. Moll, G. Geipel, K. Gloe¹

¹Department of Chemistry and Food Chemistry, Technische Universität Dresden, Dresden, Germany

A 2-picolyl substituted methane tricarboxamide (MTCA) was synthesized to investigate its complexation property with trivalent lanthanides (Ln(III) = La, Ce, Nd, Sm, Eu, Gd and Yb) and actinides (An(III) = Cm) in solution. The ligand was obtained by a condensation reaction in xylene. The complex formation has been confirmed by NMR and Time-Resolved Laser-Induced Fluorescence spectroscopy (TRLFS).

The complexation properties of trivalent *f*-elements (i.e. Ln(III) and An(III)) with β -diketones have been well investigated, while those with structurally comparable amides are still poorly understood. However, amides could potentially coordinate to metal ions more efficiently particularly in pH-neutral solutions than β -diketones, due to the mesomerism of the amide group. This study aims to investigate the complexation behavior of Ln(III) and An(III) with an amide ligand under physiologically relevant conditions.

EXPERIMENTAL. The ligand synthesis was performed under N₂ atmosphere with standard Schlenk techniques. Solvents used in this study were pre-dried over molecular sieves and CaCl₂. MTCA was synthesized by a condensation of triethyl methanetricarboxylate and 2-picolylamine in xylene and recrystallization from acetone. The structure of MTCA is illustrated in Fig. 1. Precipitates of Ln(III)-MTCA complexes were obtained from a mixture of Ln(III) nitrate and MTCA in THF by a microwave treatment (5 min at 100 °C). Those precipitates were dried and re-dissolved in a H₂O/MeOH mixed solution (H₂O:MeOH = 5:1 in volume). The resultant solutions of Ln(III)-MTCA complexes were employed for TRLFS measurements. Solutions of Cm(III)-MTCA complex were prepared under N₂ atmosphere by mixing an aqueous solution of 0.3 μ M Cm(III) with 0.3 mM MTCA in 0.1 M NaClO₄. TRLFS measurements were performed with a femtosecond Nd:YAG laser system (Powerlite Precision II 9020 + OPO by Continuum, USA).

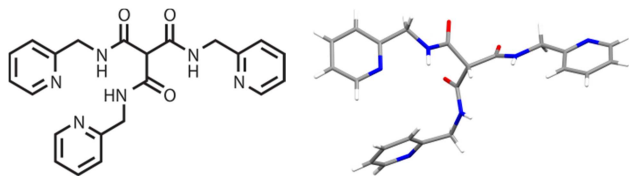


Fig. 2: Scheme and structure of MTCA.

RESULTS. The excitation of Ln(III)-MTCA complexes at 510 nm produced a broad emission band at around 570 nm, while the fluorescence intensities varied depending on the Ln(III) center. It was pre-confirmed that MTCA itself is non-fluorescent under the same conditions and, hence, the observed emission band should originate in the complex formation between Ln(III) and MTCA. When measuring the fluorescence decay of the Ln(III)-MTCA complexes, their fluorescence lifetimes exhibited a second order exponential behavior with two independent fluorescence lifetimes ranging from 25 to 870 ns. This result suggests the presence of two different species in the

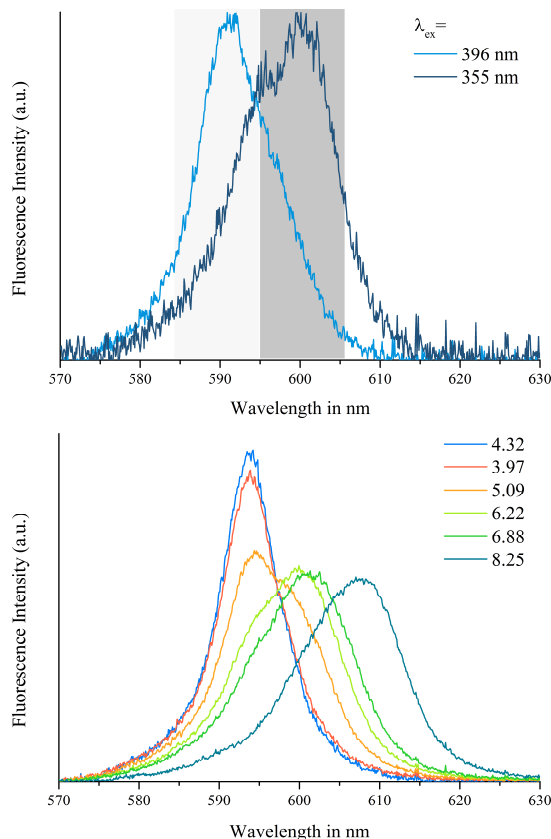


Fig. 1: Fluorescence spectra of Cm(III)-MTCA complexes excited at 396 and 355 nm at pH \approx 5 (top) and excited at 396 nm with varying pH (bottom).

samples, which is also supported by NMR measurements for La(III)-MTCA and Eu(III)-MTCA complexes [1]. In contrast to Ln(III), Cm(III) allows us to excite the metal center directly, in addition to the indirect excitation *via* the ligand. When the Cm(III)-MTCA solution was excited with 355 nm (indirect excitation *via* the ligand), the fluorescence spectrum showed a clear peak at 600 nm (colored with grey in Fig. 2, top) which indicates the formation of a Cm(III)-MTCA complex. The additional shoulder peak at 593 nm can be assigned to the direct excitation of Cm(III) from [Cm(H₂O)₉]³⁺ (Fig. 2, top). The hydration number of Cm(III) can be estimated from the fluorescence lifetime based on the *Kimura-Choppin* equation [2]. According to this equation, the fluorescence lifetime of 115 μ s for the complex Cm(III)-MTCA can be assigned to 4.8 ± 0.9 water molecules around the Cm(III) center. Assuming the coordination number of nine for the pure aquo Cm(III) complex, the remaining three to five coordination sites could be occupied with the MTCA ligand and coordination, indicating the formation of a complex with Cm:MTCA = 1:2. The fluorescence spectra of Cm(III)-MTCA complexes show a pH dependence with bathochromic shifts of 6 nm and 14 nm, as an increase in pH (Fig. 2, bottom).

ACKNOWLEDGEMENTS. J.M. acknowledges the German Federal Ministry of Education and Research for funding (02NUK014).

[1] Lakowicz, J. R. (2006) *Principles of Fluorescence Spectroscopy*.
[2] Kimura, T. et al. (1994) *J. Alloys. Compd.* **213/214**, 313–317.

The aqueous speciation of Se(IV): impact of concentration. Part 1: IR and MP2 studies

N. Jordan, J. Kretzschmar, E. Brendler,¹ S. Tsushima, C. Franzen, H. Foerstendorf, K. Heim, V. Brendler

¹Institute of Analytical Chemistry, Technical University Bergakademie Freiberg, Freiberg, Germany

The impact of concentration on the aqueous speciation of selenium(IV) was elucidated in this work by applying infrared (IR) spectroscopy and quantum chemical calculations. The dimerization of hydrogen selenite (HSeO_3^-) was confirmed at concentrations above 10 mmol L^{-1} by IR spectroscopy. Quantum chemical calculations using the second-order Møller–Plesset Perturbation theory (MP2) provide the assignment of vibrational bands observed to specific molecule modes of the $(\text{HSeO}_3)_2^{2-}$ dimer. Geometry optimization by MP2 enabled obtaining the most stable configurations of the dimer.

The still most comprehensive overview about selenium chemistry is presented by the respective volume of the OECD/NEA Thermochemical Database by Olin et al. [1]. One of the open questions left is a detailed characterization of the dimerization of aqueous HSeO_3^- ions, starting at concentrations around 1 mmol L^{-1} [2]. Olin et al. reported a broad variety of studies supporting this phenomenon. Torres et al. [2] presented a set of thermodynamic constants for this system recently, but their list of species is not backed-up by independent spectroscopic evidence. This work combines IR and MP2 calculations and thus provides vibrational data including the identification of the vibrational modes of four different molecule's geometries, i.e. SeO_3^{2-} , HSeO_3^- , and two configurations of the $(\text{HSeO}_3)_2^{2-}$ dimer (Fig. 1).

EXPERIMENTAL. Samples were prepared at varying Se(IV) concentrations ranging from 1 mmol L^{-1} up to 1 mol L^{-1} at pH_c 5, at constant ionic strength of 3 mol L^{-1} (adjusted with NaCl if necessary). The IR measurements and MP2 calculations, described elsewhere [3], were supported by recording the ^{77}Se NMR chemical shift of Se(IV) solutions at different concentrations and pH [4].

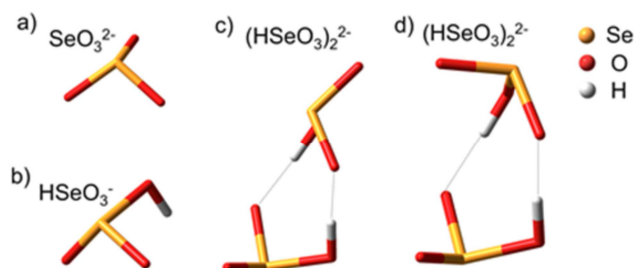


Fig. 1: Optimized structures of SeO_3^{2-} (a), HSeO_3^- (b) and the Se(IV) dimer (c) and (d). In structure c and d, the HSeO_3^- monomers are linked by hydrogen bonds.

RESULTS. The Gibbs energies of two selenite dimers (Fig. 1 c and d) are virtually identical with energy difference of only 0.6 kJ mol^{-1} (slightly favoring structure c). The energy difference is smaller than the hydrogen bond energy, therefore two configurations are likely to coexist and equilibrate. The results of MP2 calculations predict the symmetric and antisymmetric Se–O stretching vibrations of the dimer to appear at 860 and 798 cm^{-1} , respectively (Fig. 2 c and d). No significant difference in the Se–O stretching region between HSeO_3^- and the $(\text{HSeO}_3)_2^{2-}$ dimer is foreseen by MP2. However, two in plane deformation δ -OH vibrations of weak intensity at

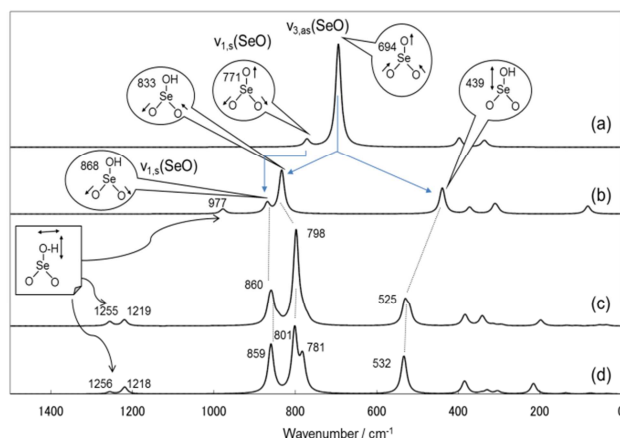


Fig. 2: Theoretical (MP2) IR spectra for SeO_3^{2-} (a), HSeO_3^- (b), Se(IV) dimer (c) and (d).

1255 and 1219 cm^{-1} are envisioned to belong specifically to the dimer (Fig. 2 c and d).

The respective experimental IR spectra are shown in Fig. 3. The symmetric and antisymmetric Se–O stretching vibrations of the dimer are observed at 849 and 820 cm^{-1} , respectively. No significant differences in the experimental spectra (Fig. 3) can be seen with increasing Se(IV) concentrations suggesting a predominance of the dimers already at concentrations above 0.01 mol L^{-1} .

Nevertheless, the weak band observed around 1200 cm^{-1} (Fig. 3) assigned to overlapping δ -OH modes of the dimer prove unambiguously the presence of these species, as expected from MP2 calculations.

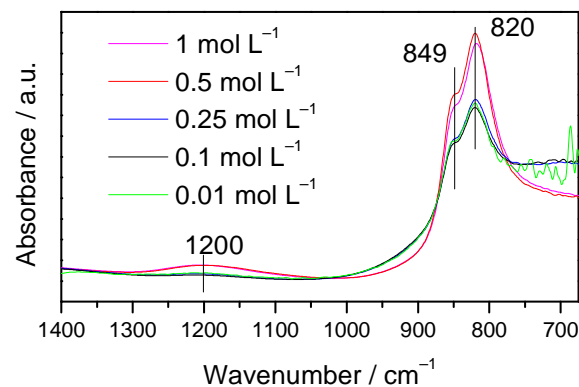


Fig. 3: Normalized IR spectra of solutions of different Se(IV) concentrations, $I = 3 \text{ mol L}^{-1}$, $\text{pH}_c = 5$.

- [1] Olin, A. et al. (2005) *Chemical thermodynamics of selenium*, Elsevier Science Publishers B. V., Amsterdam.
- [2] Torres, J. et al. (2010) *J. Solution Chem.* **39**, 1–10.
- [3] Kretzschmar, J. et al. (2015) *Inorg. Chem.* (submitted).
- [4] Kretzschmar, J. et al. (2015) this report, p. 43

The aqueous speciation of Se(IV): impact of concentration. Part 2: NMR studies

J. Kretzschmar, N. Jordan, E. Brendler,¹ S. Tsushima, C. Franzen, H. Foerstendorf, K. Heim, V. Brendler

¹Institute of Analytical Chemistry, Technical University Bergakademie Freiberg, Freiberg, Germany

The impact of concentration on the selenium(IV) aqueous speciation was systematically investigated by applying Nuclear Magnetic Resonance (NMR) spectroscopy in addition to vibrational spectroscopy and quantum chemical calculations [1]. The dimerization of hydrogen selenite (HSeO_3^-) was confirmed at concentrations above 10 mmol L^{-1} . These results might serve as reference data for aqueous Se speciation as well as for future spectroscopic investigations of the Se sorption processes on mineral phases.

Selenium (Se) is an element being essential for animal and human beings, possessing a narrow difference between the deficient and the toxic level [2]. Furthermore, the radioactive isotope ^{79}Se is a long-lived fission product found in nuclear waste. Due to its half-life of 3.27×10^5 years it is expected to contribute substantially the potential radiation dose of nuclear waste repositories. The spin $\frac{1}{2}$ nucleus of the naturally occurring isotope ^{77}Se is well suited to be directly observed by NMR spectroscopy.

EXPERIMENTAL. NMR measurements were carried out on an Agilent DD2-600 NMR system with a ^{77}Se resonance frequency of 114.5 MHz and using a 10 mm broadband direct detection probe. Selenium chemical shifts are referred to Me_2Se using a coaxial 5 mm tube with 0.5 mol L^{-1} sodium selenate at pH 9.6 in 10% D_2O as external chemical shift reference ($\delta = 1032 \text{ ppm}$ [3]). Samples were prepared at varying Se(IV) concentrations ranging from 1 mmol L^{-1} through 1 mol L^{-1} at pH_c 5, at constant ionic strength of 3 mol L^{-1} (adjusted with NaCl).

RESULTS. According to literature [4] Se(IV) predominates as the hydrogen selenite ion (HSeO_3^-) for dilute solutions in the pH range of 4 to 7. Upon increasing total Se(IV) concentration systematic changes of both the spec-

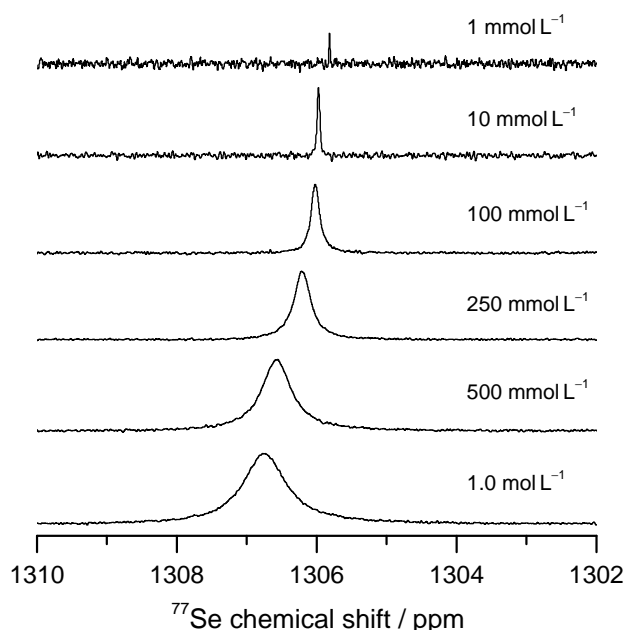


Fig. 1: ^{77}Se NMR spectra of Se(IV) with concentrations as indicated. Spectra are scaled for better visualization.

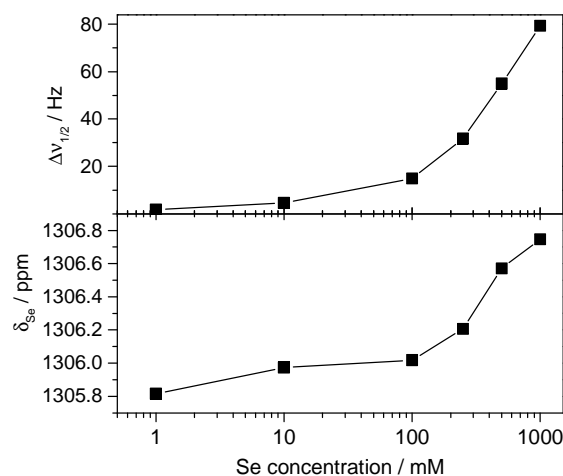


Fig. 2: Dependence of NMR linewidth (top) and chemical shift (bottom) on Se(IV) concentration.

tral parameters selenium chemical shift, δ_{Se} , and NMR linewidth, $\Delta v_{1/2}$, (*i.e.* signal's width at half amplitude) reveal changes in the nature of the Se(IV) speciation. The obtained ^{77}Se NMR spectra and their graphical evaluation can be found in Figs. 1 and 2, respectively. Dimer formation has been postulated at selenium concentrations above $\sim 10 \text{ mmol L}^{-1}$ on the basis of potentiometric titrations [5], but spectroscopic evidence is still lacking. Since other (chemical or spectroscopic) setup based influencing factors could be ruled out [6], the observed spectroscopic changes are attributed to dimerization, yielding the respective hydrogen selenite dimer (HSeO_3^-) $_2^{2-}$. Since monomer and dimer are expected to possess different δ_{Se} and undergo fast chemical exchange, the observed signal is a molar fraction weighted average of these two species. With increasing Se concentration the signal shifts from δ_{Se} of the monomer towards δ_{Se} of the dimer due to a decreasing monomer and concomitant increasing dimer content.

Together with the vibrational spectroscopic results and quantum chemical calculations [1], the existence of the hydrogen selenite dimer could unambiguously be proven. For further aqueous Se(IV) speciation calculations above a critical concentration ($\sim 10 \text{ mmol L}^{-1}$) the dimer has to be considered. This affects both the long-term safety assessment of nuclear waste repositories as well as models for Se migration in some natural environments.

- [1] Jordan, N. et al. (2015) this report, p. 42
- [2] Fernandez-Martinez, A. et al. (2009) *Rev. Environ. Sci. Biotechnol.* **8**, 81–110.
- [3] Koch, W. et al. (1978) *Z. Naturforsch., A: Phys. Sci.* **33**, 1025–1028.
- [4] Olin, A. et al. (2005) *Chemical thermodynamics of selenium*, Elsevier Science Publishers B. V., Amsterdam.
- [5] Torres, J. et al. (2010) *J. Solution Chem.* **39**, 1–10.
- [6] Kretzschmar, J. et al. (2015) *Inorg. Chem.* (submitted).

β -Diketiminato rare earth borohydride complexes: synthesis, structure, and catalytic activity in the ring-opening-polymerization of cyclic esters

M. Schmid, S. M. Guillaume,¹ P. W. Roesky²

¹Institute des Sciences Chimiques de Rennes, Rennes, France; ²Institut für Anorganische Chemie, KIT, Karlsruhe, Germany

A series of β -diketiminato borohydride complexes of di- and trivalent lanthanides (Ln) and Scandium (Sc) [(dipp)₂NacNacLn(BH₄)(THF)₂] ((dipp)₂NacNac = (2,6-C₆H₃Pr₂)NC(Me)CHC(Me)N(2,6-C₆H₃Pr₂); Ln = Sm, Eu and Yb) and [(dipp)₂NacNacLn(BH₄)₂(THF)] (Sc; Ln = Sm, Dy, Yb and Lu) has been synthesized by salt metathesis of [(dipp)₂NacNacK] and the corresponding homoleptic di- and trivalent Ln/Sc borohydrides [Ln(BH₄)₂(THF)₂] (Ln = Sm, Eu and Yb), [Sc(BH₄)₃(THF)₂], and [Ln(BH₄)₃(THF)₃] (Ln = Sm, Dy, Yb and Lu) in THF, respectively (Fig. 1) [1]. The complexes were characterized by single crystal X-ray diffraction. The application of these di- and trivalent metal compounds as initiators in the ring-opening polymerization (ROP) of ϵ -caprolactone (CL) and trimethylene carbonate (TMC) was investigated.

Ionic catalytic systems based on rare earth metals are often employed in a ROP to produce poly(ϵ -caprolactone) and poly(trimethylene carbonate) which have a wide range of biomedical applications due to their biocompatibility and biodegradability. In this study we aim to establish novel catalytic systems based on rare earth borohydrides for the ROP of CL/TMC.

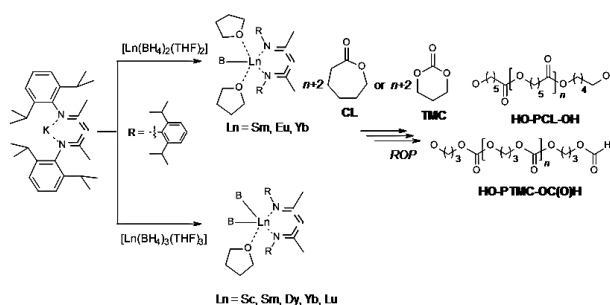


Fig. 1: Synthetic approach to borohydride complexes of di- and trivalent lanthanides and scandium and reaction scheme of the subsequent polymerizations.

EXPERIMENTAL/RESULTS. All manipulations of air-sensitive materials were performed in oxygen- and moisture-free Schlenk-type glassware either on a dual-manifold Schlenkline, or in an argon-filled MBraun or Jacomex glovebox. Tetrahydrofuran was distilled under nitrogen from Na/K alloy benzophenone ketyl prior to use and stored in vacuo over LiAlH₄. Deuterated tetrahydrofuran was obtained from Aldrich Inc. (all 99 atom % D) which was degassed, dried, and stored in vacuo over Na/K alloy. CL (Aldrich) was dried over CaH₂ at least one week prior to distillation. Trimethylene carbonate (1,3-dioxane-2-one, Labso Chimie Fine, Blanquefort, France) was purified by dissolving it in THF, stirring over CaH₂ before being filtered and dried in vacuo, and finally recrystallized from cold THF.

SYNTHESIS OF THE DIVALENT COMPLEXES

[(dipp)₂NacNacLn(BH₄)(THF)₂] (FIG. 2). THF (20 mL) was condensed at -78 °C onto a mixture of [(dipp)₂NacNacK] and [Ln(BH₄)₂(THF)₂] (Ln = Sm (1),

Eu (2), Yb(3)) and the mixture was allowed to warm to room temperature. The resulting green-black (1), yellow (2), or red (3) suspension was stirred at room temperature. The solution was filtered off and concentrated to ca. 10 mL. Storage at -20 °C yielded nearly black (1), yellow (2), or orange (3) prismatic crystals suitable for X-ray analysis.

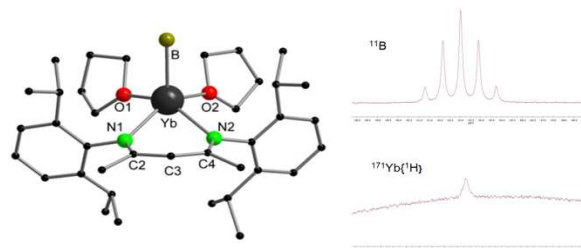


Fig. 2: Crystal structure of the divalent Yb-complex omitting the hydrogen atoms and the corresponding ¹¹B, ¹⁷¹Yb{¹H} spectra.

SYNTHESIS OF THE TRIVALENT COMPLEXES

[(dipp)₂NacNacM(BH₄)₂(THF)] (FIG. 3). THF (20 mL) was condensed at -78 °C onto a mixture of [(dipp)₂NacNacK] and [M(BH₄)₃(THF)_x] (M = Sc (4, x = 2), Sm (5, x = 3), Dy (6, x = 3), Yb (7, x = 3), Lu (8, x = 3)) and the mixture was allowed to warm to room temperature. The resulting orange (4, 5, 8), deep yellow (6), or deep purple (7) suspension was stirred at 60 °C (4), or at room temperature (5–8). The solution was filtered off and concentrated to ca. 10 mL (4) or 5 mL (6, 7, 8). Storage at -20 °C (4, 8), at ambient temperature (6), or at 5 °C (7) yielded colorless (4), yellow prismatic (6), deep purple prismatic (7), or colorless (8) crystals suitable for X-ray analysis.

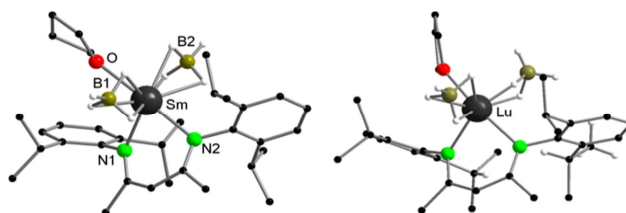


Fig. 3: Crystal structure of the trivalent Sm- and Lu-borohydride complexes omitting the carbon-bound hydrogen atoms.

In both the di- and trivalent compounds, the BH₄[−] groups coordinate in a κ^3 (H) mode to the metal center. Only in the Lu-complex [(dipp)₂NacNacLu(BH₄)₂(THF)] does one BH₄[−] group coordinate in a κ^3 (H) mode, whereas the other one coordinates as κ^2 (H). This kind of mixed κ^2/κ^3 (H) coordination mode is rare. All the complexes were found to afford well-controlled ROPs of CL and TMC.

ACKNOWLEDGEMENTS. M. Schmid thanks the Cusanuswerk, the KHYS (Karlsruhe House of young scientists), and the support program of the Metropole Region of Rennes.

[1] Schmid, M. et al. (2014) *Organometallics* **33**, 5392–5401.

SCIENTIFIC CONTRIBUTIONS (PART IV)

**STRUCTURAL INVESTIGATIONS ON
SOLID SOLUTIONS**

The influence of host cation size and crystal structure on Eu^{3+} substitution in REPO_4

N. Huittinen, Y. Arinicheva,¹ J. Holthausen,¹ S. Neumeier,¹ T. Stumpf

¹Forschungszentrum Jülich, Jülich, Germany

Europium incorporation in rare earth phosphate (REPO_4) ceramics was investigated with site-selective TRIFS. The host cation size of the larger REPO_4 crystallizing in the nine-fold coordinated monazite structure (LaPO_4 - GdPO_4) showed no preference for Eu^{3+} substitution in the crystal lattice, i.e. a complete uptake of the dopant was observed independent of host cation radius. The smaller lanthanides crystallizing in the eight-fold coordinated xenotime structure (TbPO_4 - LuPO_4), however, showed only a weak uptake of the dopant in the ceramic structure.

EXPERIMENTAL. For the synthesis of $\text{REPO}_4:\text{Eu}^{3+}$, rare earth nitrate salts were dissolved in deionized water to a concentration of 0.3–0.5 M. An 85% aqueous solution of H_3PO_4 was slowly added to the solution, causing precipitation of $\text{REPO}_4:\text{Eu}^{3+}$. The precipitate was washed, dried and sintered (5 h, 1450 °C) to obtain a crystalline monazite or xenotime ceramic. The correct composition and solid solution formation of the ceramics were verified with SEM-EDX and XRD, respectively. The site-selective time-resolved laser fluorescence spectroscopic investigations were performed with a pulsed Nd:YAG-pumped tunable optical parametric oscillator. All measurements were performed at cryogenic temperatures (~ 10 K) using excitation wavelengths ranging from 575 to 585 nm, thus, directly exciting the Eu^{3+} ion from the non-degenerate ${}^7\text{F}_0$ ground state to the emitting, non-degenerate ${}^5\text{D}_0$ excited state. Excitation spectra, emission spectra and luminescence lifetimes were collected for all measured samples.

RESULTS. The very narrow excitation spectra of LaPO_4 and GdPO_4 monazites doped with 500 ppm Eu^{3+} (Fig. 1) indicate that Eu^{3+} is fully incorporated on the host cation sites in the highly ordered ceramic materials independent of the ionic radii of the host cations. To investigate the influence of a higher doping on the substitution process, we synthesized mixed $\text{La}_{1-x}\text{Gd}_x\text{PO}_4$ monazites doped with 500 ppm Eu^{3+} (Gd^{3+} serving as a surrogate for Eu^{3+} to avoid potential concentration quenching effects when increasing the Eu^{3+} concentration).

The excitation peak becomes broader when going from

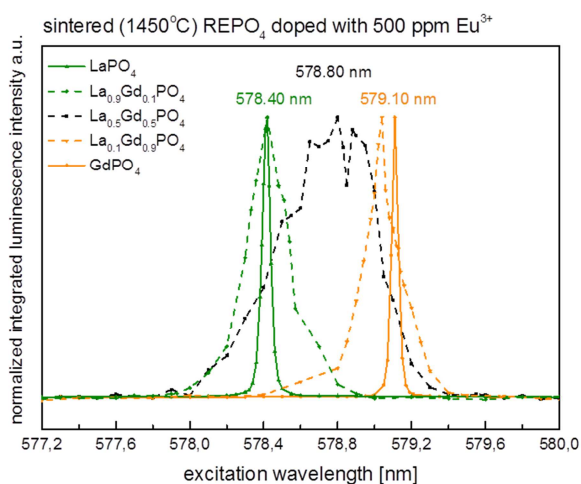


Fig. 1: Excitation spectra of Eu^{3+} -doped LaPO_4 , GdPO_4 , and mixed LaGdPO_4 monazites.

the pure end-members, LaPO_4 and GdPO_4 , toward the $\text{La}_{0.5}\text{Gd}_{0.5}\text{PO}_4$ composition. The emission spectra and luminescence lifetimes, however, do not show any significant change for any of the mixed monazite compositions, indicating that the excitation peak broadening is caused by a local disordering of the monazite crystal structure around the dopant ion, not a bulk phenomenon that would impact the ideality of the monazite solid solutions.

In Eu^{3+} -doped LuPO_4 and $\text{Gd}_{0.5}\text{Lu}_{0.5}\text{PO}_4$ xenotime ceramics the excitation spectra (Fig. 2) show a very broad feature between 575–580 nm along with a peak at 583.00 nm (LuPO_4) and 581.05 nm ($\text{Gd}_{0.5}\text{Lu}_{0.5}\text{PO}_4$).

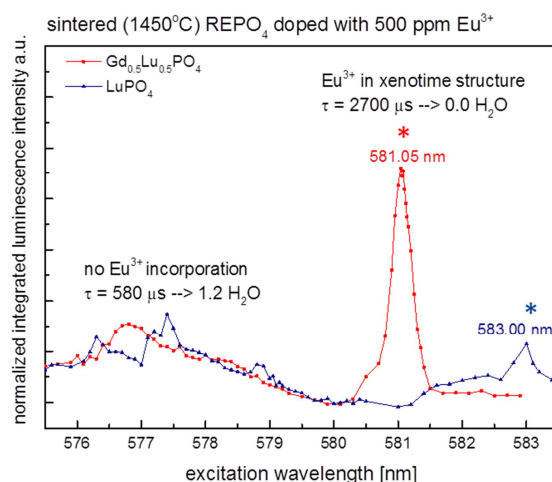


Fig. 2: Excitation spectra of Eu^{3+} -doped LuPO_4 and $\text{Gd}_{0.5}\text{Lu}_{0.5}\text{PO}_4$ xenotime phases.

The broad signal in the shorter wavelength region could be identified as a partly hydrated europium species in the solids, based on luminescence lifetimes. The peaks at 583.00 nm and 581.05 nm (denoted in Fig. 2 with an asterisk) could be assigned to Eu^{3+} substituted within the host cation sites in the xenotime matrix. Even though the relative amount of this incorporated Eu^{3+} species could be increased by increasing the dopant concentration, the hydrated species is still present in the system, pointing towards a non-ideal substitution of the dopant in the xenotime ceramics.

CONCLUSIONS. Rare earth phosphates crystallizing in the monazite structure show promise as potential waste forms for the immobilization of trivalent actinides. The host cation radius does not influence the substitution of the dopant within the host cation sites in the ceramic structure, however, a local disordering can be seen upon increasing the dopant concentration in the materials. The xenotime structure on the other hand is not an ideal host for the larger lanthanide or actinide dopants due to the structure mismatch that does not allow for a complete guest ion substitution within the ceramic structure.

ACKNOWLEDGEMENTS. The authors kindly acknowledge funding from the BMBF (02 NUK 021). N. Baumann, G. Geipel, and M. Schmidt are thanked for valuable help throughout the course of the project.

Determination of the local structure in $\text{La}_{1-x}\text{Eu}_x\text{PO}_4$ solid solutions by EXAFS

M. J. Lozano-Rodriguez, Y. Arinicheva,¹ S. Neumeier,¹ A. C. Scheinost

¹Institute of Energy and Climate Research, Nuclear Waste Management and Reactor Safety (IEK-6), Forschungszentrum Jülich GmbH, Jülich, Germany

Monazite ceramics (LnPO_4 , La-Gd) are promising candidates for the safe storage of nuclear waste. Their low solubility, high chemical flexibility and irradiation resistance makes them especially suited for the enclosure of minor actinides, such as Am and Cm. X-ray absorption spectroscopy was carried out to elucidate the structural changes in $\text{La}_{1-x}\text{Eu}_x\text{PO}_4$ at different ratios of Eu.

EXPERIMENTAL. Solid solutions of $\text{La}_{1-x}\text{Eu}_x\text{PO}_4$ ($x = 0, 0.2, 0.35, 0.5, 0.65, 0.8, 1$) were synthesized as published before [1]. EXAFS measurements were carried out at ROBL (ESRF, Grenoble). The spectra were collected at the La L_1 (6266 eV) and Eu L_3 -edges (6977 eV), using a He cryostat (15 K). Fluorescence or transmission mode data were collected depending on the concentration. The experimental spectra were Fourier transformed using a Hanning window over k -space 2.0 – 9.6 \AA^{-1} for La and 2.0 – 12 \AA^{-1} for Eu. The La and Eu edges were simultaneously refined using the Demeter code [2].

RESULTS. The experimental k^3 -weighted spectra of $\text{La}_{1-x}\text{Eu}_x\text{PO}_4$ ($x = 0, 0.2, 0.35, 0.5, 0.65, 0.8, 1$) and their Fourier Transform magnitudes (FT) are shown in Fig. 1. At both edges, the peaks A, A' correspond to the nine-fold cation-oxygen interaction of the first coordination shell. The peaks B and B' correspond to the nearest phosphate groups and, finally, C and C' correspond to the nearest cation-cation interactions. The Eu local environment as selectively probed by Eu L_3 EXAFS (Fig. 1, right) shows little changes across the whole measurable $\text{La}_{1-x}\text{Eu}_x\text{PO}_4$ solid-solution range; Eu–O distances show a small change across the Eu incorporation, and Eu–(La,Eu) distances decrease monotonously, but with a relatively small slope (Fig. 2). In contrast, the EXAFS spectra at the La L_1 -edge change significantly with increasing Eu content (Fig. 1 left). This change is due to a small decrease of the nearest La–O distances, and a more pronounced one of the nearest La–(La,Eu) distances. The statistically weighted average (La,Eu)–O distances and average (La,Eu)–(La,Eu) distances marked by blue stars in Fig. 2 show a Vegard-like decrease also seen at the long-range order by X-ray diffraction (XRD) [1].

Our results therefore show a very distinct behavior of the Eu and La local environments not detectable by long-range order methods like XRD, which may be at the heart of the structural flexibility of the monazite structure to incorporate a range of different cations.

[1] Ravel, B. et al. (2005) *J. Synchrotron Rad.* **12**, 537–541.

[2] Arinicheva Y. et al. (2014) *Prog. Nucl. Energ.* **72**, 144–148.

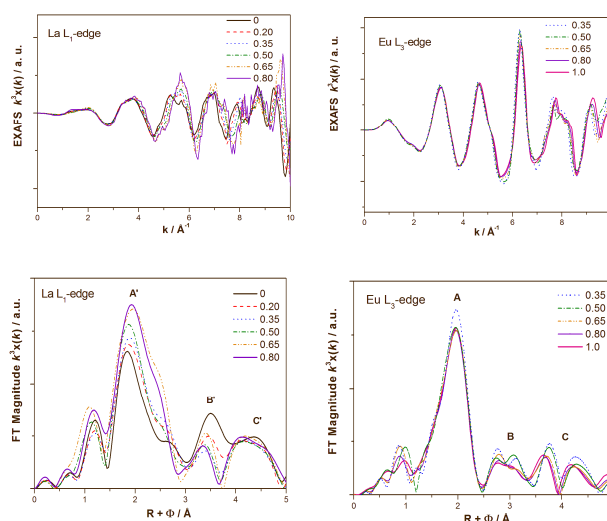


Fig. 1: EXAFS spectra of $\text{La}_{1-x}\text{Eu}_x\text{PO}_4$. (Top) k^3 -weighted spectra collected at Eu L_3 and La L_1 -edges and (Bottom) corresponding Fourier Transforms.

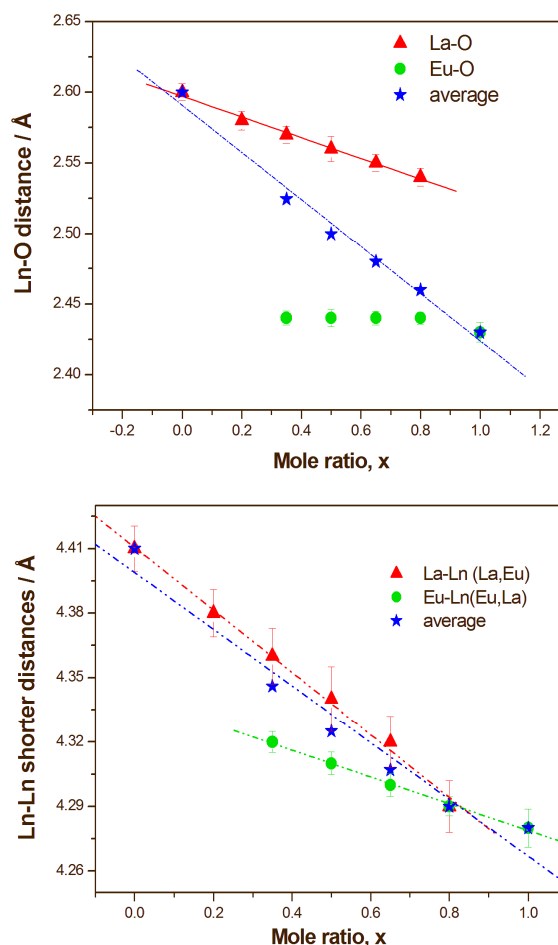


Fig. 2: EXAFS-derived nearest Ln–O and Ln–Ln distances in $\text{La}_{1-x}\text{Eu}_x\text{PO}_4$ plotted as a function of the mole ratio, x .

Structure investigation of $U_xTh_{(1-x)}SiO_4$ solid solutions by EXAFS spectroscopy

C. Hennig, S. Weiss, H. Zänker, S. Labs,¹ H. Curtius,¹ D. Bosbach¹

¹Institute of Energy and Climate Research – Nuclear Waste Management, Forschungszentrum Jülich GmbH, Jülich, Germany

The miscibility behavior of the $USiO_4$ – $ThSiO_4$ system was investigated. The end members and ten solid solutions $U_xTh_{(1-x)}SiO_4$ with $x = 0.12$ – 0.92 were successfully synthesized, without formation of other secondary uranium or thorium phases. Lattice parameters of the solid solutions evidently follow Vegard's Law. Investigation of the local structure with EXAFS reveals small differences between U and Th environments attributed to their different atomic radii but no implications for a miscibility gap [1].

The analysis of the local structure of $Th_{(1-x)}U_xSiO_4$ provides information if the solid solution can be considered as true mixture or if it comprises potentially a miscibility gap. EXAFS spectroscopy is well suited for such analysis because of its element selectivity. The direct coordination of U and Th in $Th_{(1-x)}U_xSiO_4$ does not provide enough information, because the M–O distances depend mainly on the central atom and do not show a significant change with varying x . In contrast, the shortest M–M distance provide more information on the local structure. Half of the $[ThO_8]$ and $[UO_8]$ are directly linked via M–O–M bonds, whereas half of the polyhedra are isolated from each other through $[SiO_4]$ polyhedra (Fig. 1). The M–M distances indicated in Fig. 1 are well suited for an analysis of the local structure in $U_xTh_{(1-x)}SiO_4$.

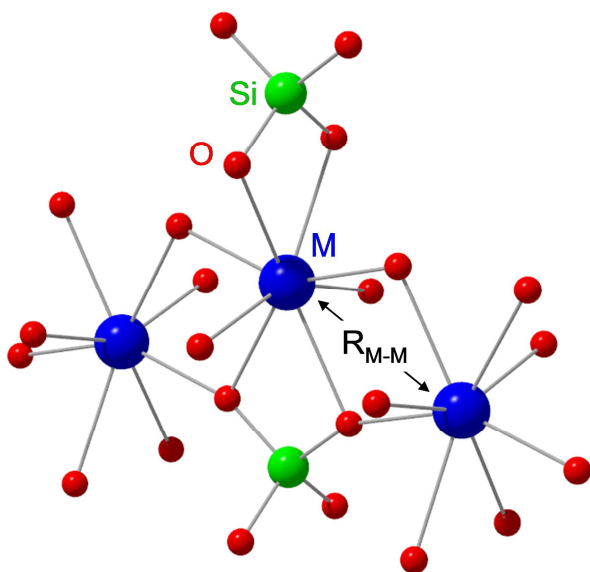


Fig. 1: Schematic drawing of the metal (M) coordination in $U_xTh_{(1-x)}SiO_4$. R_{M-M} represents the three possible distances R_{Th-Th} and R_{Th-U} and R_{U-U} under discussion.

The solid solution comprises three types of these M–M distances, R_{Th-Th} , R_{Th-U} and R_{U-U} . (It should be mentioned that R_{Th-U} and R_{U-Th} are equivalent.) The experimentally determined average distance is given by

$$\bar{R} = \frac{aR_{Th-Th} + bR_{Th-U} + cR_{U-U}}{a + b + c} \quad (1)$$

The diffraction measurement reveals the average distance given by eq. (1), whereas EXAFS reveals only two types of distances: at the Th L_3 absorption edge the distances R_{Th-Th} and R_{Th-U} and at the U L_3 absorption edge the dis-

tances R_{U-U} and R_{U-Th} . R_{Th-Th} is given by the limiting species $ThSiO_4$, R_{U-U} by $USiO_4$. Taking into account only the interaction with the next neighboring metal atoms it is reasonable to assume that $R_{Th-U} \approx (R_{Th-Th} + R_{U-U})/2$. The experimentally determined distances at the Th L_3 absorption edge are

$$\bar{R}_{ThL_3} = \frac{aR_{Th-Th} + bR_{Th-U}}{a + b} \quad (2)$$

In other words, at the Th L_3 absorption edge there is no information on R_{U-U} . In the structure of $U_xTh_{(1-x)}SiO_4$ with $x = 0$, i.e. $ThSiO_4$, exists exclusively distances of R_{Th-Th} , thus, the experimentally determined \bar{R}_{ThL_3} is identical with R_{Th-Th} . For $x \rightarrow 1$ only a small number of Th atoms appear in a dominating environment of U neighbors, thus, $a \rightarrow 0$ and the experimentally determined \bar{R}_{ThL_3} approaches the distance R_{Th-U} . The intermediate \bar{R}_{ThL_3} follow the eq. (2). The distance distribution of \bar{R}_{UL_3} approaches for $x \rightarrow 0$ accordingly the limiting distance R_{U-Th} . Figure 2 shows an approximation of \bar{R}_{ThL_3} and \bar{R}_{UL_3} with Gaussian normal distribution functions. The dashed line adheres to the Vegard line connecting R_{Th-Th} and R_{U-U} . The dotted line represents R_{Th-U} .

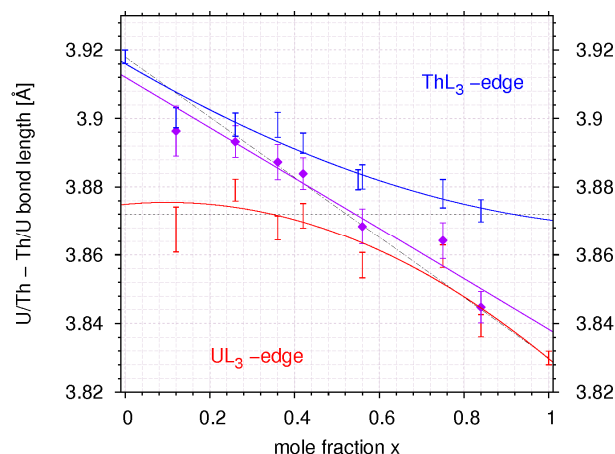


Fig. 2: The metal-metal distances (blue and red) of $U_xTh_{(1-x)}SiO_4$ determined with EXAFS and the weighed averages (purple). The measurements at the U L_3 and Th L_3 absorption edges were performed successively with the same sample.

The data are suitable to discuss whether there exists potentially a miscibility gap and to which extent. The values of \bar{R} are rough indicators for the size of a miscibility gap. The hypothetical case that the system is completely separated into two phases, $ThSiO_4$ and $USiO_4$, could be indicated by EXAFS, because \bar{R}_{ThL_3} would remain equal to R_{Th-Th} for any x and reversed, \bar{R}_{UL_3} would remain equal to R_{U-U} . The distances are expected to follow a linear trend combined with a discontinuity if there is a miscibility gap. The true limiting distances \bar{R} are related with the size of the miscibility gap. Within the experimental error limits, there is no indication of a miscibility gap in the system.

[1] Labs, S. et al. (2014) *Environ. Sci. Technol.* **48**, 854–860.

SCIENTIFIC CONTRIBUTIONS (PART V)

**TRANSPORT PHENOMENA IN
RESOURCE TECHNOLOGY**

Direct observation of waterglass impregnation of fractured salt rock with positron emission tomography

L. Bittner, J. Kulenkampff, M. Gründig, F. Enzmann,¹ J. Lippmann-Pipke

¹Institute for Geosciences, Environmental Mineralogy, Johannes Gutenberg University Mainz, Germany

The injection of waterglass into a sylvinitic core was observed by computed tomography (CT) and positron emission tomography (PET). Significant alterations of the flow field were observed. Further injection of waterglass caused no significant permeability reduction for brine flow. This method provides new insights into impregnation processes of barrier materials.

Impregnation with waterglass (sodium silicate, $\text{Na}_2\text{SiO}_3 + \text{H}_2\text{O}$) is one option of technical improvement of the geological barrier in underground disposal sites, especially in salt rock [1]. The effective sealing depends on a number of factors: the nature of the fractures, the injection velocity, and the reaction kinetics of the injected waterglass with salt and brines, because it polymerizes at a reduction of the pH or in contact with salt. Up to now, only the final results of such impregnations have been tested with destructive methods. We developed a method to observe the waterglass injection process and quantify the resulting modification of transport pathways with the non-destructive techniques μCT and PET [2]. Details on the applied GeoPET-method are given elsewhere [3–5]. Another application in salt rocks is discussed in [6]. In this study, radiolabelled waterglass for sealing the salt core is used and radiolabeled saturated NaCl-solution was applied prior to and after the waterglass injection to verify the seal.

EXPERIMENTAL. The cylindrical sylvinitic core from Staßfurt (Z2KSTh), with a diameter of 100 mm and a length of 150 mm, was strongly fractured by a geomechanical triaxial test. It was characterized with high-resolution μCT , yielding a system of two converging fractures with a total porosity of 6.38%. Saturated sodium chloride solution with sediment and sodium waterglass was applied as injection test fluid and impregnation agent, respectively. The injection study with PET-observation consists of five steps (Tab. 1). First, a saturated NaCl-solution labelled with $[^{18}\text{F}]\text{KF}$ with an activity of 100 MBq was injected in order to visualize the effective flow paths of the brine and quantify the permeability of the core. Second, waterglass solution labelled with $[^{18}\text{F}]\text{KF}$ was injected into the wet core. As a third step, again saturated NaCl-solution with $[^{18}\text{F}]\text{KF}$ was injected for direct comparison with the initial brine flow experiment. The latter two steps were repeated after flushing the core with pressured air.

The duration of each injection step was 1–2 hours, at least 3 days were left between the steps for decay and equilibration. The entry pressure was limited to 5 bars for technical reasons in this feasibility study.

Tab. 1: Parameters of the five individual measurements.

No.	p_{max} (bar)	flow (mL/min)	V_{inj}	fluid
1	0.3	0.25	const. flow	NaCl-brine
2	2.6	0.25; 0.5	7 mL	waterglass
3	1.0	0.25; 0.1	const. flow	NaCl-brine
4	5.0	5; 0.1; 0.05; 0.01	9 mL	waterglass
5	1.0	0.25	const. flow	NaCl-brine

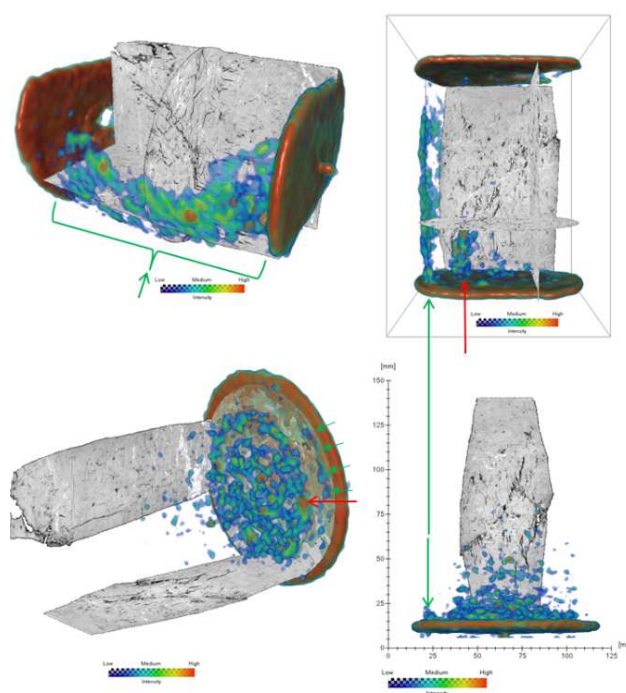


Fig. 1: PET (coloured) overlay with CT (grey). Influx of brine (top), Inflow of waterglass (bottom); green arrows mark the flux into the superficial structure and red arrows into the central volume.

RESULTS. The sequential PET images show the propagation of these fluids through the core which allows the derivation of the local velocities and the topology of the effective pathways. From the comparison of time series of PET with the μCT data the effective volume, which is the portion of the void volume affected by the process, can be derived.

In spite of the relatively low entry pressure we could observe significant alterations of the flow field, although the achievable depth of penetration and thus the achievable permeability reduction was insufficient for practical applications. Actually, the crucial effect was the elimination of primary superficial flow after the first injection of waterglass. The further injection of a significant quantity of waterglass caused no severe permeability reduction for brine flow. The pressure range can be extended, and the method is ready for studying and evaluating impregnation processes, also with other barrier materials and sealing agents.

ACKNOWLEDGEMENT. This work was funded by the German Federal Ministry of Economics and Technology (BMWi), project agency PTKA-WTE, contract no. 02 E 10176

- [1] Bollingerfer, W. et al. (2011) *Vergütung der Auflockerungszone im Salinar (VerA)*, Abschlussbericht DBE Technology GmbH.
- [2] Bittner et al. (2014) International Conference on the Performance of Engineered Barriers: Backfill, Plugs & Seals, February 06–07, 2014, Hannover, Germany.
- [3] Gründig, M. et al. (2007) *Appl Geochem.* **22**, 2334–2343.
- [4] Kulenkampff, J. et al. (2008) *Phys. Chem. Earth* **33**, 937–942.
- [5] Richter, M. et al. (2005) *Radiochim. Acta.* **93**, 643–651
- [6] Wolf, M. (2011) PhD Thesis, Universität Leipzig, Leipzig, Germany.

Highly effective radiolabeling of commercial TiO₂ nanopowder as a tool for sensitive nanoparticle detection

H. Hildebrand, S. Schymura, U. Holzwarth,¹ N. Gibson,¹ M. Dalmiglio,¹ K. Franke

¹European Commission Joint Research Centre, Ispra, Italy

Detection and quantification of engineered nanoparticles (NPs) in complex (environmental) media is still a challenge because their concentrations are expected to be low compared to elemental background levels. This study presents three different options for radiolabeling of commercial TiO₂-NP (AEROXIDE® P25, Evonik Industries, d_p = 21 nm) for particle detection, localization and tracking under various experimental conditions. The radiolabeling procedures ensure high efficiency, stability and consistency of important particle properties such as size and morphology. Concentrations of TiO₂-NPs as low as 0.5 ng/L could be detected for the first time.

EXPERIMENTAL. Radiolabeling via in-diffusion of ^{44,45}Ti radionuclides was slightly modified according to [1] by adding about 1 kBq of [⁴⁴Ti]TiCl₄ aqueous stock solution to 5 mg powdered TiO₂-NPs. To test higher specific activities, up to 180 MBq of [⁴⁵Ti]TiCl₄ was added to 1 mg TiO₂-NPs. Low temperature annealing of the mixtures was conducted at 180 °C for 2 hours until the sample was completely dry. In the next step, the powder was cooled to room temperature and radiolabeled TiO₂-NPs were dispersed in ultrapure water by sonication for 10 min and afterwards centrifuged to separate NPs from supernatant. This washing procedure was conducted three times to remove unbound ⁴⁴Ti or ⁴⁵Ti, respectively. Proton irradiation of TiO₂ nanopowder was conducted using a cyclotron (Scanditronics MC 40) and the nuclear reaction ⁴⁸Ti(p,n)⁴⁸V which leads to recoil implantation of ⁴⁸V radionuclides in TiO₂-NPs. Details on the target system and irradiation capsules were previously described by Abbas et al. [2]. The third radiolabeling method was based on the nuclear reaction ⁷Li(p,n)⁷Be. For radiolabeling of TiO₂-NPs, LiH salt was carefully mixed with TiO₂-NPs in a predefined mass ratio (LiH/TiO₂ ≈ 0.5) and proton irradiation of the LiH/TiO₂ mixture was conducted [3]. After radiolabeling, several washing steps were applied to remove LiH from the [⁷Be]TiO₂-NP.

RESULTS. Three different methods were tested for radiolabeling of TiO₂-NP. All three methods proved to be successful and lead to reasonable activity concentrations and, thereby, very low detection limits (see Tab. 1). In all cases, size and morphology of the radiolabeled NPs were comparable to the original NPs. This was proven by dynamic light scattering methods and SEM measurements (Fig. 1). Radiolabeling stability was tested in aqueous NP suspensions under different pH conditions. It could be

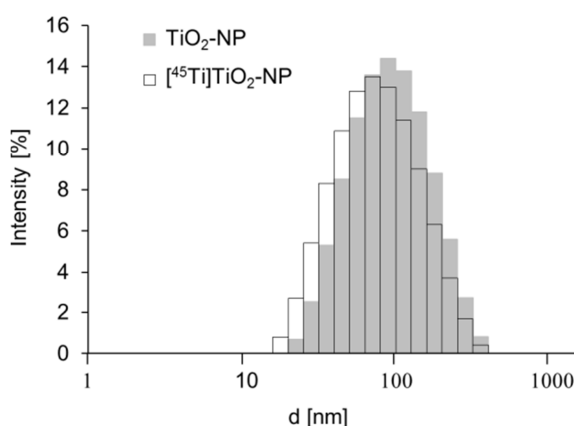


Fig. 1: Particle size distribution by intensity of Na₆P₆O₁₈-stabilized TiO₂-NP dispersions (c_{NP} = 100 mg/L, c(Na₆P₆O₁₈) = 0.1 %), original TiO₂-NPs (grey histogram), [⁴⁵Ti]TiO₂-NPs (white histogram).

shown that all radiolabeled NPs are stable under environmentally relevant conditions (pH 5.5 to pH 8) for at least 7 days. In case of [⁴⁴Ti]TiO₂, a new radiolabeling method was developed that allows radiolabeling without the necessity of a cyclotron. Furthermore, it has to be pointed out that isotopic labeling might be quite interesting and necessary in many studies where chemical purity of the NPs is important.

Direct activation and recoil labeling was conducted using a cyclotron and special target setups. These radiolabeling procedures offer quite interesting options in terms of radiolabel half-life and also detection limits in the low ng/L range. Direct activation seems to be the best option in case of cyclotron availability, whereby recoil labeling is maybe more interesting for other nanomaterials [3]. The very low detection limits reached are unrevealed with conventional detection methods so far. Furthermore, no extensive sample preparation, processing, or purification is necessary. This means that radiolabeled TiO₂ NP can be traced and localized within very complex systems such as (waste-)water, sediments, soils, or tissue without disturbing the sample structure.

ACKNOWLEDGEMENTS. This study was financially supported by the German Federal Ministry of Education and Research within the NanoNature initiative (project NanoTrack, support code: 03X0078A) and QualityNano Transnational Access (support codes JRC-TAF-13 and JRC-TAF-119).

- [1] Butz, T. (2012) *Radiochim. Acta* **100**,147–153.
 [2] Abbas, K. et al. (2010) *J. Nanopart. Res.* **12**, 2435–2443.
 [3] Holzwarth, U. et al. (2014) *J. Nanopart. Res.* **16**, 2574.

Tab. 1: Comparison of the radiolabeling procedures and the resulting radiolabeled TiO₂-NP. Detection limits were determined using batch vessels with aqueous NP suspensions (V = 20 mL), a gamma counter and measurement times of 5 min.

Radiolabeling procedure	NP obtained	t _{1/2}	Detection limit (ng/L)
In-Diffusion	[⁴⁴ Ti]TiO ₂	60.4 a	5000
	[⁴⁵ Ti]TiO ₂	3.08 h	0.5
Direct Activation	[⁴⁸ V]TiO ₂	15.97 d	14
Recoil Labeling	[⁷ Be]TiO ₂	53.29 d	17

Dynamics of metal-humate complexation equilibria: isotope exchange studies substantiate stabilization processes

H. Lippold

Complexation with dissolved humic matter can be crucial in controlling the mobility of higher-valent contaminant metals such as actinides, which are otherwise strongly adsorbed to mineral surfaces. For transport modelling, all involved interactions are presumed to be dynamic equilibrium processes where association and dissociation run permanently. For metal-humate complexes, however, there are indications of a growing resistance to dissociation over time [1–3], away from reversibility. In this study, the isotope exchange principle was employed to gain direct insight into the dynamics of the complexation equilibrium including kinetic stabilization phenomena.

EXPERIMENTAL. The experimental conception is illustrated in Fig. 1. Purified humic acid (HA, 500 mg L⁻¹ in 0.1 M NaClO₄, pH 4.0) was contacted with the REE Tb(III) (M) as an analogue of trivalent actinides. Deviating from the procedure applied in a previous study [4], the radioisotope ¹⁶⁰Tb (1 nM) was introduced first, and non-radioactive ¹⁵⁹Tb (2 mM) was added subsequently after different times of pre-equilibration (t_1). At this high metal load, flocculation of humic colloids generates a solid-liquid system where adsorbed amounts of ¹⁶⁰Tb can be determined by radiometric analysis of the supernatant after centrifugation. Owing to the curvature of the adsorption isotherm, the bound fraction of total Tb is lower after adding the large amount of ¹⁵⁹Tb (saturation of HA). Consequently, in a dynamic equilibrium the radioisotope is expected to be partly desorbed to adapt the solid-liquid distribution of total Tb. For equilibration, the solutions (4 mL) were rotated end-over-end, admitting different time periods (t_2).



Fig. 1: Experimental approach for investigating the dynamics of metal-humate complexation, considering possible ageing effects (M: metal, M*: radioisotope, HA: humic acid).

RESULTS. As reported previously [4], isotope exchange proceeds very fast if the radioisotope ¹⁶⁰Tb is contacted with HA that has been saturated with non-radioactive ¹⁵⁹Tb. Stabilization processes were not observed. Reversing the sequence of introducing the isotopes leads to completely different results, as it can be seen in Fig. 2. Here, M* stands for “radiolabelled Tb” since the added quantity of 1 nM does not entirely consist of ¹⁶⁰Tb. At this concentration, only the strongest binding sites are occupied. By introducing the excess amount of non-radioactive Tb, an exchange is initiated, striving towards the equilibrium state (Fig. 2a). The dynamic character of this equilibrium is thereby proven. However, the rate of exchange is much lower than in the reverse procedure. Most notably, it depends on the time of pre-equilibration with M*, i.e., stabilization processes are in fact existent. Obviously, they are confined to the most reactive sites. The time-dependent progress of this stabilization can be better seen in Fig. 2b, where adsorbed amounts of M* af-

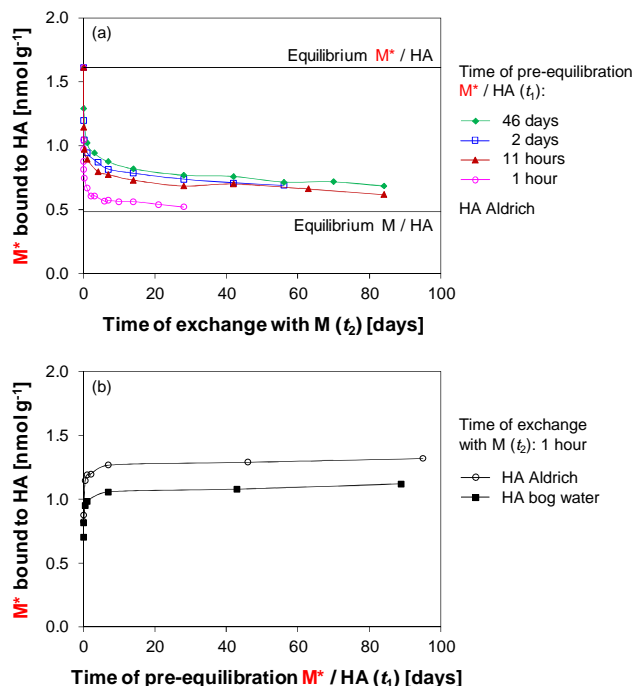


Fig. 2: Amount of radiolabelled Tb bound to HA after saturating with non-labelled Tb, shown as a function of exchange time for different pre-equilibration times (a) and as a function of pre-equilibration time for a fixed exchange time of 1 hour (b).

ter a fixed time of exchange are plotted vs. pre-equilibration time for two different humic materials. Changes are most pronounced in the first days, followed by a very minor trend over an extended time period. For longer pre-equilibration times, the kinetics of stabilization does not interfere with the kinetics of exchange. However, fitting the data for the 46 days period in Fig. 2a, according to first-order exchange kinetics, is only possible if at least two components with different rate constants are assumed. This means that the very small fraction of sites occupied by M* is still only partly affected by the slow exchange kinetics. Nonetheless, the present findings are relevant since just such extremely low metal loads are to be considered. Even though it takes up to 2 years until equilibrium is attained, metal exchange between humic carriers and mineral surfaces cannot be neglected in transport models on the long time scale.

ACKNOWLEDGEMENT. This work was funded by the German Federal Ministry for Economic Affairs and Energy (BMWi), project agency PTKA-WTE, support code 02 E 10971.

- [1] Artinger, R. et al. (1998) *J. Contam. Hydrol.* **35**, 261–275.
- [2] King, S. J. et al. (2001) *Phys. Chem. Chem. Phys.* **3**, 2080–2085.
- [3] Geckeis, H. et al. (2002) *Environ. Sci. Technol.* **36**, 2946–2952.
- [4] Lippold, H. (2013) *Report HZDR-048*, p. 25.

Transport system for solid targets of the COSTIS-system mounted at the beam transfer line (BTL) of the Cyclone 18/9

K. Franke, J. Hauser¹

¹Helmholtz-Zentrum Dresden – Rossendorf, Department of Research Technology, Dresden, Germany

The COSTIS system is a commercially available target station for the irradiation of solid targets by means of a cyclotron. Up to three targets can be provided for irradiation by a slot system. In standard setup the target can be ejected via a pneumatically driven piston system. The target is then allowed to drop down into an open lead container, which can be closed remotely afterwards. The described procedure is well established and reliable. But the concept is limited to low dose targets and environments. The required entering of the cyclotron vault for manual pick up of the container at the cyclotron and the light 20 mm Pb shielding of the container itself cause exposure risk for the personnel after long term irradiations with highly activated cyclotron parts and target.

The purpose of this work was the design of an alternative for the pickup and the transport of irradiated targets to minimize the radiation dosage of the personnel during manual handling of the COSTIS-lead-container.

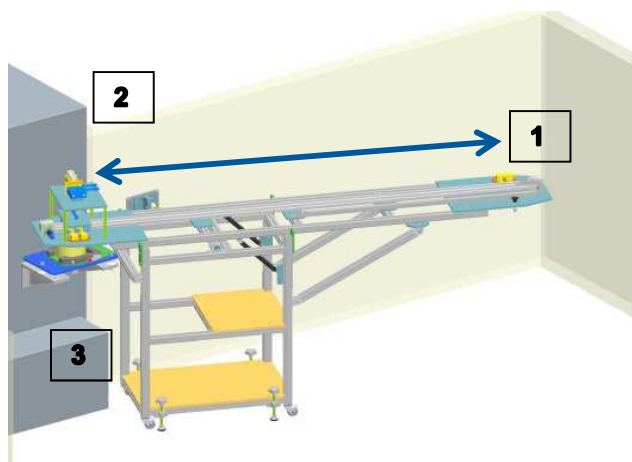


Fig. 1: Transport system (1: target ejection position; 2: loading station; 3: vault door).

PRINCIPLE. The new designed transport system (Fig. 1) still uses the software controlled target ejection function of the COSTIS-system. With ejection the target capsule is allowed to fall into a PTFE-container. To assure a safe target drop into the PTFE-container, the gap between the target guiding plate and the PTFE-container is smaller than $d/2$ of the target capsule. After target ejection the PTFE-container can be transferred remotely from target ejection position (1) to the loading station (2) with a target slide. The loading station allows the transfer of the PTFE-container remotely into a Pb-container (60 mm Pb).

Now the vault door is used as carrier of the Pb-container from inside the vault to the anteroom. For this purpose a proper fixture for the Pb-container is mounted at the inner side of the vault door and via opening the vault door the container is safely transported out of the vault. Once outside, the container is manually closed with a lid and transferred to a trolley for further handling. Due to positioning of the container at a certain altitude and due to the deep positioning of the target coin inside of the container, the manual closing of the container does not cause significant

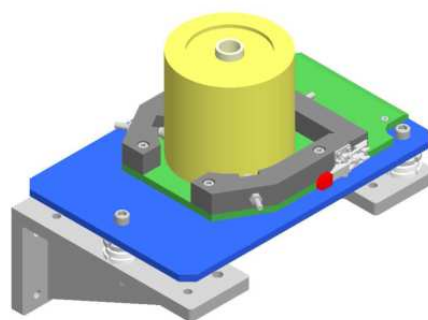


Fig. 2: COSTIS-lead-container positioned in the door holder (Yellow: Pb-container, white: PTFE-container).

dosage. A more complicated automatic closing system is not mandatory.

Subsequent target transfers can follow up without entering the vault once another empty lead container is positioned in the door holder and the vault door is closed. A new PTFE-container is transferred remotely from a magazine onto the target slide, which again is remotely positioned at target ejection position. The magazine of PTFE-containers holds two replacements in accordance with the maximal capacity of the three target slots of the COSTIS station. The remote system of the transport unit uses redundant feedback signals for a reliable and safe operation.

RESULTS. The newly implemented transport system allows a significant reduction of the radiation dose during pickup and transport of the irradiated solid targets. No entering of the vault is needed after irradiation. The system is highly reliable due to its redundant and straightforward design (2-fold position switches and photoelectric barriers). Due to fixed attachment points in the vault and at the BTL the mobile unit can be easily removed or mounted. The system is maintenance free and all parts easy accessible.



Fig. 3: COSTIS-lead-container placed on the container carrier.

For further handling of the targets lead containers were designed to fit in the transfer locks of hot cells. The transfer can be carried out directly from the trolley. Container lid and PTFE-container are suited for manipulator handling in hot cells.

SCIENTIFIC CONTRIBUTIONS (PART VI)

**NUCLEAR REACTOR
SAFETY RESEARCH**

Modeling of the OECD/NEA large SFR core with Serpent-DYN3D and Serpent-PARCS code sequences

E. Nikitin, E. Fridman, K. Mikityuk¹

¹Paul Scherrer Institut, Villigen, Switzerland

In this study, the Serpent Monte Carlo code was used as a tool for preparation of homogenized group constants for the nodal diffusion analysis of a large U-Pu MOX fueled Sodium-cooled Fast Reactor (SFR) core specified in the OECD/WPRS neutronic SFR benchmark. The group constants generated by Serpent were employed by DYN3D and PARCS nodal diffusion codes in 3D full core calculations. The DYN3D and PARCS results were verified against the references full core Serpent Monte Carlo solution. A good agreement between the reference Monte Carlo and nodal diffusion results was observed demonstrating the feasibility of using Serpent as a group constant generator for the deterministic SFR analysis.

This study presents the solution of the OECD/NEA neutronic Sodium-cooled Fast Reactor (SFR) benchmark [1] with nodal diffusion codes. The homogenized few-group constants were generated with a Monte Carlo code called Serpent [2], and these were used as an input in the nodal diffusion calculations performed with the deterministic core simulators DYN3D [3] and PARCS [4]. The study concentrates on the beginning of cycle and from the expected results of the benchmark the following parameters were evaluated: core multiplication factor (k -eff), effective delayed neutron fraction (β -eff), Doppler constant (K_D), sodium void worth ($\Delta\rho_{Na}$), total control rod (CR) worth ($\Delta\rho_{CR}$), and radial power distribution.

DESCRIPTION OF THE REFERENCE CORE. For the benchmark the large 3600 MWth SFR core with U-Pu mixed oxide (MOX) fuel was chosen [1]. It is a 3D core which radially contains two fuel zones, surrounded by the radial reflector sub-assemblies. The Pu content of MOX fuel material is varied axially and also differs in the radial zones. The fuel pellets in the fuel rods are axially bonded with helium gas plenums and reflector pellets as from below, so from above. Furthermore two independent control sub-assemblies – one with natural and the other with enriched B4C pins – are included in the core, and in nominal state the bottom of the CRs is located at the top of the active core. More detailed description of the reference core is given in the benchmark specification [1].

Tab. 1: Comparison of the core integral parameters.

	Serpent*	DYN3D	PARCS	Difference, pcm	
				Serpent vs DYN3D	Serpent vs PARCS
k -eff	1.01070	1.00940	1.00984	-128	-84
β -eff, pcm	358	356	356	-2	-2
K_D , pcm	-852	-867	-868	-15	-15
$\Delta\rho_{Na}$, pcm	1864	1951	1945	87	81
$\Delta\rho_{CR}$, pcm	-6046	-6173	-6227	-127	-180

*: Standard deviation of k -eff = 2 pcm.

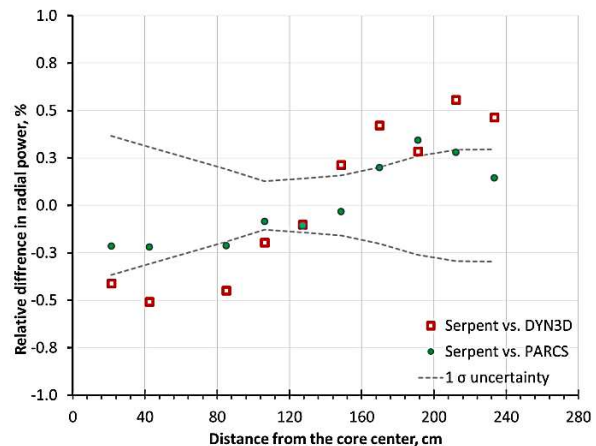


Fig. 1: Relative difference in radial power.

GENERATION OF THE HOMOGENIZED GROUP CONSTANTS. The homogenized group constants for all components of the reference SFR core were produced by Serpent. For fuel regions not facing radial reflector the group constants were calculated using a 3D single sub-assembly model with reflective radial and black axial boundary conditions. Because of the non-negligible spectral effect the homogenized parameters for outermost fuel sub-assemblies were generated using 3D fuel-reflector models. For all non-multiplying regions the group constants were prepared using 2D super-cell models. More details can be found in [5].

RESULTS. The nodal diffusion results are compared with the full core Serpent solutions. The calculated core integral parameters can be seen in Tab. 1, where nodal diffusion results show generally good agreement between deterministic and MC solutions. The k -eff is slightly underestimated by DYN3D and PARCS. The β -eff and K_D values agree within few pcm. Both core simulators overestimate the $\Delta\rho_N$ by about 80 pcm while predict somewhat higher CR worth. The comparison of the core radial power distribution was made on the main diagonal and the evaluated results are presented in Fig. 1. The Serpent-DYN3D and Serpent-PARCS results are in a very good agreement with the reference MC solution.

CONCLUSIONS. The results of the study demonstrate the feasibility of using Serpent as a group constant generator for the deterministic SFR analysis.

[1] Blanchet, D. et al. (2011) *AEN – WPRS Sodium Fast Reactor Core Definitions (version 1.2)*, OECD/NEA.
 [2] Leppänen, J. (2013) *Serpent – a Continuous-energy Monte Carlo Reactor Physics Burnup Calculation Code*. <http://montecarlo.vtt.fi/>.
 [3] Grundmann, U. et al. (2000) *Proc. PHYSOR 2000*, Pittsburgh, USA.
 [4] Downar, T.J. et al. (2010) *PARCS v3.0 – U.S. NRC Core Neutronics Simulator*, Theory Manual, Ann Arbor, MI.
 [5] Nikitin, E. et al. (2015). *Solution of the OECD/NEA neutronic SFR benchmark with Serpent-DYN3D and Serpent-PARCS code system*, Ann. Nucl. Energy. 75, 492–497.

Study of the impact from small shifts of fuel assemblies on the ex-core neutron flux

J. Konheiser, C. Brachem,¹ M. Seidl²

¹Institute of Power Engineering, Technische Universität Dresden, Dresden, Germany; ²E.ON Kernkraft GmbH, Hannover, Germany

Variation of fuel assembly positions in the outer region of the core were studied, which were directly opposite to the ex-core instrumentation. An increase of the neutron flux at the chambers of up to 4% has been calculated for a change in position of 1 mm between some fuel assemblies. The reason is an improved moderation of neutrons because of the larger water gap. This causes an increase in local power which leads to a greater leakage of neutrons over the core barrel. In addition, a dependence of this effect was found as a function of cycle time.

The fuel assembly pitch in a Pressurized Water Reactor (PWR) is slightly larger than necessary to enable a good loading respectively unloading of the reactor core and to take thermal expansion. Therefore, small movements of the fuel assemblies are possible in the core during operation cycle and leads to varying water gaps. These can occur between the fuel assemblies or between the fuel assemblies and the core baffle. The local fuel to moderator ratio is changed and it induces small local variations in the power. These variations in the periphery of the reactor core can influence the neutron flux at the ex-core instrumentation. The focus of the present work was to quantitatively predict the implications of these pitch variations. The Monte Carlo code MCNP [1] was used for the calculations. Figure 1 shows a calculated case with the expanding water gap between the separate fuel assemblies and the remainder of the core. The fluxes in the instrumentation were determined in two steps. The behavior of the core was investigated on the basis of critical calculations in the first step. In the second step, the neutron fluxes in the ex-core instrumentation were determined.

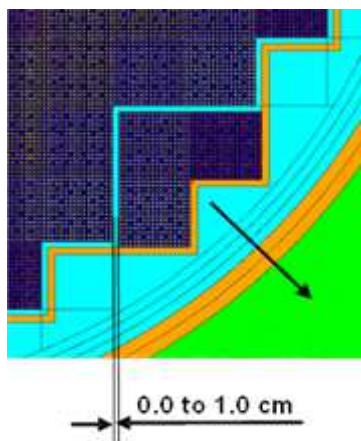


Fig. 1: The expanding water distance inside of the reactor core.

CRITICAL CALCULATION. The complete core up to the reactor pressure vessel was modeled for critical calculations. The model had 193 fuel assemblies with 256 fuel rods correspond the fuel layout for a German Vor-Konvoi type PWR. The material data have been taken from the burn-up and power distribution calculations. Burnup distributions of the core were used from the start and end of cycle for the critical calculations.

The calculations primarily served for the calculated neutron fluxes at the outer surface of the barrel. The results were used for the generation of surface sources for the transport calculations. The analysis of sources shows a

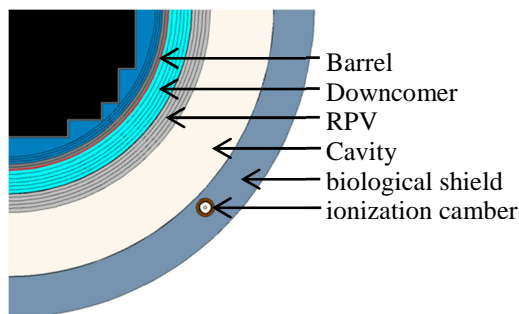


Fig. 2: Horizontal cut of the calculation model for positions of the ionization chambers.

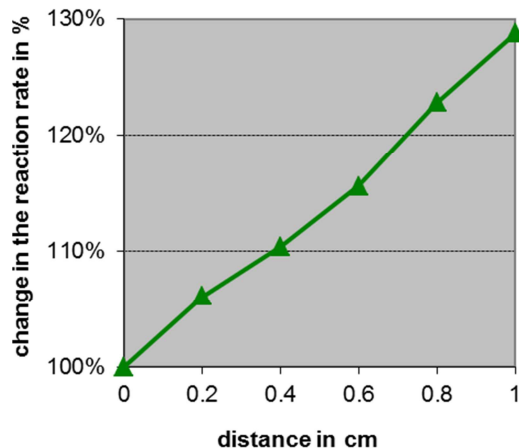


Fig. 3: The change of reaction rate of the ex-core instrumentation as a function of distance between core and move fuel assemblies.

clear increase of the flux with growing distance (up to 40%). The reason is a hotspot of fission. It is generated at the water and has a direct impact on the flux in the core barrel. This effect is at the end of the cycle at the greatest. Accordingly, the transport calculations were performed with this source.

TRANSFER CALCULATION. Figure 2 shows a horizontal cut of the model. The ex-core instrumentation is located in the biological shield. Figure 3 shows the change of (n, α) reaction rate of boron of the ionization chambers of the ex-core instrumentation. The reaction rate at the positions could change for up to 30%. The calculations show, that the ionization chambers practically see only the core region, which lies directly in their field of view. Therefore, local changes in core dimension in this region have a considerable influence on the counting rate of the chamber.

CONCLUSION. Variations of fuel assembly pitches could produce the signal amplitudes approximately 30% in the ex-core instrumentation. The reason is an increase in local power of a fuel assembly. Also, a dependence on cycle time could be determined. The maximum effect was observed at the end of cycle.

ACKNOWLEDGEMENT. This work was supported by E.ON Kernkraft GmbH.

[1] Kiedrowski, B. et al. (2010) *MCNP5-1.60 Feature Enhancements and Manual Clarifications*, LA-UR-10-06217.

Simulation of a boron dilution transient scenario in a PWR modeling coupled neutron kinetics, thermal hydraulics, and fuel rod behavior by the code system DYN3D-TRANSURANUS

U. Rohde, L. Holt, S. Kliem

Recently the reactor dynamics code DYN3D was coupled to the fuel performance code TRANSURANUS. The code system DYN3D-TRANSURANUS applies a general TRANSURANUS coupling interface [1], hence, it can be used as either one-way or two-way coupling approach. The coupled code system was applied for the simulation of a boron dilution transient in a PWR reactor. Applying the more advanced two-way coupling approach, much higher fuel rod cladding temperatures were achieved at locally resolved level due to the occurrence of heat transfer crisis. This emphasizes the importance of advanced simulations for reliable estimation of reactor safety.

SCENARIO DESCRIPTION AND MODELING. The accident scenario analysis was performed for a German Konvoi type Pressurized Water Reactor with a nominal thermal power of 3750 MW. The reactor is assumed to be at sub-critical shut down state after a steam generator tube break incident. In the course of this scenario, the coolant pressure in the primary circuit will arrive at a lower level than pressure at the secondary side of the steam generator. Hence, un-borated feedwater can penetrate from the secondary to the primary side in the affected loop. If then the main coolant circulation pump is switched on erroneously, the un-borated water will be transported to the reactor core. On the way to the core it is mixed with highly borated water in the reactor pressure vessel. The lower boron concentration in the mixed coolant leads to a positive reactivity insertion into the core, which over-compensates the initial sub-criticality and induces a sharp rise of reactor power. This power rise will then be compensated by negative reactivity feedback.

The neutron kinetics and thermal hydraulics in the core are modeled by the 3D reactor dynamics code DYN3D [2]. The fuel rod behavior is described in detail by the TRANSURANUS code [3], whereas DYN3D adopts its own simplified fuel behavior model in parallel in the one-way approach. Both one-way and two-way DYN3D-TRANSURANUS code coupling approaches were applied. In both approaches, the nuclear power density and thermal hydraulic conditions at the cladding surface are transferred from DYN3D to TRANSURANUS, whereas in the two-way approach the fuel and cladding temperatures additionally obtained by TRANSURANUS are transferred back to DYN3D. As input for boron concentration at each fuel assembly inlet, measured values from the Rossendorf Coolant Mixing Model facility were used [4].

RESULTS OF THE ANALYSIS. The maximum reactivity introduced by the boron dilution achieves 2.11 \$ (one-way approach) and 2.07 \$ (two-way approach) resulting in a super-prompt critical power excursion. The maximum peak power reaches 32090 MW (one-way approach) and 32144 MW (two-way approach). The differences in the average reactor parameters like reactivity and power are almost negligible. The picture will change if we look for local parameters in single nodes of the fuel assemblies. Figure 1 shows the differences in node surface

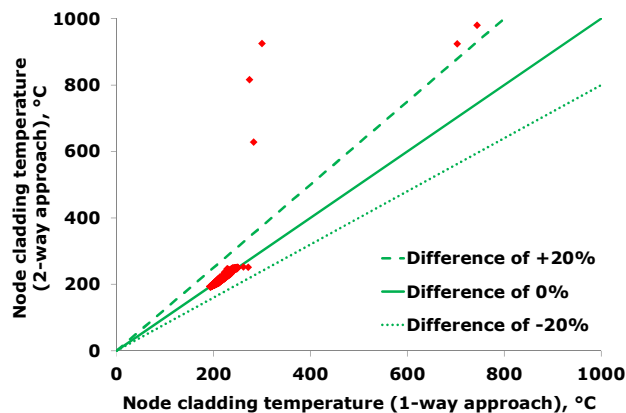


Fig. 1: Node surface cladding temperature in the two-way approach versus one-way approach.

cladding temperatures between one-way and two-way approach. In this calculation, the calculated critical heat flux value was conservatively increased by a factor of two. In five nodes we observe cladding temperatures much higher than 350 °C indicating post-crisis heat transfer conditions (film boiling). In three of these nodes film boiling occurs only in the two-way approach calculation. These differences can be mainly explained by feedback from TRANSURANUS cladding temperatures to thermal hydraulics which is taken into account only in the two-way approach. Heat transfer coefficient in the gas gap changes with burn-up and fuel rod enthalpy. This can be correctly modeled only by the help of detailed fuel performance codes like TRANSURANUS. For example, according to the node with the highest surface cladding temperature in Fig. 1, a higher heat transfer coefficient in the gap was calculated by TRANSURANUS leading to a higher heat flux, and therefore, to earlier exceedance of the critical heat flux in the two-way approach. That means, the one-way coupling approach can produce non-conservative results with respect to safety assessment for cladding temperature. An advanced coupling between neutron kinetics, thermal hydraulics and detailed fuel behavior modeling is required for reliable safety analysis.

ACKNOWLEDGEMENTS. This project was funded by E.ON Kernkraft GmbH within the knowledge preservation program in the German nuclear safety research.

- [1] Holt, L. et al. (2015) *Annals of Nuclear Energy, Special Issue on LWR Multi-Physics* (accepted).
- [2] Grundmann, U. et al. (2000). *Proc. of Int. Topl. Mtg. on Advances in Reactor Physics and Mathematics and Computation into the Next Millennium* (PHYSOR2000), Pittsburgh, U.S.A.
- [3] Lassmann, K. (1992) *J. Nucl. Mat.* **188**, 295–302.
- [4] Kliem, S. (2010) *Ein Modell zur Beschreibung der Kühlmittelvermischung und seine Anwendung auf die Analyse von Borverdünnungstransienten in Druckwasserreaktoren*, Ph.D.Thesis. Technische Universität Dresden, Germany.

Implementation of the CCCP solver for pin-power reconstruction in DYN3D – First results

D. Litskevich, B. Merk

An advanced methodology based on the current coupling collision probability method with an orthonormal expansion of the flux is applied for pin-power reconstruction in DYN3D code. The results of the calculations using proposed methodology for the test mini assembly demonstrate good agreement with the results of the full core transport calculations.

The aim of many reactor calculations is the determination of the neutron flux and the nuclear power distribution. These distributions are in general calculated by solving the space and energy dependent transport equation. Thus, a reliable computation of the neutron flux distribution within the reactor core would require the solution of the neutron transport equation for the full nuclear reactor core. For practical use, approximations are applied in modern nodal computer codes. One of these computer codes is DYN3D. The DYN3D code is based on the nodal expansion method. It applies for the calculations fuel assembly wise homogenized cross-sections and determines fluxes homogenized for each node in the core. However, for safety calculations good knowledge of power and distributions on assembly level is not detailed enough. In most cases the ability to predict accurately the local pin powers in nuclear reactors is necessary. This knowledge helps to evaluate the safety margins and to understand the mechanisms that cause fuel pin failure during steady state and transient operation. The distribution of the power inside assembly can be determined as combination between full core diffusion solution and transport solution inside assembly of interest. According to this methodology, the full core calculation is used to define partial incoming currents as boundary conditions for a local problem. The boundary conditions describe the coupling of the local problem which will be solved by a transport solver to the global problem. The local problem in its turn is solved using transport approximation. In present work current coupling collision probability with orthonormal flux expansion is used as transport solver. Currently, transport

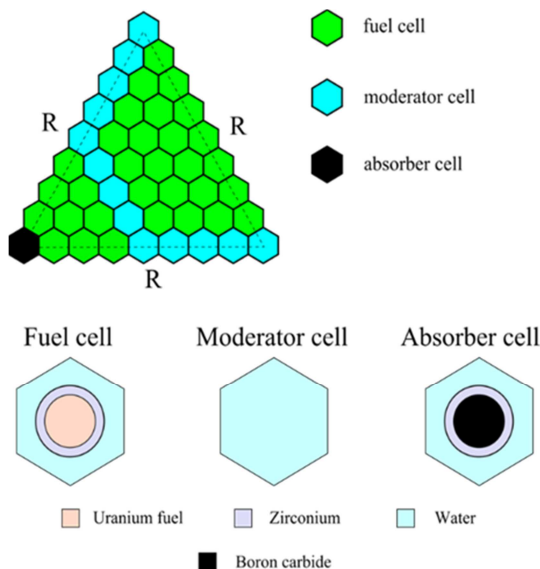


Fig. 1: Material map and geometry of the test problem for pin-power reconstruction.

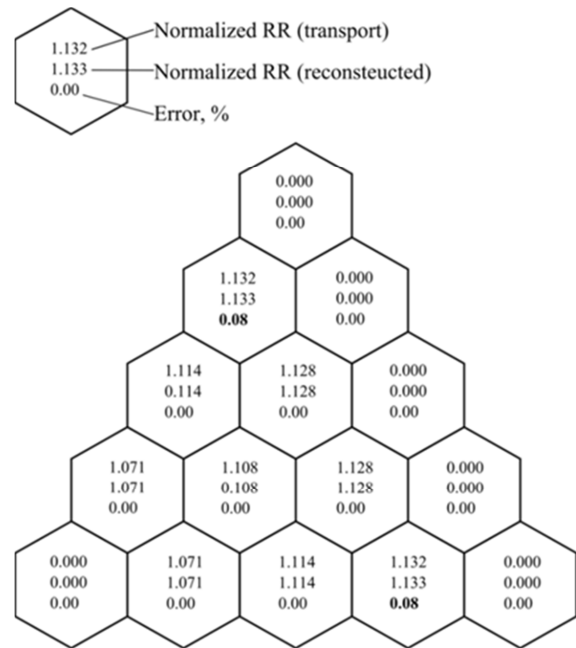


Fig. 2: Results of the calculations for the test mini assembly and comparison with MCU (flux averaged on cell level).

solver on the level of full assembly is available only for the regular hexagonal lattices. The results of its verification are described in details in the work [2]. The developed solver has been introduced in the DYN3D code as additional module.

DESCRIPTION OF THE TEST PROBLEM AND RESULTS OF CALCULATIONS. In order to evaluate efficiency of the proposed methodology for pin-power reconstruction inside chosen assembly, the test case with mini-assemblies has been proposed. The geometry of the test case as well as material maps in 60 degree symmetry are presented in Fig. 1. The test case simulates the assembly with inserted control rod, surrounded by the fuel assemblies. The one-group cross-sections sets have been prepared using HELIOS code. For the DYN3D code, the cross-sections have been homogenized for each assembly; for the transport solver, cross-sections have been homogenized for each material separately. After that, the nodal calculations with DYN3D code have been performed and reconstruction of the flux inside the absorber mini-assembly has been performed. Results of the pin-power reconstruction and comparison with the full-core transport solutions are presented in Fig. 2. As it can be seen from the Fig. 2, results of pin power reconstructions agree quite well with the reference full core transport calculations. Except two corner cells, the difference between reconstructed and transport reaction rates are equal to zero. The small deviations in the corner cells can be explained by the loss of the accuracy for the evaluation of the boundary conditions for these cells.

[1] Grundmann, U. et al. (2000) DYN3D three-dimensional core model for steady-state and transient analysis of thermal reactors, In: *Proc. PHYSOR 2000*, Pittsburgh, Pennsylvania, U.S.A.
 [2] Litskevich, D. et al. (2014) *J. Comp. Theoret. Transport* **43**, 214–239.

Feasibility assessment of the once-through thorium fuel cycle for the PTVM LWR concept

R. Rachamin, E. Fridman, A. Galperin¹

¹Department of Nuclear Engineering, Ben-Gurion University of the Negev, Beer Sheva, Israel

An innovative light water reactor concept, which holds a great potential of improving the fuel utilization, has emerged recently based on an idea of “breed & burn” mode of operation. The novel concept, named the PTVM LWR [1], is a pressure tube type reactor in which the “breed & burn” mode of operation is implemented by a dynamic variation of the moderator content in the core. The PTVM LWR is based on the ACR-1000 [2] design with several simple modifications. First, the inter fuel channel assemblies spacing, surrounded by the calandria tank, contains a low pressure gas instead of heavy water moderator. Second, the calandria tank is surrounded by a 50 cm-thick and 25 cm-thick graphite reflector in the radial and horizontal direction, respectively. Finally, the fuel channel assembly, which is the basic unit of the PTVM LWR design, features an additional/external tube (designated as moderator tube) connected to a separate light water moderator management system. The moderator management system is designed to vary the moderator tube content from “dry” (gas) to “flooded” (light water filled). The fuel channel assemblies are arranged in the core in a hexagonal lattice. The total number of the fuel channel assemblies can be varied according to the desired core power. In the previous study [1], the once-through low-enriched uranium (LEU) fuel cycle was employed in the PTVM LWR concept. The general purpose of this investigation was to explore the physics aspects of the PTVM LWR design and estimate the potential benefits of a traditional LEU-based fuel cycle operating in a “breed & burn” mode. In the present study, the emphasis is placed on developing an open (once-through) thorium fuel cycle concept that would facilitate both high fuel utilization and increased proliferation resistance.

CORE DESIGN AND FUEL MANAGEMENT CONSIDERATION. The once-through thorium fuel cycle is employed in a 3310 MWt PTVM LWR core, consisting of 540 novel fuel channel assemblies seated in a seed-blanket arrangement. The core is divided into five separated regions: three regions of UO₂ fuel, known as seed regions (60% of the core), and two regions of (Th-U)O₂ fuel, known as blanket regions (40% of the core). Each region consists of 108 fuel channel assemblies. A novel fuel in-core management scheme, based on two separate fuel flow routes (i.e., seed route and blanket route), is employed. The seed regions are reshuffled and reloaded according to 3-batches in-core fuel management scheme, while the blanket batches are periodically reshuffled (interchanged) between the inner and outer blanket regions. As a first design option, the target discharge burnup of the blanket batches is set to be about 60 GWd/T. In order to keep the core critical and supply neutrons to the blanket, each reloaded cycle 1/3 of the seed is replaced by a fresh seed batch. Due to their relatively short in-core residence time, the seed batches are discharged with an insufficient accumulated burnup. This fact can be a strong drawback from fuel economy point of view. In order to overcome this drawback and improve the seed utilization, it is desired to return the discharged seed batches into the core for additional “post-burn” cycles. Therefore, it is suggest-

ed to divide the novel fuel in-core management scheme into two distinct periods: 1) Th-U period, which is based on separate seed and blanket fuel flow routes (as described so far), and 2) all-U period, which is based only on seed fuel management, involving “post-burn” of the discharged seed batches. Following the blanket in-core residence time (end of the Th-U period), the blanket batches are discharged and the core is rearranged to host the discharged seed batches for additional “post-burn” (all-U period). The main design idea of the all-U period is that each of the seed batches will reside in the core for total of 4 reloaded cycles. Thereby, the 3-batches seed fuel management, applied in the Th-U period, is upgraded to a 4-batches seed fuel management scheme (hosted in 4 of the 5 core regions). The remind region is used to host, each reloaded cycle, one of the discharged seed batches for additional “post-burn”. Following the all-U period, the Th-U period start all over again. The feasibility of such a novel core fuel management is demonstrated in this study.

NEUTRONIC PERFORMANCE ANALYSIS. A novel fuel in-core management scheme for the PTVM LWR design is proposed and described in the previous section. In order to assess the feasibility of such a scheme, a 3D full core model with on-line stepwise moderator addition was analyzed. The analysis was performed using the BGCORE Monte-Carlo based depletion code [3]. As mentioned earlier, the novel fuel in-core management is composed of two designated periods: the Th-U period and the all-U period. The fuel utilization values of the different periods are presented in Tab. 1. The fuel utilization (FU) is defined as the amount of energy produced per unit mass of natural uranium. It can be noted that the fuel utilization of the Th-U period (after the post burn of the seed batches) and the all-U period are 6.36 and 4.95 GWd/T NU, respectively. While the fuel utilization of the Th-U period increases by about 22% in compared with LWR’s of current technology, the fuel utilization of the all-U doesn’t present any improvement. The global fuel utilization (all-periods) is 5.65 GWd/T NU. Hereby, the global improvement is only about 9% in cooperation with LWR’s of current technology.

Tab. 1: Fuel utilization (FU) summary.

	FU, GWd/T NU
Th-U period	6.36
All-U period	4.95
All-periods	5.65

[1] Rachamin, R. et al. (2013) *Ann. Nucl. Energy* **60**, 248–255.
[2] AECL (2007) ACR-1000 Technical Summary, AECL, Canada.
[3] Fridman, E. et al. (2008) *Proc. PHYSOR 2008*, Switzerland.

Accident analyses on a prismatic High Temperature Reactor

S. Baier, S. Kliem, M. Schreier¹

¹Institute of Power Engineering, Technische Universität Dresden, Dresden, Germany

The reactor dynamics code DYN3D [1, 2] was coupled with the multi-physics code COMSOL [3] to analyze an accident scenario with complete loss of coolant in a prismatic High Temperature Reactor (HTR).

The joint research project SYNKOPE was dedicated to significant improvement of the conversion of brown coal. An HTR was chosen as energy source due to its potential to provide high temperature process heat as well as electricity. Therefore, its inherent safety during accident scenarios has to be proven. Earlier studies with the reactor dynamics code version DYN3D-HTR (e.g. [4]) showed the applicability of DYN3D-HTR for short-time transients (e.g. due to blackout) was identified as the most perilous design basis accident concerning maximum temperatures within the core or within the surrounding structures. Since DYN3D is not able to model structures outside the reactor core, it was coupled with the code COMSOL.

METHODOLOGY. The DYN3D core design is based on a benchmark definition of a prismatic HTR [5]. It contains 271 fuel assemblies. The accident is modelled in the following way. The time- and space-dependent core power after shut down was taken from [5]. The coolant mass flow density was reduced to 1% in the time interval from 2 s to 12 s. Thereafter, the heat transfer coefficient to the coolant was set to zero. Thus, heat removal is possible only via the radial core boundary.

COMSOL modelled the heat transfer through the surrounding structures including a steel liner followed by a set-up of steel with helium coolant channels, the reactor pressure vessel (RPV) steel, an air-filled annular gap and cement.

The two codes were iteratively coupled. DYN3D provided time- and space-dependent heat fluxes at the radial core boundary. They were used by COMSOL to provide respecting boundary temperatures which in turn were used by DYN3D to calculate new heat fluxes. Four iterations were performed.

RESULTS. Figure 1 shows the temporal evolution of the maximum temperature of the graphite for adjacent assemblies. Assembly 157 contains fuel and has the highest fuel and graphite temperature during the whole transient. Assemblies 158–163 represent a ring of fuel or reflector assemblies each, whereupon assembly 163 is located at the radial core boundary. The main result is that the safety-critical temperature of 1600 °C is not exceeded. The sudden decrease of the temperature in the fuel zone (157–159) near $t = 0$ is due to the shut-off of the reactor and, hence, the decrease of the produced fission power. Furthermore, radial heat conduction can be clearly deduced from the temperature curves. The maximum graphite temperature decreases continuously. The heat is transferred to neighboring assemblies. For this reason, the temperature in the reflector elements (especially close to or at the boundary) increases. After 80 hours, the maximum temperature is reached in those assemblies.

Figure 2 shows a similar temporal evolution of the temperature for different peripheral elements at two axial positions.

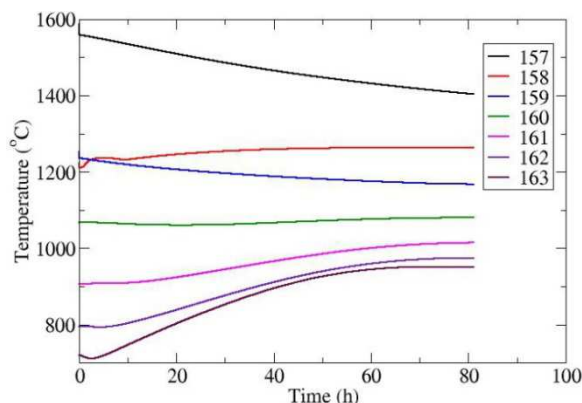


Fig. 1: Temporal evolution of maximum graphite temperature for selected radially adjacent assemblies (157: fuel assembly, 163: reflector assembly at core boundary).

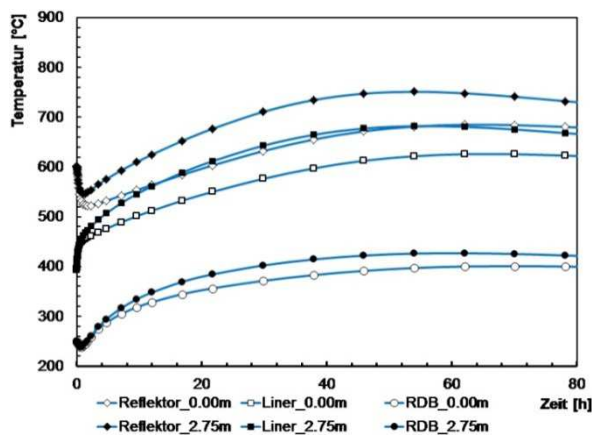


Fig. 2: Temporal evolution of the temperature of peripheral elements for the most heated outer assembly at two axial positions.

sitions in the periphery of the most heated outer assembly. The maximum temperature is reached after about 60 hours. The temperature of the RPV and of the liner stays below 450 °C and below 800 °C, respectively. Thus, the integrity of the structure materials and, hence, the inherent safety of the HTR during this accident scenario is proven. More information can be found in [6].

ACKNOWLEDGEMENTS. This project was funded by SAB, grant No. 51 2121 2101.

- [1] Grundmann, U. et al. (2000) Proc. PHYSOR2000.
- [2] Manera, A. et al. (2005) *Nucl. Eng. Design* **235**, 1517.
- [3] COMSOL-4.2a: Multiphysics modeling, finite element analysis, and engineering, <http://www.comsol.com>.
- [4] Baier, S. et al. (2014) *Nucl. Eng. Design* **271**, 431–436.
- [5] J. Ortensi et al. (2012) „OECD benchmark for prismatic coupled neutronics/thermal fluids transient of the MHTGR-350 MW core design: Benchmark definition,“ INL.
- [6] Kliem, S. et al. (2014) Meilensteinreport im SYNKOPE-Projekt (TP5).

SPECIAL CONTRIBUTION

**THE GERMAN STUDY FOR
PARTITIONING & TRANSMUTATION**

The German P&T study – Results and conclusions in the view of the contributing Helmholtz research centers

B. Merk, A. Geist,¹ G. Modolo,² J. Knebel¹

¹Karlsruher Institut für Technologie, Karlsruhe, Germany; ²Forschungszentrum Jülich, Jülich, Germany

The political decision to phase out electric energy production in nuclear power plants in Germany has put some important and urgent questions on the future of P&T research in Germany. To answer these questions on a broad scientific basis, the Federal Ministry for Economic Affairs and Energy and the Federal Ministry of Education and Research have launched a study managed by the National Academy of Science and Engineering (*acatech*). The major objective of the German Study was to evaluate scientific and technological as well as socio-economic challenges and opportunities of the P&T technology in the view of the phase out decision. The results are published as an *acatech* STUDIE, a 300 page report giving a comprehensive view on the situation of P&T in Germany [1]. Based on the STUDIE, an *acatech* POSITION [2] was prepared by *acatech*. The POSITION's text was agreed upon by all participants to the STUDIE. The POSITION gives *acatech*'s conclusions and political recommendations regarding the future of P&T research in Germany. Based on these recommendations conclusions have been drawn for the future work in the contributing Helmholtz Research Centers [3, 4].

SCENARIOS.

- **Abstinence**
Germany operates no transmutation facility; no research on P&T is institutionally funded.
- **Participation to research**
Germany carries out national research to maintain an influence on international bodies and participates to international research programs.
- **Participation to European Systems**
Germany carries out national research and actively participates to international research programmes and to European initiatives towards the construction of P&T facilities.
- **Application in Germany**
Both P&T research and the construction of P&T facilities are actively carried out as part of a national waste management strategy.

The consequences of these scenarios have been evaluated and have been compared based on a broad choice of methods to provide a specific chances-to-risk estimation.

RECOMMENDATIONS BY *acatech*.

1. P&T research in a European context as well as the evaluation of a future German contribution to P&T in Europe is recommended.
2. Participation to research should not lead to any dependency regarding investments into future application of P&T.
3. An interdisciplinary, comprehensive study should be worked out as basis for a decision on a possible contribution to P&T in Europe. Processes involving the general public should be planned in time for a decision to be expected in 10 to 15 years.
4. Germany should follow the European perspective as well as national research activities related to the phase out decision.

5. The German industry should consider a possible implementation of P&T as a chance.
6. Research should focus on key topics:
 - Efficient partitioning
 - Efficient transmutation of the TRUs
 - Safety evaluation of the facilities
 - Societal implications of all options
7. An interdisciplinary approach must be followed to evaluate and communicate scientific and technological development to the public.
8. A research alliance should be established.

CONCLUSIONS. The centres of the Helmholtz Association expect that the ministries consider the recommendations given by *acatech* in order to scientifically contribute to the decision on how to proceed with the national P&T research in Germany.

Based on the budget given in the POF III period, starting in January 2015, the continuation of the research cooperation within both European and international networks is planned to be continued as previously has been the case within several European framework programs. A focus will remain on major challenges to be solved for safe and reliable operation of P&T facilities such as advanced separation technologies, liquid metal technologies, advanced components and structural materials, and development and application of simulation tools.

acatech concludes that additional funding may be required to contribute to European initiatives or investigations in line with German phase out decision. European initiatives are currently driven by the MYRRHA project; however, the scope could be broadened. *acatech* recommends additional funding for creating dedicated European infrastructures. This is well recognised by the Helmholtz centres, which are highly interested and willing to participate to European initiatives. Additional funding would allow work with focus on the specific situation given by the phase out decision. The work should be started on a comparison of different P&T systems and how they comply with the phase out decision, i.e. using as few facilities as possible for an operating period as possible, generating as little TRU losses as possible. Based on the results, a system should be selected and developed to demonstrate the feasibility of P&T under the objectives of the phase out decision. Finally, a system optimised for TRU burning could be an attractive option for many countries operating a fleet of LWR only, not willing to switch to a fast reactor fleet of significant size.

[1] Renn, O. (ed.) (2014) *Partitionierung und Transmutation. Forschung – Entwicklung – Gesellschaftliche Implikationen (acatech STUDIE)*, Herbert Utz Verlag, München.

[2] *acatech* (ed.) (2014) *Partitionierung und Transmutation nuklearer Abfälle. Chancen und Risiken in Forschung und Anwendung (acatech POSITION)*, Herbert Utz Verlag, München.

[3] Merk, B. et al. (2014) 13th IEM Actinide and Fission Product Partitioning and Transmutation, Seoul, Republic of Korea.

[4] Merk, B. et al. (2015) 46th Ann. Mtg. on Nuclear Technology, Berlin.

- ▣ ARTICLES (PEER-REVIEWED)
- ▣ ORAL PRESENTATIONS
- ▣ PATENTS
- ▣ THESES

ARTICLES (PEER-REVIEWED)

- Abu Sharkh, S. E.; Erkut, C.; Oertel, J.; Kurzchalia, T. V.; Fahmy, K.
The role of phospholipid headgroup composition and trehalose in the desiccation tolerance of *Caenorhabditis elegans*
Langmuir 30, 12897–12906 (2014).
- Baier, S.; Fridman, E.; Kliem, S.; Rohde, U.
Extension and application of the reactor dynamics code DYN3D for Block-type High Temperature Reactors
Nuclear Engineering and Design 271, 431–436 (2014).
- Baldova, D.; Fridman, E.; Shwageraus, E.
High Conversion Th-U233 fuel for current generation of PWRs: Part I – Assembly level analysis
Annals of Nuclear Energy 73, 552–559 (2014).
- Baldova, D.; Fridman, E.; Shwageraus, E.
High Conversion Th-U233 fuel for current generation of PWRs: Part II – 3D full core analysis
Annals of Nuclear Energy 73, 560–566 (2014).
- Barkleit, A.; Kretzschmar, J.; Tsushima, S.; Acker, M.
Americium(III) and europium(III) complex formation with lactate at elevated temperatures studied by spectroscopy and quantum chemical calculations
Dalton Transactions 43, 11221–11232 (2014).
- Barth, T.; Kulenkampff, J.; Bras, S.; Gründig, M.; Lippmann-Pipke, J.; Hampel, U.
Positron emission tomography in pebble beds. Part 2: Graphite particle deposition and resuspension
Nuclear Engineering and Design 267, 227–237 (2014).
- Barth, T.; Ludwig, M.; Kulenkampff, J.; Gründig, M.; Franke, K.; Lippmann-Pipke, J.; Hampel, U.
Positron emission tomography in pebble beds. Part 1: Liquid particle deposition
Nuclear Engineering and Design 267, 218–226 (2014).
- Bauer, J. D.; Labs, S.; Weiss, S.; Bayarjargal, L.; Morgenroth, W.; Milman, V.; Perlov, A.; Curtius, H.; Bosbach, D.; Zänker, H.; Winkler, B.
High pressure phase transition of coffinite, USiO_4
Journal of Physical Chemistry C 118, 25141–25149 (2014).
- Baumann, N.; Arnold, T.; Haferburg, G.
Uranium contents in plants and mushrooms grown on a uranium contaminated site near Ronneburg in Eastern Thuringia/Germany
Environmental Science and Pollution Research 21, 6921–6929 (2014).
- Belle, C. J.; Wesch, G. E.; Neumeier, S.; Lozano-Rodríguez, M. J.; Scheinost, A. C.; Simon, U.
Volume-doped cobalt titanates for ethanol sensing: an impedance and X-ray absorption spectroscopy study
Sensors and Actuators B 192, 60–69 (2014).
- Böhler, R.; Welland, M. J.; Prieur, D.; Cakir, P.; Vitova, T.; Pruessmann, T.; Pidchenko, I.; Hennig, C.; Guéneau, C.; Konings, R. J. M.; Manara, D.
Recent advances in the study of the UO_2 – PuO_2 phase diagram at high temperatures
Journal of Nuclear Materials 448, 330–339 (2014).
- Brockmann, S.; Arnold, T.; Bernhard, G.
Speciation of bioaccumulated uranium(VI) by *Euglena mutabilis* cells obtained by laser fluorescence spectroscopy
Radiochimica Acta 102, 411–422 (2014).
- Dulnee, S.; Scheinost, A. C.
Surface reaction of Sn(II) on goethite (α - FeOOH): surface complexation, redox reaction, reductive dissolution, phase transformation
Environmental Science & Technology 48, 9341–9348 (2014).
- Foerstendorf, H.; Jordan, N.; Heim, K.
Probing the surface speciation of U(VI) on iron (hydr)oxides by in situ ATR FT-IR spectroscopy
Journal of Colloid and Interface Science 416, 133–138 (2014).

- Gomez, A.; Sanchez Espinosa, V. H.; Kliem, S.; Gommlich, A.
Implementation of a fast running full core pin power reconstruction method in DYN3D
Nuclear Engineering and Design 274, 44–55 (2014).
- Günther, A.; Raff, J.; Merroun, M. L.; Roßberg, A.; Kothe, E.; Bernhard, G.
Interaction of U(VI) with *Schizophyllum commune* studied by microscopic and spectroscopic methods
BioMetals 27, 775–785 (2014).
- Günther, T. J.; Suhr, M.; Raff, J.; Pollmann, K.
Immobilization of microorganisms for AFM studies in liquids
RSC Advances 4, 51156–51164 (2014).
- Harzmann, S.; Braun, F.; Zakhnini, A.; Weber, W.A.; Pietrzyk, U.; Mix, M.
Implementation of cascade gamma and positron range corrections for I-124 small animal PET
IEEE Transactions on Nuclear Science 61, 142–153 (2014).
- Haupt, S.; Handke, M.; Kuhnert, R.; Poetsch, M.; Kersting, B.
Synthesis of calix[4]arene-based polycarboxylate ligands and their chemical immobilization onto controlled-pore glass
Tetrahedron 70, 5254–5259 (2014).
- Haupt, S.; Schnorr, R.; Poetsch, M.; Mansel, A.; Handke, M.; Kersting, B.
Extraction properties of 25,27-bis(carbonyl-methoxy)calix[4]arenes towards Sr²⁺: competitive extraction and extraction in a synthetic groundwater
Journal of Radioanalytical and Nuclear Chemistry 300, 779–786 (2014).
- Hoffmann, A.; Merk, B.; Hirsch, T.; Pitz-Paal, R.
Simulation of thermal fluid dynamics in parabolic trough receiver tubes with direct steam generation using the computer code ATHLET
Kerntechnik 79, 175–186 (2014).
- Hofmann, S.; Voitchovsky, K.; Schmidt, M.; Stumpf, T.
Trace concentration – Huge impact: nitrate in the calcite/Eu(III) system
Geochimica et Cosmochimica Acta 125, 528–538 (2014).
- Holt, L.; Schubert, A.; van Uffelen, P.; Walker, C. T.; Fridman, E.; Sonoda, T.
Sensitivity study on Xe depletion in the high burn-up structure of UO₂
Journal of Nuclear Materials 452, 166–172 (2014).
- Hoyer, M.; Zabelt, D.; Steudtner, R.; Brendler, V.; Haseneder, R.; Repke, J.
Influence of speciation during membrane treatment of uranium contaminated water
Separation and Purification Technology 132, 413–421 (2014).
- Jordan, N.; Ritter, A.; Scheinost, A. C.; Weiß, S.; Schild, D.; Hübner, R.
Selenium(IV) uptake by maghemite (γ-Fe₂O₃)
Environmental Science & Technology 48, 1665–1674 (2014).
- Kozmenkov, Y.; Rohde, U.
Application of the method for uncertainty and sensitivity evaluation to results of PWR LBLOCA analysis calculated with the code ATHLET. Part 2: Sensitivity analysis
Kerntechnik 79, 97–102 (2014).
- Krepel, J.; Hombourger, B.; Fiorina, C.; Mikityuk, K.; Rohde, U.; Kliem, S.; Pautz, A.
Fuel cycle advantages and dynamics features of liquid fueled MSR
Annals of Nuclear Energy 64, 380–397 (2014).
- Kretzschmar, J.; Brendler, E.; Wagler, J.; Schmidt, A. C.
Kinetics and activation parameters of the reaction of organoarsenic(V) compounds with glutathione
Journal of Hazardous Materials 280, 734–740 (2014).
- Labs, S.; Hennig, C.; Weiss, S.; Curtius, H.; Zaenker, H.; Bosbach, D.
Synthesis of coffinite, USiO₄, and structural investigations of the U_xTh_(1-x)SiO₄ solid solutions
Environmental Science & Technology 48, 854–860 (2014).
- Lebreton, F.; Martin, P.M.; Horlait, D.; Bes, R.; Scheinost, A. C.; Rossberg, A.; Delahaye, T.; Blanchart, P.
New insight into self-irradiation effects on local and long-range structure of uranium-amerium mixed oxides (through XAS and XRD)
Inorganic Chemistry 53, 9531–9540 (2014).

- Lederer, F. L.; Günther, T.J.; Raff, J.; Flemming, K.; Pollmann, K.
Eigenschaften von Bakterien aus Schwermetall-kontaminierten Halden: Mikrobielle Ökologie
Biospektrum 20, 172–175 (2014).
- Leppanen, J.; Aufiero, M.; Fridman, E.; Rachamin, R.; van der Marck, S.
Calculation of effective point kinetics parameters in the Serpent 2 Monte Carlo code
Annals of Nuclear Energy 65, 272–279 (2014).
- Lippold, H.; Lippmann-Pipke, J.
New insights into the dynamics of adsorption equilibria of humic matter as revealed by radiotracer studies
Geochimica et Cosmochimica Acta 133, 362–371 (2014).
- Litskevich, D.; Merk, B.
SP3 solution versus diffusion solution in pin-by-pin calculations and conclusions concerning advanced methods
Transport Theory and Statistical Physics 43, 214–239 (2014).
- Mansel, A.; Gruhne, S.; Franke, K.; Fischer, S.
Production of ^{85}Sr at a 18 MeV-cyclotron and purification for geochemical investigations
Applied Radiation and Isotopes 92, 22–24 (2014).
- Merk, B.; Konheiser, J.
Neutron shielding studies on an advanced molten salt fast reactor design
Annals of Nuclear Energy 64, 441–448 (2014).
- Merk, B.; Rohde, U.; Glivici-Cotruță, V.; Scholl, S.
On the use of a Molten Salt Fast Reactor to apply an idealized transmutation scenario for the nuclear phase out
PlosOne 9, e92776 (2014).
- Moll, H.; Lütke, L.; Cherkouk, A.; Selenska-Pobell, S.; Bernhard, G.; Bachvarova, V.
Interactions of the Mont Terri Opalinus Clay isolate *Sporomusa sp.* MT-2.99 with curium(III) and europium(III)
Geomicrobiology Journal 31, 682–696 (2014).
- Moll, H.; Rossberg, A.; Steudtner, R.; Drobot, B.; Müller, K.; Tsushima, S.
Uranium(VI) Chemistry in Strong Alkaline Solution: Speciation and Oxygen Exchange Mechanism
Inorganic Chemistry 53, 1585–1593 (2014).
- Morcillo, F.; Gonzalez-Munoz, M. T.; Reitz, T.; Romero-Gonzalez, M. E.; Arias, J. M.; Merroun, M. L.
Biosorption and biomineralization of U(VI) by the marine bacterium *Idiomarina loihiensis* MAH1: effect of background electrolyte and pH
PlosOne 9, e91305 (2014).
- Opherden, L.; Oertel, J.; Barkleit, A.; Fahmy, K.; Keller, K.
Paramagnetic decoration of DNA origami nanostructures by Eu^{3+} coordination
Langmuir 30, 8152–8159 (2014).
- Pannier, A.; Lehrer, T.; Vogel, M.; Soltmann, U.; Böttcher, H.; Tarre, S.; Green, M.; Raff, J.; Pollmann, K.
Long-term activity of biohybrid coatings of atrazine-degrading bacteria *Pseudomonas sp.* ADP
RSC Advances 4, 19970–19979 (2014).
- Petrovska, I.; Nüske, E.; Munder, M. C.; Kulasegaran, G.; Malinowska, L.; Kroschwald, S.; Richter, D.; Fahmy, K.; Gibson, K.; Verbavatz, J. M.; Alberti, S.
Filament formation by metabolic enzymes is a specific adaptation to an advanced state of cellular starvation
eLife 3, 02409 (2014).
- Prasser, H. M.; Kliem, S.
Coolant mixing experiments in the upper plenum of the ROCOM test facility
Nuclear Engineering and Design 276, 30–42 (2014).
- Radeva, G.; Kenarova, A.; Bachvarova, V.; Flemming, K.; Popov, I.; Vassilev, D.; Selenska-Pobell, S.
Phylogenetic diversity of archaea and the archaeal ammonia monooxygenase gene in uranium mining-impacted locations in Bulgaria
Archaea, 196140 (2014).
- Reitz, T.; Rossberg, A.; Barkleit, A.; Selenska-Pobell, S.; Merroun, M. L.
Decrease of U(VI) immobilization capability of the facultative anaerobic strain *Paenibacillus sp.* JG TB8 under anoxic conditions due to strongly reduced phosphatase activity
PlosOne 9(8), e102447 (2014).

- Sabau, A.; Pipon, Y.; Toulhoat, N.; Lomenech, C.; Jordan, N.; Moncoffre, N.; Barkleit, A.; Marmier, N.; Brendler, V.; Surblé, S.; Giffaut, E.
Interaction of europium and nickel with calcite studied by Rutherford Backscattering Spectrometry and Time-Resolved Laser Fluorescence Spectroscopy
Nuclear Instruments and Methods in Physics Research B 332, 116 (2014).
- Schmeide, K.; Gürtler, S.; Müller, K.; Steudtner, R.; Joseph, C.; Bok, F.; Brendler, V.
Interaction of U(VI) with Äspö diorite: A batch and in situ ATR FT-IR sorption study
Applied Geochemistry 49, 116–125 (2014).
- Schmid, M.; Guillaume, S. M.; Roesky, P. W.
 β -Diketiminato rare earth borohydride complexes: synthesis, structure, and catalytic activity in the ring-opening-polymerization of ϵ -caprolactone and trimethylene carbonate
Organometallics 33, 5392–5401 (2014).
- Schmoock, C.; Börnick, H.; Vogel, M.; Lehmann, F.; Kutschke, S.; Raff, J.; Dittmar, T.; Worch, E.
S-layer proteins as possible immobilization matrix for photocatalysts – OH radical scavenging capacity and protein stability
Journal of Photochemistry and Photobiology A: Chemistry 277, 12–18 (2014).
- Schott, J.; Kretzschmar, J.; Acker, M.; Eidner, S.; Kumke, M. U.; Drobot, B.; Barkleit, A.; Taut, S.; Brendler, V.; Stumpf, T.
Formation of a Eu(III) borate solid species from a weak Eu(III) borate complex in aqueous solution
Dalton Transactions 43, 11516–11528 (2014).
- Smith, A. L.; Raison, P. E.; Martel, L.; Charpentier, T.; Farnan, I.; Prieur, D.; Hennig, C.; Scheinost, A. C.; Konings, R. J. M.; Cheetham, A. K.
A ^{23}Na magic angle spinning nuclear magnetic resonance, XANES, and high temperature X-Ray diffraction study of NaUO_3 , Na_4UO_5 , and $\text{Na}_2\text{U}_2\text{O}_7$
Inorganic Chemistry 53, 375–382 (2014).
- Soltermann, D.; Marques Fernandes, M.; Baeyens, B.; Dähn, R.; Joshi, P.A.; Scheinost, A. C.; Gorski, C. A.
Fe (II) uptake on natural montmorillonites. I. Macroscopic and spectroscopic characterization
Environmental Science & Technology 48, 8688–8697 (2014).
- Suhr, M.; Unger, N.; Viacava, K.E.; Günther, T.J.; Raff, J.; Pollmann, K.
Investigation of metal sorption behavior of Slp1 from *Lysinibacillus sphaericus* JG-B53 – A combined study using QCM-D, ICP-MS and AFM
BioMetals 27, 1337–1349 (2014).
- Takao, K.; Tsushima, S.; Ogura, T.; Tsubomura, T.; Ikeda, Y.
Experimental and theoretical approaches to redox innocence of ligands in uranyl complexes: what is formal oxidation state of uranium in reductant of uranyl(VI)?
Inorganic Chemistry 53, 5772–5780 (2014).
- Tits, J.; Walther, C.; Stumpf, T.; Macé, N.; Wieland, E.
A luminescence line-narrowing spectroscopic study of the uranium(VI) interaction with cementitious materials and titanium dioxide
Dalton Transactions 44, 966–976 (2014).
- Tusheva, P.; Schäfer, F.; Reinke, N.; Kamenov, Al.; Mladenov, I.; Kamenov, K.; Kliem, S.
Assessment of accident management measures on early in-vessel station blackout sequence at VVER-1000 pressurized water reactors
Nuclear Engineering and Design 277, 106–116 (2014).
- Viehweger, K.; Barbaro, L.; Pombo García, K.; Joshi, T.; Geipel, G.; Steinbach, J.; Stephan, H.; Spiccia, L.; Graham, B.
EGF receptor-targeting peptide conjugate incorporating a near-IR fluorescent dye and a novel 1,4,7-triazacyclononane-based 64Cu(II) chelator assembled via click chemistry
Bioconjugate Chemistry 25, 1011–1022 (2014).
- Zänker, H.; Hennig, C.
Colloid-borne forms of tetravalent actinides: A brief review
Journal of Contaminant Hydrology 157, 87–105 (2014).

ORAL PRESENTATIONS

- Barthen, R.; Lippmann-Pipke, J.
Quantifying bioleaching kinetics and efficiency: (3D+t)-visualization of Cu transport through dump material by means of PET - First results from HZDR-IRE (11/2014)
Ecometals Meeting 2014, November 18–19, 2014, Orléans, France.
- Barthen, R.; Mickein, K.; Kutschke, S.; Pollmann, K.; Kulenkampff, J.; Gründig, M.; Lippmann-Pipke, J.
Development of a labeling system for microorganisms based on antimicrobial peptides
Gemeinsame Jahrestagung der DGHM und der VAAM, October 05–08, 2014, Dresden, Germany.
- Baumann, N.; Arnold, T.; Haferburg, G.
Uranium contents in plants and mushrooms grown on a uranium mining waste tip site in former eastern Germany
International Nuclear Science and Technology Conference 2014 (INST 2014), August 28–30, 2014, Bangkok, Thailand.
- Baumann, N.; Geipel, G.
Determination of uranium(VI)-speciation in natural occurring waters by Time-resolved Laser-induced Fluorescence Spectroscopy
Special lecture at the Department of Applied Radiation and Isotopes, Faculty of Science, Kasetsart University, August 27, 2014, Bangkok, Thailand.
- Bilodid, Y.; Fridman, E.; Kotlyar, D.; Margulis, M.; Shwageraus, E.
Verification of the spectral history correction method with fully coupled Monte Carlo code BGCORE
PHYSOR 2014 – The Role of Reactor Physics Toward a Sustainable Future, September 28–October 03, 2014, Kyoto, Japan.
- Bittner, L.; Kulenkampff, J.; Gründig, M.; Lippmann-Pipke, J.; Enzmann, F.
Direct observation of waterglass impregnation of fractured salt rock with Positron Emission Tomography
International Conference on the Performance of Engineered Barriers: Backfill, Plugs & Seals, February 06–07, 2014, Hannover, Germany.
- Bok, F.; Richter, A.; Brendler, V.
Sorption data: Ways from a plain collection to recommended values
248th ACS National Meeting, August 10–14, 2014, San Francisco, U.S.A.
- Brachem, C.; Konheiser, J.; Hampel, U.
The gamma radiation emitted by a PWR Core under severe accident conditions
22nd International Conference on Nuclear Engineering (ICONE22), July 07–11, 2014, Prague, Czech Republic.
- Brachem, C.; Konheiser, J.; Hampel, U.
Investigations on the discrimination of nuclear reactor core state changes by the external gamma radiation field
46th Annual Meeting on Nuclear Technology, May 05–07, 2014, Berlin, Germany.
- Breynaert, E.; Wangermez, W.; Dom, D.; Scheinost, A. C.; Parac-Vogt, T. N.; Kirschhock, C. E. A.; Maes, A.
Pathways for abiotic reduction in the FeS/Se(IV) and FeS₂/Se(IV) systems
Goldschmidt 2014, June 08–13, 2014, Sacramento, U.S.A.
- Britz, S.; Noseck, U.; Brendler, V.; Durner, W.; Zachmann, D.
A wrap up of modeling sorption processes of Eu³⁺ under varying geochemical conditions
TRePro III – Workshop on Modelling of Coupled Reactive and Transport Processes, March 05–07, 2014, Karlsruhe, Germany.
- Cherkouk, A.; Radeva, G.; Selenska-Pobell, S.
BN project – contribution from HZDR/IRE
TD-246 Joint BN, GD, HT, MA Mont Terri Meeting, February, 10–11, 2014, St. Ursanne, Switzerland.
- Drobot, B.
Biologische Bausteine für Materialien der Zukunft
Tage der Wissenschaften, July 02, 2014, Radebeul, Germany.
- Dumas, T.; Fellhauer, D.; Gaona, X.; Altmaier, M.; Scheinost, A.C.
Is plutonium being incorporated by magnetite under anoxic conditions?
248th ACS National Meeting, August 10–14, 2014, San Francisco, U.S.A.

- Fahmy, K.
Infrared spectroscopy on lipid–protein interactions: what crystals don't tell
564. WE-Heraeus-Seminar: Physical Approaches to Membrane Proteins, May 25–28, 2014, Bad Honnef, Germany.
- Foerstendorf, H.; Jordan, N.; Heim, K.
Surface speciation of dissolved radionuclides on mineral phases derived from vibrational spectroscopic data
248th ACS National Meeting, August 10–14, 2014, San Francisco, U.S.A.
- Franke, K.; Hildebrand, H.; Schymura, S.
Project NanoTrack – Untersuchung des Lebenszyklus von Nanopartikeln anhand von [⁴⁵Ti]TiO₂ und [¹⁰⁵Ag]AgO
27th Meeting of the DECHEMA/VCI-Working Party „Responsible Production and Use of Nanomaterials“, September 04, 2014, Frankfurt am Main, Germany.
- Franzen, C.
Berufsfelder in den Geowissenschaften - Als Mineralogin in der Endlagerforschung
Berufsfelder in den Geowissenschaften, June 23, 2014, Heidelberg, Germany.
- Franzen, C.
Natural distribution of heavy metals in wetlands - Evaluation of sources and processes
Lecture at North-West University, August 28, 2014, Vanderbijlpark, South Africa.
- Franzen, C.; Hering, D.; Jordan, N.; Weiss, S.
Retention of selenium oxyanions at the water-mineral interface in the context of nuclear waste repositories
21st General Meeting of the International Mineralogical Association, September 01–05, 2014, Johannesburg, South Africa.
- Fridman, E.
Generation of few-group constants with Serpent: application examples
PHYSOR 2014, Workshop on new features and capabilities in the Serpent 2 Monte Carlo code, September 28–October 03, 2014, Kyoto, Japan.
- Fritsch, K.; Schmeide, K.
Montmorillonite as barrier material for uranium(VI) at high ionic strengths
7th Mid-European Clay Conference, September 16–19, 2014, Dresden, Germany.
- Fritsch, K.; Schmeide, K.
Uranium sorption on montmorillonite at high ionic strengths: Surface complexation modelling
7. Workshop zum Verbundprojekt "Rückhaltung endlagerrelevanter Radionuklide im natürlichen Tongestein und in salinaren Systemen", October 28–29, 2014, Saarbrücken, Germany.
- Gerasch, R.; Kulenkampff, J.; Lippmann-Pipke, J.
Parameter estimation of anisotropic diffusion in clay with COMSOL Multiphysics
COMSOL Conference 2014, September 17–19, 2014, Cambridge, U.K.
- Grahn, A.; Kliem, S.; Rohde, U.
Coupling of the 3D neutron kinetic core model DYN3D with the CFD software ANSYS CFX
22nd International Conference on Nuclear Engineering (ICONE22), July 07–11, 2014, Prague, Czech Republic.
- Hennig, C.
Complex formation of tetravalent metal ions with small carboxylic ligands
Institut de Chimie de Nice Université de Nice Sophia Antipolis, October 31, 2014, Nice, France.
- Hennig, C.
Phase analysis with HRPD and XAFS in the USiO₄-ZrSiO₄ solid solution system
TALISMAN Projekt meeting, February, 06, 2014, Jülich, Germany.
- Hennig, C.
Polynuclear complexes of tetravalent actinides and lanthanides with simple carboxylate ligands
Forschungszentrum Jülich, Institute of Energy and Climate Research, February, 06, 2014, Jülich, Germany.
- Hennig, C.; Takao, K.; Takao, S.; Ikeda-Ohno, A.; Kraus, W.; Weiss, S.; Scheinost, A. C.
Formation and structure of polynuclear tetravalent actinide and lanthanide carboxylates in aqueous solution and solid state
Actinide XAS 2014, May 20–22, 2014, Schloss Boettstein, Switzerland.

- Hildebrand, H.; Franke, K.; Schymura, S.; Freyer, A.; Bilz, E.; Mehnert, R.; Mai, E.; Isaacson, C.; Schug, H.; Schirmer, K.; Ammann, A.; Sigg, L.
Investigation of the life cycle of titania NPs using radiolabeling techniques for highly sensitive NP detection
International Conference on Safe production and use of nanomaterials, Nanosafe 2014, November 18–20, 2014, Grenoble, France.
- Hildebrand, H.; Schymura, S.; Kulenkampff, J.; Lippmann-Pipke, J.; Franke, K.
Radiolabelling of colloids for highly sensitive detection in transport studies
Joined meeting of WP2 and WP4 within the EC project BELBaR, October 30–31, 2014, Prague, Czech Republic.
- Holt, L.
Completeness of DYN3D coupling approaches by the european fuel performance code TRANSURANUS – Full core analysis for a reactivity initiated accident
45th Annual Meeting on Nuclear Technology (Workshop Preserving Competence), May 06–08, 2014, Frankfurt, Germany.
- Ikeda-Ohno, A.; Johansen, M. P.; Payne, T. E.; Hotchkis, M. A. C.; Child, D. P.
XFM studies of plutonium dispersed in an arid environment
12th International Conference on X-Ray Microscopy (XRM 2014), October 26–31, 2014, Melbourne, Australia.
- Jordan, N.; Domaschke, S.; Foerstendorf, H.; Scheinost, A. C.; Franzen, C.; Zimmermann, V.; Weiss, S.; Heim, K.
Uptake of selenium oxyanions by hematite
Goldschmidt 2014, June 08–13, 2014, Sacramento, U.S.A.
- Kliem, S.
AER Working Group D on VVER safety analysis – Report of the 2014 meeting
24th Symposium of AER on VVER Reactor Physics and Reactor Safety, October 14–18, 2014, Sochi, Russian Federation.
- Konheiser, J.; Ferrari, A.; Naumann, B.; Müller, S.; Brachem, C.
Source and shielding calculations at a PET cyclotron and possible activation in the soil
14th AAA Workshop, December 01, 2014, Garching, Germany.
- Konheiser, J.; Grahn, A.; Borodkin, P.; Borodkin, G.
Uncertainties in the fluence determination in the surveillance samples of VVER-440
Fifteenth International Symposium on Reactor Dosimetry, May 18–23, 2014, Aix-en-Provence, France.
- Korn, N.; Lippmann-Pipke, J.
Algorithm for fluid velocity field quantification from image sequences in complex geomaterials
TRePro III 2014, March, 05–07, 2014, Karlsruhe, Germany.
- Kretzschmar, J.; Schott, J.; Barkleit, A.; Paasch, S.; Brunner, E.; Scholz, G.; Brendler, V.
Nuclear Magnetic Resonance Spectroscopy in rare earth and actinide research
Rare Earth Research Conference (RERC) 2014, June 22–26, 2014, Squaw Valley, Lake Tahoe, U.S.A.
- Kulenkampff, J.
Kontaminationsfreie Injektion von Radiotracer für die Prozesstomographie von Transportprozessen in Geomaterialien
ISCO-Anwendertreffen, December 09, 2014, Potsdam, Germany.
- Kulenkampff, J.; Gründig, M.; Zakhnini, A.; Lippmann-Pipke, J.
Process tomography of diffusion with PET for evaluating anisotropy and heterogeneity
7th Mid-European Clay Conference, September 16–19, 2014, Dresden, Germany.
- Kulenkampff, J.; Lippmann-Pipke, J.
High resolution Positron Emission Tomography for quantitative, spatio-temporal process visualization in geological material (GeoPET)
GeoCT Kick off Workshop Hannover, Nationaler Workshop von Forschungseinrichtungen mit tomographischen Methoden in den Geowissenschaften, February 19, 2014, Hannover, Germany.
- Kulenkampff, J.; Lippmann-Pipke, J.
Hochauflösende Positronen Emission Tomographie für quantitative, raumzeitliche Prozessvisualisierung in geologischem Material (GeoPET)
International Conference on the Performance of Engineered Barriers: Backfill, Plugs & Seals, February 06–07, 2014, Hannover, Germany.

- Kulenkampff, J.; Stoll, M.; Enzmann, F.; Gründig, M.; Mansel, A.; Lippmann-Pipke, J.
Spatiotemporal process monitoring of conservative and reactive tracer transport in a synthetic soil column
International Symposium 2014 Biogeochemical Interfaces in Soil: Towards a Comprehensive and Mechanistic Understanding of Soil Functions, October 06–08, 2014, Leipzig, Germany.
- Lippmann-Pipke, J.; Kulenkampff, J.
Quantification of permeability and porosity changes of cement/clay materials by means of GeoPET
Cebama Proposal Consortium Meeting, March 11, 2014, Karlsruhe, Germany.
- Lippold, H.
Gleichgewichtsdynamik der Huminstoff-Komplexbildung: Konzentrations- und zeitabhängige Effekte
7. Workshop zum Verbundprojekt "Rückhaltung endlagerrelevanter Radionuklide im natürlichen Tongestein und in salinaren Systemen", October 28–29, 2014, Saarbrücken, Germany.
- Litskevich, D.; Merk, B.
Development and verification of a transport solver for DYN3D
The 45th Annual Meeting on Nuclear Technology, May 06–08, 2014, Frankfurt, Germany.
- Merk, B.
Der Salzschnmelzenreaktor als Transmutationssystem vor dem Hintergrund des Kernenergieausstiegs
Seminar an der RWTH Aachen, July 08, 2014, Aachen, Germany.
- Merk, B.
Enhanced feedback effects in sodium cooled fast reactors using moderating material – The effect of the plutonium content in the fuel
PHYSOR 2014 – The Role of Reactor Physics Toward a Sustainable Future, September 28–October 03, 2014, Kyoto, Japan.
- Merk, B.; Geist, A.; Modolo, G.; Knebel, J.
The German P&T study – Results and conclusions in the view of the contributing Helmholtz research centers
Actinide and Fission Product Partitioning and Transmutation 13th Information Exchange Meeting, September 23–26, 2014, Seoul, Republic of Korea.
- Merk, B.; Konheiser, J.
On an optimized neutron shielding for an advanced molten salt fast reactor design
PHYSOR 2014 – The Role of Reactor Physics Toward a Sustainable Future, September 28–October 03, 2014, Kyoto, Japan.
- Moll, H.; Cherkouk, A.
Microorganisms and their impact on radionuclide speciation
8th European Summer School on Separation Chemistry and Conditioning as well as Supramolecular, Intermolecular, Interaggregate Interactions, July 07–09, 2014, Bonn/Bad Godesberg, Germany.
- Moll, H.; Lütke, L.; Cherkouk, A.; Bernhard, G.
Actinide/Lanthanide interaction studies with a typical bacterial isolate from Mont Terri Opalinus Clay a potential host rock for nuclear waste disposal
IGD-TP Geodisposal 2014 Conference, June 24–26, 2014, Manchester, U.K.
- Moll, H.; Lütke, L.; Cherkouk, A.; Bernhard, G.
Pu interaction studies with a typical bacterial isolate from Mont Terri Opalinus clay
TD-246 Joint BN, GD, HT, MA Mont Terri Meeting, February 10–11, 2014, St. Ursanne, Switzerland.
- Moll, H.; Lütke, L.; Cherkouk, A.; Bernhard, G.
Pu interaction with bacterial isolates from Mont Terri Opalinus Clay
Plutonium Futures – The Science 2014, September 07–12, 2014, Las Vegas, U.S.A.
- Müller, K.; Berger, J.; Gröschel, A.
In-situ vibrational spectroscopic identification of Np(V) sorption complexes at the mineral oxide-water interface
247th ACS National Meeting, March 16–20, 2014, Dallas, Texas, U.S.A.
- Müller, K.; Foerstendorf, H.; Steudtner, R.; Rossberg, A.
Actinyl(V/VI) complexes at water-mineral interfaces investigated by vibrational spectroscopy and complementary techniques
Institutskolloquium, February 28, 2014, Umeå, Sweden.
- Noseck, U.; Britz, S.; Flügge, J.; Mönig, J.; Brendler, V.; Stockmann, M.
New methodology for realistic integration of sorption processes safety assessments
WM2014 Conference, March 02–06, 2014, Phoenix, U.S.A.

- Poetsch, M.; Claus, M.; Lippold, H.
Effect of ionic strength on the mobility of radionuclides in the presence of natural organic matter: testing the Linear Additive Model
Goldschmidt 2014, June 08–13, 2014, Sacramento, U.S.A.
- Prieur, D.; Carvajal-Nunez, U.; Vigier, J. V.; Somers, J.; Bes, R.; Martin, P.; Lebreton, F.; Caisso, M.; Delahaye, T.; Scheinost, A. C.; Hennig, C.; Pruessmann, T.; Vitova, T.; Kvashnina, K. O.
Electronical and structural changes induced by the incorporation of Am into conventional fuels
NUMAT 2014, October 27–30, 2014, Hilton Clearwater, U.S.A.
- Raff, J.; Weinert, U.; Nikolaus, N.; Guenther, T.; Strehlitz, B.; Pollmann, K.
Using nature's genius for pollutant detection
Rapid Methods Europe 2014, March 31–April 02, 2014, Noordwijkerhout, Netherlands.
- Richter, C.
The influence of naturally occurring microorganisms on the sorption of uranium
LLNL intern seminar, June 23–24, 2014, Livermore, U.S.A.
- Richter, C.; Fahmy, K.
Investigation of contaminated soil
ISBC Meeting, Lund 2014, June 03, 2014, Lund, Sweden.
- Rossberg, A.; Domaschke, K.; Lucks, C.; Tsushima, S.
Analysis of EXAFS spectra with the aid of neural networks: aqueous U(VI) complexes with aliphatic (hydroxy-) carboxylic acids
Actinide XAS 2014, May 20–22, 2014, Schloss Boettstein, Switzerland.
- Sachs, S.; Heller, A.; Geipel, G.; Bernhard, G.
Impact of Eu(III) on mammalian cells as a function of its speciation
International Conference on Radioecology and Environmental Radioactivity ICRER, September 07–12, 2014, Barcelona, Spain.
- Scheinost, A.C.; Dumas, T.; Steudtner, R.; Fellhauer, D.; Gaona, X.; Altmaier, M.
Interaction of plutonium and neptunium with magnetite under anoxic conditions: reduction, surface complexation, and structural incorporation
Actinide XAS 2014, May 20–22, 2014, Schloss Boettstein, Switzerland.
- Scheinost, A. C.; Prieur, D.; Smith, A.; Martin, P. M.; Lebreton, F.; Belin, R. C.
X-ray Absorption Spectroscopy of nuclear materials at the Rossendorf Beamline, ESRF NES Colloquium, November 19, 2014, Villigen, Switzerland.
- Schmeide, K.; Jordan, N.; Moll, H.; Cherkouk, A.; Lippold, H.; Poetsch, M.; Kulenkampff, J.; Fritsch, K.
Wechselwirkung von Uran und Plutonium mit Ton, Tonorganika und bakteriellen Tonisolaten
6. Workshop des Verbundprojekts "Rückhaltung endlagerrelevanter Radionuklide im natürlichen Tongestein und in salinaren Systemen", April 08–09, 2014, Mainz, Germany.
- Schmeide, K.; Joseph, C.; Brendler, V.
U(VI) retention by potential host rocks: Comparison of clay and crystalline rock
RadChem 2014 – 17th Radiochemical Conference, May 11–16, 2014, Mariánské Lázně, Czech Republic.
- Schmeide, K.; Joseph, C.; Brendler, V.
Uranium(VI) retention in clay and crystalline rock: how and why does it differ
8th European Summer School on Separation Chemistry and Conditioning as well as Supramolecular, Intermolecular, Interaggregate Interactions, July 07–09, 2014, Bonn/Bad Godesberg, Germany.
- Schmeide, K.; Joseph, C.; Fritsch, K.
Uranium(VI) and neptunium(V) retention by clay minerals and natural clay rock – Influence of clay organics, temperature and pore water salinity
51st Annual Meeting of the Clay Minerals Society, May 17–21, 2014, College Station, Texas, U.S.A.
- Schmidt, M.; Fenter, P.; Lee, S. S.; Bellucci, F.; Wilson, R. E.; Knope, K. E.; Soderholm, L.
Interfacial reactivity of Pu and Th at the muscovite (001) basal plane
Actinide XAS 2014, May 20–22, 2014, Schloss Boettstein, Switzerland.
- Schmidt, M.; Knope, K. E.; Lee, S. S.; Stubbs, J. E.; Eng, P. J.; Bellucci, F.; Fenter, P.; Soderholm, L.
Surface-mediated formation of Pu(IV) nanoparticles on muscovite
Goldschmidt 2014, June 08–13, 2014, Sacramento, U.S.A.

- Schmidt, M.; Lee, S.S.; Knope, K.E.; Bellucci, F.; Soderholm, L.; Fenter, P.
Interfacial reactivity of Pu and Th at the muscovite (001) basal plane
247th ACS National Meeting, March, 16–20, 2014, Dallas, Texas, U.S.A.
- Schymura, S.; Hildebrand, H.; Kuhlenkampff, J.; Franke, K.; Lippmann-Pipke, J.
The application of radiolabelled nanoparticles in transport studies
CYCLEUR Meeting 2014, November 13–14, 2014, Ispra, Italy.
- Schymura, S.; Kulenkampff, J.; Franke, K.; Lippmann-Pipke, J.
Environmental mobility of carbon nanotubes
International Conference on Safe production and use of nanomaterials, Nanosafe 2014, November 18–20, 2014, Grenoble, France.
- Steutner, R.; Großmann, K.
Cryo-Fluoreszenzspektroskopie – Eine innovative Technik für die Wissenschaft
ProcessNet-Jahrestagung, September 30–October 02, 2014, Aachen, Germany
- Stumpf, T.
Grundlagenforschung als wichtiger Beitrag zur Langzeitsicherheit nuklearer Endlager
Geowissenschaftliches Kolloquium, November 10, 2014, Friedrich-Schiller-Universität Jena, Jena, Germany.
- Stumpf, T.
Prozessverständnis auf molekularer Ebene – Ein wesentlicher Beitrag zur Endlagerforschung im Hinblick auf die Sicherheit von Mensch und Umwelt
GDCh-Kolloquium des Ortsverbandes Freiberg; April 30, 2014, Technische Universität Bergakademie Freiberg, Freiberg, Germany.
- Stumpf, T.
TRLFS – Actinides and lanthanides as atomic sensors
Microsymposium on Solvent Extraction, September 12, 2014, Technische Universität Dresden, Dresden, Germany.
- Suhr, M.
Innovative Methoden in der Bionanotechnologie – Die Quarzkristallmikrowaage (QCM-D)
Umweltkolloquium der Fakultät Maschinenbau/Verfahrenstechnik, Studiengang Chemieingenieurwesen, May 20, 2014, Dresden, Germany.
- Vauchy, R.; Robisson, A. C.; Martin, P. M.; Belin, R. C.; Aufore, L.; Scheinost, A. C.; Hodaj, F.
Impact of the cation distribution homogeneity on the americium oxidation state in the (U_{0.54}Pu_{0.45}Am_{0.01})O_{2-x} mixed oxide
Plutonium Futures – The Science 2014, September 07–12, 2014, Las Vegas, U.S.A.
- Weinert, U.; Günther, T.; Lehmann, F.; Vogel, M.; Suhr, M.; Matys, S.; Bobeth, C.; Kutschke, S.; Pollmann, K.; Raff, J.
Multifunctional S-layer proteins as building blocks for hybrid materials
Multifunctional S-layer proteins as building blocks for hybrid materials, September 23–25, 2014, Darmstadt, Germany.
- Weinert, U.; Lederer, F.; Günther, T.; Lehmann, F.; Drobot, B.; Vogel, M.; Pollmann, K.; Raff, J.
Bioinspired hybrid nanomaterials based on self-assembling proteins
Biomaterials – Made in Bioreactors, May 26–28, 2014, Radebeul, Germany.
- Zänker, H.; Hennig, C.; Weiss, S.
Silica-stabilised actinide(IV) colloids in neutral and slightly alkaline solutions
IGDTP-Geodisposal 2014, 24–26, 2014, Manchester, U.K.
- Zänker, H.; Weiss, S.; Hennig, C.; Husar, R.
Actinide(IV) colloids at near-neutral pH due to reaction with dissolved silicic acid
2nd Annual Workshop CP BELBaR (Bentonite erosion effects on the long term performance of the engineered barrier and radionuclide transport), June 16–18, 2014, Meiringen, Switzerland.

In addition, more than 40 posters were presented at international conferences and workshops.

PATENTS

Lütke, L.; Moll, H.

**P1211 – Verfahren und System zur
Abtrennung von Schwermetallen**

DE102013207197.3 – Grant: October 23, 2014.

Raff, J.; Lakatos, M.; Matys, S.; Katzschner, B.;
Pompe, W.

**P1312 – Funktionalisierung von
Edelmetallnanopartikeln mit Monomeren
und Oligomeren bakterieller Hüllproteine für
biosensorische Anwendungen**

DE102013204543 – Grant: February 13, 2014.

THESES

DOCTORAL THESES

Attia, E.

**Interactions of quercetin-uranium complexes
with biomembranes and DNA**

*Technische Universität Dresden, Dresden,
Germany (2014).*

Baldova, D.

**Feasibility study on high-conversion Th-U233
fuel cycle for current generation of PWRs**

*Czech Technical University in Prague, Prague,
Czech Republic (2014).*

Bilodid, Y.

**Spectral history modeling in the reactor
dynamics code DYN3D**

*Technische Universität Dresden, Dresden,
Germany (2014).*

Osman, A. A. A.

**Investigation of uranium binding forms in
relevant environmental waters and bio-fluids**

*Technische Universität Dresden, Dresden,
Germany (2014).*

DIPLOMA THESES

Bittner, L.

**Prozessbeobachtung von Vergütungsmaß-
nahmen im Salzgestein mittels Positronen
Emissions Tomographie (GeoPET)**

*University of Applied Sciences, Zittau/Görlitz,
Germany (2014).*

Leipold, T.

**Sequentielle/simultane in situ Erfassung von
lateralen Radionuklidverteilungen in
Säulenanlagen**

*University of Applied Sciences, Zittau/Görlitz,
Germany (2014).*

Stuhlfauth, C.

**Säulenversuche zur Adsorption von MCPA
an künstlichen Bodenmineralmischungen**

*Johannes-Gutenberg-Universität Mainz, Mainz,
Germany (2014).*

MASTER THESES

Gauss, L.

Spectroscopic studies of an amphipathic structure element of the copper transporter CopA

Technische Universität Dresden, Dresden, Germany (2014).

Köppchen, S.

Kultivierung von Mikroorganismen aus dem ehemaligen Uranbergwerk Königstein im Hinblick auf mikrobielle Sanierungsstrategien

Technische Universität Dresden, Dresden, Germany (2014).

Gabernet-Garriga, G.

DNA origami platform for membrane protein structure determination

Technische Universität Dresden, Dresden, Germany (2014).

Liebmann, M.

Untersuchungen zur Metallbindung der MIIA-Domäne aus dem Protein Vic_001052 von *Vibrio coralliilyticus* ATCC BAA-450

Technische Universität Dresden, Dresden, Germany (2014).

BACHELOR THESES

Strobel, A.

Untersuchungen zur Struktur und des Bindungsverhaltens von Uran(VI) an Glutathiondisulfid mittels NMR- und zeitaufgelöster Laserfluoreszenz-Spektroskopie

University of Applied Sciences, Zwickau, Germany (2014).

SCIENTIFIC ACTIVITIES

- ▣ SEMINARS (TALKS OF VISITORS)
- ▣ WORKSHOPS
- ▣ ATAS 2014
- ▣ TEACHING ACTIVITIES

SEMINARS

Tits, J.

Laboratory for Waste Management, Paul Scherrer Institut (PSI), Villigen, Switzerland
Site-selective luminescence spectroscopy investigations of the U(VI) speciation in highly alkaline, cementitious environments
March 04, 2014

Neumeier, S.

Forschungszentrum Jülich, Germany
Ceramic materials for innovative waste management strategies
March 28, 2014

Roesky, P.

Institut für Anorganische Chemie, Karlsruher Institut für Technologie (KIT), Germany
Chemie der Selten-Erden: Homogene Katalyse und ungewöhnliche Verbindungen
April 10, 2014

Merroun, M. L.

Universidad de Granada, Spain
Biogeochemical processes at the interface mineral-bacteria-radionuclides: multidisciplinary approach characterization
April 14, 2014

Patzschke, M.

Universität Helsinki, Finland
Von induzierten Ringströmen bis zur homogenen Katalyse. Wie Berechnungen zum Verständnis der Chemie beitragen
May 05, 2014

Lloyd, J.

University of Manchester, U.K.
The geomicrobiology of the nuclear fuel cycle
July 09, 2014

Krone, J.

DBE TECHNOLOGY GmbH, Peine, Germany
Erfahrungen der DBE TECHNOLOGY GmbH bei der Planung von Endlagerbergwerken und Realisierung von Verschlussbauwerken für Endlager radioaktiver Abfälle
July 09, 2014

Steppert, M.

Institut für Radioökologie und Strahlenschutz, Leibniz Universität Hannover, Germany
Ionic solution species of molybdenum in strongly acidic media characterized by means of electrospray ionization mass spectrometry
October 01, 2014

Bagus, P. S.

Department of Chemistry, University of North Texas, U.S.A.
The Near-Edge X-Ray Absorption structure of heavy metal oxides
October 01, 2014

Kubicki, J. D.

Pennsylvania State University, U.S.A.
Computational spectroscopy in environmental chemistry
October 10, 2014

Cervinka, R.

ÚJV Rez, Czech Republic
Activities of fuel cycle chemistry department, ÚJV Rez
October 20, 2014

Videnská, K.

ÚJV Rez, Czech Republic
The dynamic column experiments performed by ÚJV Rez
October 20, 2014

Letho, J.

Laboratory of Radiochemistry, Department of Chemistry, University of Helsinki, Finland
Sorption processes of cesium in soil and bedrock
October 27, 2014

Nies, D. H.

Martin-Luther-Universität Halle-Wittenberg
CH34 als Alchemist
November 11, 2014

WORKSHOPS; (CO)-ORGANIZED BY THE IRE

Bilateral meeting – Institute of Radioecology and Radiation Protection (IRS), Leibniz Universität Hannover, Germany, and the Institute of Resource Ecology (IRE)

IRS, Hannover, Germany, June 05–06, 2014.

Brendler, V.

Research within the division of surface processes

Cherkouk, A.

Microorganisms and their impact on radionuclide speciation in potential nuclear waste disposals

Franzen, C.

Retention of Selenium-79 at the water-mineral interface in the context of nuclear waste repositories

Geipel, G.

Uptake of actinides by plants - new data and future plans

Husar, R.

Unusual self-organisation of nanocrystalline neptunium dioxide

Lütke, L.

The impact of the U(VI) speciation on the U(VI) uptake and stress response in plants

Müller, K.

Vibrational spectroscopic investigations of Np(V) sorption onto hematite

Obeid, M. H.

Adaptation of bacterial strains to low doses of uranium inferred from microcalorimetry

Raff, J.

Interaction of actinides and lanthanides with biological interfaces

Riebe, B.

TransAqua: Analysis of ^3H , ^{14}C , ^{36}Cl , ^{90}Sr , ^{129}I and $^{239}\text{Pu}/^{240}\text{Pu}$ in ground water and drinking water

Steppert, M.

Uranium solution speciation investigated by nano-electrospray ionization time-of-flight mass spectrometry

Vahlbruch, J.-W.

Entwicklungen und Trends in der Strahlenschutz Ausbildung

Walther, C.

Trace Analysis of Actinides in environmental samples. AMS, SIMS, RIMS and beyond

Workshop of the

Nuclear Energy and Safety Research Department, Laboratory for Waste Management (LES), Paul Scherrer Institute (PSI), Villigen, Switzerland, and the Institute of Resource Ecology (IRE)

PSI, Villigen, Switzerland, August 25–26, 2014.

Cherkouk, A.

Microorganisms in extreme environments

Dähn, R.

Mikrodiffraction

Drobot, B.

Speciation of uranyl(VI) using combined theoretical and luminescence spectroscopic methods

- Geipel, G.
Uranium in plant cells – Uptake and speciation
- Huittinen, N.
Rare earth phosphate ceramics for conditioning of radioactive waste
- Ikeda-Ohno, A.
Research on *f*-elements chemistry at HZDR – Introduction of new research division “Chemistry of the *f*-elements”
- Pegado, L.
Molecular modelling of C-S-H phases
- Pfingsten, W.
Diffusion mit stark sorbierenden Tracern
- Poonoosamy, J.
Modelling of reactive transport experiments

2ND INTERNATIONAL WORKSHOP ON ADVANCED TECHNIQUES FOR ACTINIDE SPECTROSCOPY (ATAS 2014)

HZDR, Dresden, Germany, November 03–07, 2014.

(Only lectures are noted. Complete abstract book available at: www.hzdr.de/atas)

- Aoyagi, N. (JAEA, Japan)
Synthesis and laser spectroscopy of uranium(IV, VI) complexes in ionic liquids
- Autillo, M. (CEA, France)
Study of paramagnetic actinide complexes with dipicolinate ligands
- Bader, M. (HZDR, Germany)
TRLFS studies on biosorption of uranium on halophilic archaea at high ionic strength (3 M NaCl)
- Bahl, S. (KIT, Germany)
Spectroscopic and microscopic characterization of U bearing multicomponent borosilicate glass
- Baker, R. J. (Trinity College Dublin, Ireland)
Uranyl minerals as models for the long term storage of spent nuclear fuels
- Bernier-Latmani, R. (EPFL, Switzerland)
Mechanism and products of U(VI) reduction in the subsurface
- Berthomieu, C. (CEA, France)
Chelation of uranyl by variants of the calmodulin EF-hand motif
- Boily, J.-F. (Umeå University, Sweden)
Mineral surface hydroxo group identity and reactivity
- Boyanov, M. I. (Bulgarian Academy of Sciences, Bulgaria)
Uptake, reduction, and reoxidation mechanisms of uranium in biogeochemical systems studied by X-ray absorption spectroscopy
- Britz, S. (GRS, Germany)
Using CLSM and TRLFS analysis to describe spatial distributions of Eu surface complexes – Future perspectives
- Burek, K. (University of Potsdam, Germany)
Luminescence of lanthanides in aqueous solutions in the presence of small organic molecules
- Çakir, P. (ITU, European Community)
Surface interaction of actinide oxides and mixed oxides with ice under UV light: an UPS, XPS investigation
- Campbell, A. (PNNL, U.S.A.)
Molecular insights into actinide speciation at interfaces and nanoparticles
- Cha, W. (KAERI, South Korea)
ATR-FTIR and UV-Vis spectroscopic studies of aqueous U(IV)-oxalate complexes
- Conradson, S. D. (Soleil, France)
Bose-Einstein-Hubbard condensate-type behavior via a novel mechanism in the *f* electron Mott insulator $UO_{2+(x)}$

- Creff, G. (University of Nice, France)
Mechanisms of uranium and thorium accumulation in the bone matrix
- Eloirdi, R. (ITU, European Community)
XPS and UPS study on the electronic structure of ThO_x (x ≤ 2) and (U,Th)O_x (x ≤ 2) thin films
- Geipel, G. (HZDR, Germany)
Uranium Redox processes – initiated by plant cells
- Huittinen, N. (HZDR, Germany)
Site-selective TRLFS of Eu(III) doped rare earth phosphates for conditioning of radioactive wastes
- Ikeda-Ohno, A. (HZDR, Germany)
Hydrolysis of tetravalent cerium (Ce(IV)) – A multi-spectroscopic study on nanocrystalline CeO₂ formation
- Kremleva, A. (TU Munich, Germany)
Computational modeling of actinide adsorption on edge surfaces of 2:1 clay minerals
- Kretzschmar, J. (HZDR, Germany)
Nuclear magnetic resonance spectroscopy in Ln/An research
- Kwon, K. D. (Kangwon National University, South Korea)
Mechanistic understanding of mineral reactivity toward trace metals through density functional theory
- Natrajan, L. S. (University of Manchester, U.K.)
Monitoring redox and separation behavior of actinide ions by a combination of NMR and Emission Spectroscopy
- Ohnuki, T. (JAEA, Japan)
Importance of actinides-organic complexes in biodegradation and bioreduction
- Pidchenko, I. (KIT, Germany)
Plutonium oxidation state speciation in aqueous solution studied by Pu L and M edge high energy resolution XANES technique
- Quinto, F. (KIT, Germany)
AMS of actinides in ground- and sea-water: a new procedure for simultaneous trace analysis of U, Np, Pu, Am and Cm isotopes
- Rossberg, A. (HZDR, Germany)
Interaction of U(VI) with aluminium(hydr)oxides: structural analysis combining EXAFS and artificial intelligence
- Saeki, M. (JAEA, Japan)
Elemental analysis of simulated debris of nuclear fuel in water by fiber-coupled Laser Induced Breakdown Spectroscopy
- Saito, T. (JAEA, Japan)
Eu³⁺ binding to deep groundwater humic substances studied by time resolved laser fluorescence spectroscopy and factor analysis
- Schimmelpfennig, B. (KIT, Germany)
Development of accurate force field parameters for An(III)/Ln(III) ions in aqueous solution
- Schreckenbach, G. (University of Manitoba, Canada)
Theoretical actinide molecular science: aqueous species, macrocycles, mineral surfaces
- Shiryaev, A. A. (IPCE-RAS, Russia)
Structure and inclusions in bulk and dispersed samples of Chernobyl “lava”: data from vibrational spectroscopy, XAFS and X-ray tomography
- Su, J. (Chinese Academy of Science, China)
A joint photoelectron spectroscopy and theoretical study on uranium halide complexes
- Wang, Z. (PNNL, U.S.A.)
Cryogenic Laser-Induced Time-Resolved Luminescence Spectroscopy of U(VI) in mineral mixtures and natural sediments
- Yang, P. (PNNL, U.S.A.)
Coordination of actinyl ions to nitrogenous heterocyclic ligands: a joint theoretical and experimental study

ACKNOWLEDGEMENTS

The organizers gratefully acknowledge the financial support provided by Commission of the European Communities (Talisman), Federal Ministry of Education & Research (BMBF), Deutsche Forschungsgemeinschaft (DFG), Gesellschaft Deutscher Chemiker (GDCh), Bruker Optik GmbH, Perkin Elmer GmbH, Horiba Ltd., LOT-Oriel/Andor – An Oxford Instruments Company.

Round-Robin test in actinide spectroscopy at ATAS 2014

Steudtner, R.; Müller, K.; Tsushima, S.;

Foerstendorf, H. (all HZDR)

Cluster speakers:

Kumke, M. U. (Univ. Potsdam, Germany);

Lefèvre, G. (ENCSP, France);

Rothe, J. (KIT, Germany);

Mason, H. (LLNL, U.S.A.);

Walther, C. (Univ. Hannover, Germany);

Yang, P. (PNNL, U.S.A.)

An inter-laboratory round-robin test was initiated by the organizers of the workshop. The aim is a unique comparison of molecular information obtained from the different spectroscopic and theoretical approaches. Hence, concordance as well as the source of discrepancies between the several methods will be evaluated. The findings are expected to illuminate the potentials as well as the limitations of the coupling of selected spectroscopic and theoretical approaches as a tool for the molecular study of actinide complexes. More than 40 scientists from 20 institutions in 7 countries are involved. The test is understood to stimulate scientific discussions, but not as a competitive exercise between the labs of the community.

For the experiments of this test, a simple aqueous actinide system (U(VI)/acetate) was selected, which is independently investigated by different analytical techniques, namely IR, Raman, laser-induced fluorescence spectroscopy, X-ray absorption spectroscopy, nuclear magnetic resonance spectroscopy, mass spectrometry, and quantum chemical calculations. The preliminary results obtained so far were presented by nominated speakers each of them representing a cluster of a distinct experimental or theoretical approach. Comprehensive plenum discussions followed the lectures which were held during three sessions at one day of the ATAS workshop. The evaluation of the results is still in progress and will be reported in the forthcoming Annual Report of the HZDR-IRE.

TEACHING ACTIVITIES

Lectures

Stumpf, T.

Radiochemistry

*Technische Universität Dresden,
Summer term 2014*

Brendler, V.

Radiochemie

*Dresden University of Applied Sciences,
Summer term 2014*

Fahmy, K.

Optical and vibrational spectroscopy

*BIOTEC-Master-Course,
Technische Universität Dresden,
Winter term 2013/2014*

Biophysical methods

*Technische Universität Dresden,
Summer term 2013/2014*

Biological thermodynamics

*Technische Universität Dresden,
Summer term 2014*

Lippold, H.

Radiochemistry and radiopharmacology – Part II: origin, properties and applications of ionising radiation

*Leipzig University,
Summer term 2014*

Radioanalytics

*Lecture within the post-graduate course
“Analytics and spectroscopy”,
Leipzig University,
Summer term 2014*

Raff, J.

Mikrobiologie

*Dresden University of Applied Sciences,
Winter term 2013/2014*

Schmidt, M.

Chemistry of f-elements

*Technische Universität Dresden,
Winter term 2014/2015*

Schmidt, M./Bernhard, G.

Environmental chemistry

*Technische Universität Dresden,
Summer term 2014*

Courses

☞ The laboratory course “Radiochemistry“ was provided from August 18th to 22nd and from 25th to 29th, 2014, as a part of a module of the chemistry master degree program at the Technische Universität Dresden.

Advisers:

Bader, M.	Gerber, U.	Mey, S.
Barthen, R.	Heim, H.	Dr. Müller, K.
Drobot, B.	Hellebrandt, S.	Peschel, S.
Fischermeier, E.	Husar, R.	Richter, C.
Fritsch, K.	Kretzschmar, J.	Wilke, C.

☞ The IRE provided two experiments “Alpha spectrometric isotope dilution analysis of uranium” and “Technetium in Nuclear Medicine” (since 2014/15) of the laboratory course “Instrumental Analysis” held by the Institute for Analytical Chemistry, Technische Universität Dresden, during winter term.

Advisers:

Winter term

2013/2014 2014/2015

Gagell, C.	Barthen, R.	Peschel, S.
Nebe, K.	Drobot, B.	Richter, C.
Weiß, S.	Dr. Franzen, C.	Taube, F. (TUD)
Zirnstein, I.	Hellebrandt, S.	Weiß, S.
	Hofmann, S. (KIT)	Wilke, C.

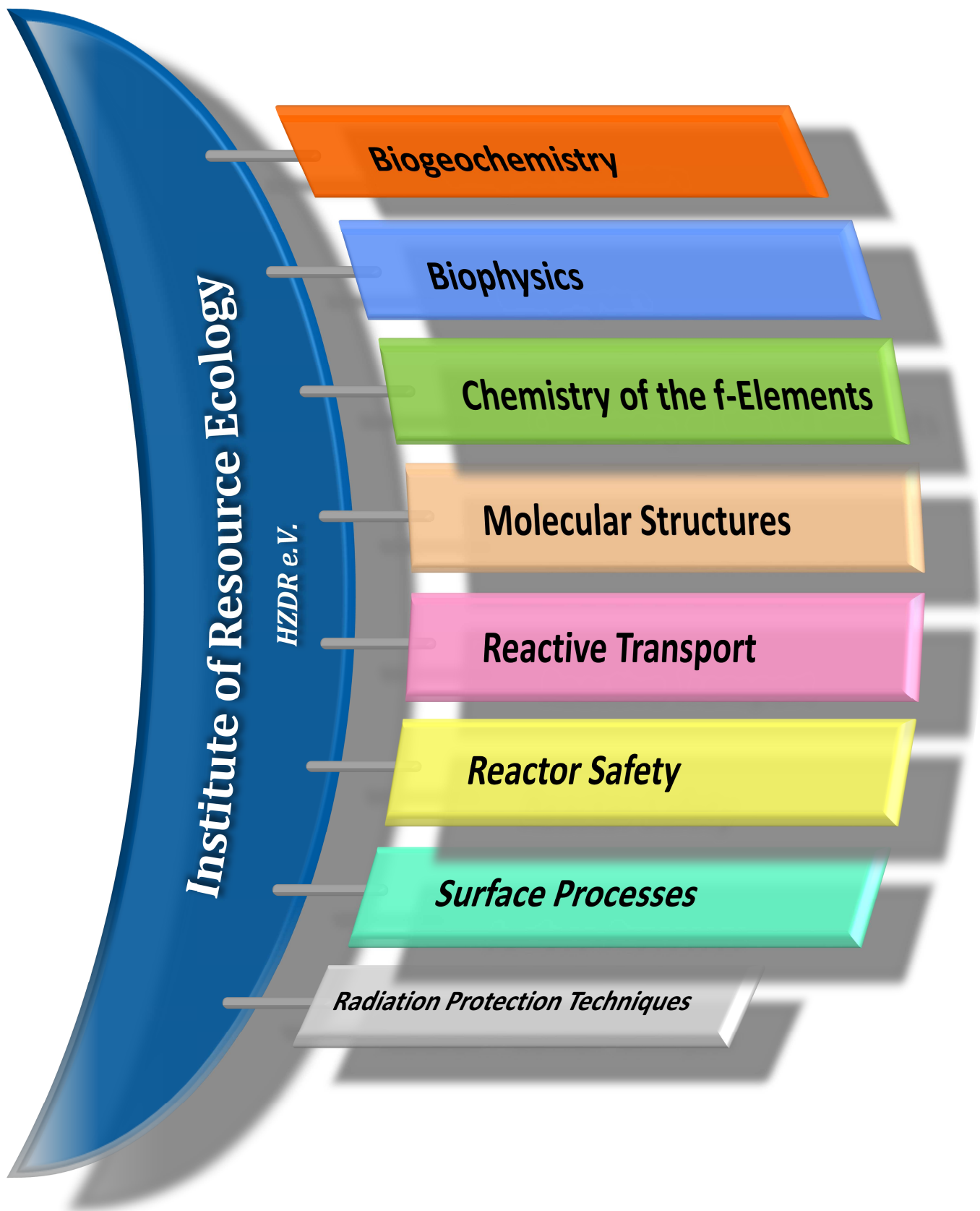
☞ Biophysics course of the Dresden-International-Graduate School.

Advisers:

Winter term 2014/2015

Prof. Dr. Fahmy, K.	Philipp, J.
Dr. Oertel, J.	Sayed, A.

PERSONNEL



Prof. Dr. Thorsten Stumpf
(HEAD OF INSTITUTE)

ADMINISTRATION:

Office Dresden: Gorzitze, Jana; Kurde, Kerstin;
Lauke, Regina

Office ESRF: Glückert, Marion

Office Leipzig: Gerstner, Katrin

Sysad: Berndt, Ronny

PROJECT COORDINATION:

Office Dresden: Dr. Arnold, Thuro

RADIATION PROTECTION:

Heim, Heidemarie

Falkenberg, Dirk

Henke, Steffen

Hiller, Bernd

Nebe, Kathrin

Rumpel, Annette



BIOGEOCHEMISTRY

Dr. Geipel, Gerhard

Dr. Baumann, Nils

Drobot, Björn

Dudek, Monika

Flemming, Katrin

Gagell, Corinna

Gerber, Ulrike

Dr. Großmann, Kay

Dr. Günther, Alix

Dr. Heller, Anne

Heller, Sylvia

Dr. Krawczyk-Bärsch, Evelyn

Dr. Moll, Henry

Müller, Manuela

Dr. Raff, Johannes

Ramisch, Alexander

Dr. Sachs, Susanne

Schulz, Katja

Seibt, Jana

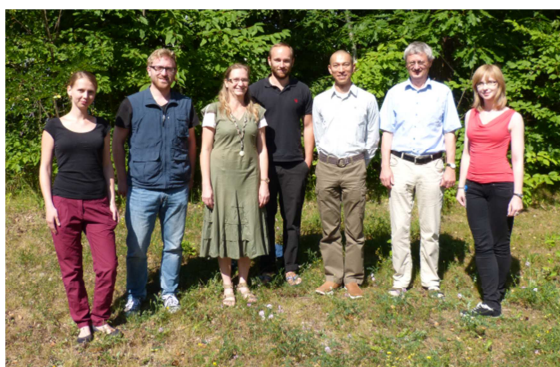
Dr. Vogel, Manja

Zirnstein, Isabel

HZDR Young Investigator Group

Dr. Cherkouk, Andrea

Bader, Miriam



CHEMISTRY OF THE F-ELEMENTS

Dr. Ikeda-Ohno, Atsushi

Dr. Barkleit, Astrid

Husar, Richard

Dr. März, Juliane

Dr. Schmid, Matthias

Wilke, Claudia

Dr. Zänker, Harald



BIOPHYSICS

Prof. Dr. Fahmy, Karim

Abu Sharkh, Sawsan E.

Attia, Enas M. H.

Fischermeier, Elisabeth

Obeid, Muhammad H.

Dr. Oertel, Jana

Philipp, Jenny

Sayed, Ahmed M. T.

Suhr, Matthias

Dr. Tsushima, Satoru

MOLECULAR STRUCTURES

Dr. habil. Scheinost, Andreas C.

Dr. Butzbach, Randolph
Dulnee, Siriwan
Exner, Jörg
Fengler, Matthias
Dr. Hennig, Christoph
Dr. Lozano Rodriguez, Janeth
Dr. Rossberg, André
Dr. Steudtner, Robin



REACTIVE TRANSPORT

Dr. Lippmann-Pipke, Johanna

Barthen, Robert
Dr. Franke, Karsten
Gründig, Marion
Gruhne, Stefan
Dr. Hildebrand, Heike
Korn, Nico
Dr. Kulenkampff, Johannes
Dr. Lippold, Holger
Lösel, Dagmar
Dr. Mansel, Alexander
Poetsch, Maria
Schößler, Claudia
Dr. Schymura, Stefan
Zakhnini, Abdelhamid



SURFACE PROCESSES

Dr. Brendler, Vinzenz

Dr. Bok, Frank
Eckardt, Carola
Fischer, Sarah
Dr. Foerstendorf, Harald
Dr. Franzen, Carola
Fritsch, Katharina
Dr. Großmann, Kay
Gürtler, Sylvia
Gurlit, Sabrina
Heim, Karsten
Dr. Huittinen, Nina
Dr. Jordan, Norbert
Kappler, Ina
Kretzschmar, Jerome
Lense, Nadine
Lehmann, Susanne
Müller, Christa
Dr. Müller, Katharina
Neubert, Heidrun
Dr. Richter, Anke
Richter, Constanze
Ritter, Aline
Dr. Schmeide, Katja
Schott, Juliane
Dr. Stockmann, Madlen
Weiß, Stephan

HGF Young Investigator Group

Dr. Schmidt, Moritz

Hellebrandt, Stefan
Dr. Johnstone, Erik
Peschel, Sophia

REACTOR SAFETY

Dr. Kliem, Sören

Dr. Baier, Silvio
Baldova, Daniela
Bilodid, Yurii
Dr. Dürigen, Susan
Dr. Fridman, Emil
Glivici-Cotruta, Varvara
Gommlich, André
Dr. Grahn, Alexander
Hoffmann, Alexander
Holt, Lars
Konheiser, Jörg
Kozmenkov, Yaroslav
Litskevich, Dzianis
Dr. Merk, Bruno
Nikitin, Evgeny
Rachamin, Reuven
Dr. Rohde, Ulrich
Dr. Schäfer, Frank
Dr. Tusheva, Polina

GUEST SCIENTISTS

Bernhard, Gert	<i>Radiochemie, Technische Universität Dresden Dresden, Germany</i>
Elo, Outi	<i>Laboratory of Radiochemistry, University of Helsinki, Helsinki, Finland</i>
Fricke, Thomas	<i>Vita 34 AG, Leipzig, Germany</i>
Ieremenko, Maksym	<i>Scientific-technical Centre for Nuclear and Radiation Safety of the Ukraine, Kiew, Ukraine</i>
Jain, Rohan	<i>UNESCO-IHE, Institute for Water Education, Delft, The Netherlands</i>
Kovacs, Istvan Soma	<i>The Institute of Nuclear Techniques, Budapest University of Technology and Economics, Budapest, Hungary</i>
Margulis, Marat	<i>The Unit of Nuclear Engineering, Reactor Physics Research Group, Ben-Gurion University of the Negev, Be'er Sheva, Israel</i>
Ovdiienko, Iurii	<i>Scientific-technical Centre for Nuclear and Radiation Safety of the Ukraine, Kiew, Ukraine</i>
Radeva, Galina	<i>Institute of Molecular Biology, Bulgarian Academy of Sciences, Sofia, Bulgaria</i>
Sabău, Andrea	<i>Laboratoire Ecosystèmes Côtiers Marins Et Réponses aux stress (ECOMERS/EA 4228), Parc Valrose, Nice, France</i>
Shcherbina, Natalia	<i>Institut für Radioökologie und Strahlenschutz, Leibniz Universität Hannover, Hannover, Germany</i>

MASTER/DIPLOMA/BACHELOR

Bittner, Lars	Hildebrand, Pia	Leipold, Thomas
Gauss, Lennard	Ihrig, Martin	Luthardt, Paula
Gerasch, Robert	Köppchen, Sandra	Stuhlfauth, Christin

GRADUATE ASSISTANTS, STUDENT ASSISTANTS, TRAINEES

Adomat, Yasmin	Garriga, Gisela	Krattennacher, Jochen	Maffert, Anika
Bauditz, Maria	Haubitz, Toni	Kuczera, Mirco	Petzold, Saskia
Bauer, Anne	Hinze, Claudia	Plytyn, Maximilian	Simon, Bénédicte
Döge, Sarah	Katin, Alexey	Ruhland, Sandra	Strobel, Alexander
Fischer, Sarah	Kermes, Sissi	Liu, Mingjun	Wollenberg, Anne

ACKNOWLEDGEMENTS

The Institute of Resource Ecology is one of the eight institutes of the Helmholtz-Zentrum Dresden – Rossendorf e.V. (HZDR). As registered, non-profit institution, the HZDR is supported by the authorities of the Federal Government and the Free State of Saxony. In addition to the basic funding, the financial support of the projects listed below by the given organizations and companies is gratefully acknowledged.

FUNDING ORGANIZATION / COMPANY	PROJECT TITLE	CONTRACT NO. (if applicable)
Commission of the European Communities (EU)	ESNII plus Preparing ESNII for HORIZON 2020	60 5172
	FREYA Fast Reactor Experiments for hYbrid Applications	FP7-2696665
	TALISMAN Transnational Access to Large Infrastructures for a Safe Management of ActiNide	FP7-323300
Bundesministerium für Wirtschaft und Technologie (BMWi) & Bundesministerium für Bildung und Forschung (BMBF)	Conditioning Grundlegende Untersuchungen zur Immobilisierung langlebiger Radionuklide mittels Einbau in endlagerrelevante Keramiken	02NUK021B 02NUK021C
	DIL Water Untersuchungen zur Entwicklung neuer Biokompositmaterialien zur Entfernung von Schadstoffen aus Abwässern	02WA1223
	ECOMETALS – Innovative umweltschonende Prozesse für die Gewinnung strategischer und seltener Metalle aus primären und sekundären Ressourcen; TP HZDR: Rohstoffcharakterisierung, mikrobiologische Mobilisierung von Metallen	033RF001A
	EDUKEM – Entwicklung und Durchführung experimenteller Methoden zur verbesserten Modellierbarkeit uranhaltiger salinärer Lösungen	02E11334B
	IMMORAD – Grundlegende Untersuchungen zur Immobilisierung langlebiger Radionuklide durch die Wechselwirkung mit endlagerrelevanten Sekundärphasen	02NUK019D
	Verbundprojekt: Rückhaltung endlagerrelevanter Radionuklide im natürlichen Tongestein und in salinaren Systemen – Geochemisches Verhalten und Transport von Radionukliden (Np, U, Pu und weitere RN) in salinaren Systemen in Gegenwart endlagerrelevanter Organika	02E10971
	TransAqua Teil A: Untersuchungen zu den Wechselwirkungen zwischen unter Tage lebenden Mikroorganismen mit Uran Teil B: Spektroskopische Bestimmung der Bindungsform (Speziation) trivalenter Actinide/Lanthanide in Biofluiden des menschlichen Gastrointestinaltraktes und im Blut	02NUK030F
	VESPA – Aufstockung Verbundprojekt: Verhalten langlebiger Spalt- und Aktivierungsprodukte im Nahfeld eines Endlagers und Möglichkeiten ihrer Rückhaltung	02E10790X
	Verbundprojekt WASA-BOSS: Weiterentwicklung und Anwendung von Severe Accident Codes - Bewertung und Optimierung von Störfallmaßnahmen	02NUK028B
	WEIMAR – Weiterentwicklung des Smart-Kd-Konzepts für Langzeitsicherheitsanalysen	02 E 11072B
WTZ Russland - Transientenanalysen für schnelle Reaktoren	1501462	

FUNDING ORGANIZATION / COMPANY	PROJECT TITLE	CONTRACT NO. (if applicable)
Deutsche Forschungsgemeinschaft (DFG)	ATAS Workshop 2014	MU 3207/2-1
	Surface processes of Np species on selected mineral oxides. From sorption to precipitation	MU 3207/1-1
	Transport von CNP	FR 1643/3-1
AREVA	Experimente PKL3	
Bundesamt für Strahlenschutz (BfS)	Cryo-Fluoreszenzspektroskopie	3342
E.ON, Hannover	MCNP Rechnungen für einen DWR	
	Datenpflege ATHLET-Datensatz für 2013 2014	
	Datensatzerstellung für DWR Anlagen	
	Entwicklung eines Modells thermo mechanisches Brennstabverhalten	
	Potenzialstudie Nuklidabsorbierende Pilze	6021141113
GMBU	Biomasse	6121142112
NRG Petten	ROCOM-PTS	
ONDRAF/NIRAS	Moldata	
VGB Powertech	Kopplung Neutronik/ Thermohydraulik für DWR	SA "AT" 41/09 A
	Kopplung Neutronik/ Thermohydraulik für SWR (TU Dresden)	SA "AT" 41/09 C
TÜV SÜD	Reaktorberechnungen für WWER-1000-Reaktoren	500601247
	KA Reaktorberechnungen für WWER-1000-Reaktoren	
TÜV NORD	Bewertung Computercode	
STFI	Textilien S-Layer	6121112102
UJV Rez, a.s.	DYN3D für UJV Wartung 2013/2014	150178
Wismut	Spezialanalytik WISMUT II	3164929-U02/1
SAB Förderbank, Dresden, Germany	SYNKOPE Synergetische Kopplung von Energieträgern für effiziente Prozesse	100109023
GRS	Codetraining Belarus	
HGF	HGF-Nachwuchsgruppe Dr. Schmidt	VH-NG-942
SCK•CEN, Studiecentrum voor Kernenergie, Brussels, Belgium	Mont Terri BN-experiment ph 17	
	Mont Terri BN Experiment 2014	6121142207

INDEX OF AUTHORS

AUTHOR	PAGE	AUTHOR	PAGE
Abu Sharkh, S.	13	Konheiser, J.	60
Acker, M.	38, 39, 40	Krawczyk-Bärsch, E.	11
Arinicheva, Y.	47, 48	Kretzschmar, J.	38, 42, 43
Arnold, T.	11	Kulenkampff, J.	53
Bader, M.	12	Labs, S.	49
Baier, S.	64	Lee, S. S.	30
Barkleit, A.	15, 16, 38	Lehto, J.	23
Bernhard, G.	14	Lippmann-Pipke, J.	53
Bittner, L.	53	Lippold, H.	32, 55
Bok, F.	29	Litskevich, D.	62
Bosbach, D.	49	Lozano-Rodriguez, M. J.	48
Brachem, C.	60	Lütke, L.	14
Brendler, E.	42, 43	März, J.	41
Brendler, V.	28, 35, 37, 38, 42, 43	Merk, B.	62, 66
Cherkouk, A.	12, 14	Mikityuk, K.	59
Curtius, H.	49	Modolo, G.	66
Dalmiglio, M.	54	Moll, H.	14, 41
Drobot, B.	35, 39	Müller, K.	23, 24, 26
Elo, O.	23	Neumeier, S.	47, 48
Eng, P. J.	30	Nikitin, E.	59
Enzmann, F.	53	Obeid, M.	13
Erkut, C.	13	Oertel, J.	13
Fahmy, K.	13, 36	Pannier, A.	19
Fenter, P.	30	Poetsch, M.	32
Foerstendorf, H.	42, 43	Pollmann, K.	18, 19
Franke, K.	54, 56	Rachamin, R.	63
Franzen, C.	31, 42, 43	Raff, J.	18, 19, 35
Fridman, E.	59, 63	Richter, C.	28
Fritsch, K.	27	Roesky, P. W.	44
Galperin, A.	63	Rohde, U.	61
Geipel, G.	17, 35, 41	Rossberg, A.	24, 26
Geist, A.	66	Sachs, S.	17
Gerber, U.	11	Scheinost, A. C.	23, 25, 48
Gibson, N.	54	Schmeide, K.	27
Gloe, K.	41	Schmid, M.	44
Großmann, K.	28	Schmidt, M.	30
Gründig, M.	53	Schott, J.	38
Gückel, K.	29	Schreier, M.	64
Guillaume, S. M.	44	Schymura, S.	54
Hauser, J.	56	Seidl, M.	60
Heim, K.	42, 43	Simon, B.	24
Hellebrandt, S.	30	Soderholm, L.	30
Heller, A.	15	Stedtner, R.	25, 35
Hennig, C.	37, 49	Stubbs, J. E.	30
Hildebrand, H.	54	Stumpf, T.	47
Holt, L.	61	Suhr, M.	18
Holthausen, J.	47	Taube, F.	39, 40
Hölttä, P.	23	Taut, S.	38, 39, 40
Holzwarth, U.	54	Tsushima, S.	35, 36, 42, 43
Huittinen, N.	23, 47	Vogel, M.	19
Ikeda-Ohno, A.	23, 37	Weiss, S.	37, 49
Jordan, N.	31, 42, 43	Wilke, C.	16
Kliem, S.	61, 64	Wilson, R. E.	30
Knebel, J.	66	Zänker, H.	37, 49
Knope, K. E.	30		

HZDR

 **HELMHOLTZ**
| ZENTRUM DRESDEN
| ROSSENDORF

Institute of Resource Ecology
P.O. Box 51 01 19 · 01314 Dresden/Germany
Phone +49 351 260-3210
Fax +49 351 260-3553
Email contact.resourceecology@hzdr.de
<http://www.hzdr.de>

Member of the Helmholtz Association